Politecnico di Torino

MSc in Mechanical Engineering
A.a. 2022/2023
Degree session October 2023

Friction Modelling of Pneumatic Cylinders for Servo-Positioning Systems

Relatori:
Prof. Luigi Lentini
Prof. Luigi Mazza

Candidato:
Domenico Recchia

ABSTRACT

This thesis presents a comprehensive study focused on examining the three distinct regimes of friction, namely pre-sliding, transition, and gross-sliding, in the context of pneumatic actuation systems. Pneumatic actuators are widely used in the industrial field thanks to their cost-effectiveness, versatility, and mechanical simplicity compared to other types of actuators. Furthermore, the use of air enables greater flexibility in their application, even in flammable or explosive environments and, air as a driving fluid, is considered a sustainable resource compared to other fluids as oils.

The primary objective of this research is to gain a deep understanding of the frictional behaviours that occur when pneumatic actuators are employed, which is crucial for enhancing the efficiency, control, and reliability of such systems. The investigation begins with a complete review of the fundamental principles of friction and its role in pneumatic actuation and then experimental work is conducted to characterize and differentiate the three distinct frictional regimes. Different test setups are utilized to control parameters like pressure and velocity allowing for the study of each regime's behaviour. A system made by a carriage constrained by a linear guide with recirculating ball bearings, which is actuated by a double-acting pneumatic cylinder and a 5/3 proportional flow valve is used. This system is used for the study of transition and gross-sliding regimes. For the pre-sliding regime, experimental trials coming from the literature are taken in account due to the impossibility of conducting certain type of tests. Experimental data are then collected to examine the frictional behaviour. In addition to the experimental approach, numerical models from existing literature are considered in this study as Polito, Dahl, LuGre and Leuven models. Those models are widely used in the literature thanks to their efficiency offering different approaches (static and dynamic) and different accuracy. The results obtained from these numerical simulations are then compared with the experimental results to validate the different models.

The findings of this research contribute to a comprehensive understanding of the pre-sliding, transition, and gross-sliding regimes of friction in pneumatic actuation systems. By clarifying the factors influencing these regimes and their impact on system performance, this study provides valuable insights for the design and control of pneumatic actuators in various applications, including robotics, automation, and manufacturing. Additionally, the knowledge gained from this research can aid in the development of optimized control strategies, materials selection, and lubrication techniques, ultimately leading to more efficient and reliable pneumatic actuation systems. These insights have the potential to make a significant impact on industries where pneumatic actuators play a critical role in achieving precise and controlled motion.

Index

CHAPTER 1 1
1.1 Introduction 1
1.2 Identification of the friction model parameters 15
CHAPTER 2 26
2.1 The friction phenomenon 26
2.2 Numerical models 30
2.2.1 Polito 30
2.2.2 Dahl 31
2.2.3 LuGre 32
2.2.4 Leuven 32
2.3 Time advanced schemes 32
2.4 The numerical implementation 37
2.5 Test bench description 45
CHAPTER 3 59
3.1 Pre-sliding regime test 59
3.2 Transition regime test 61
3.2.1 Overall Results 62
3.2.2 Test 1 63
3.2.3 Other Tests 66
3.3 Gross-sliding regime 72
3.3.1 First configuration 72
3.3.1.1 Overall Results 73
3.3.1.3 Test 2 77
3.3.1.4 Test 3 79
3.3.2 Second configuration 82
3.3.2.1 Overall results 83
CHAPTER 4 88
4.1 Pre-sliding regime 88
4.2 Transition regime 91
4.3 Gross sliding regime 95
4.3.1 First configuration 95
4.3.2 Second sconfiguration 98
CONCLUSIONS 102
BIBLIOGRAPHY 104

CHAPTER 1

In this section will be entailed a brief description of the pneumatic cylinder's applications and the problem about the friction will be highlighted. Then, the most used numerical friction models are listed and concisely described. A discussion it is also necessary about how the parameters that compose the models are found since their empirical and not physical nature.

1.1 Introduction

Pneumatic cylinders are widely used in many industrial applications. They play a key role in automatic process where repeated movements are necessary. From 2011 to 2015, the sales value on the global market of pneumatic cylinders has increased from 837,35· to 961,83·million dollars [1]. Their success can be attributed to the operating flexibility, the high reliability, the relative low cost, and their ability to work in rough environments, i.e., dusty air, explosive environments.
They can be used in a variety of applications regarding manufacturing, robotics, material handling and packaging, where they allow parts or tools to be positioned, moved, or picked up. Other operations include locking, where a piece is held in place by jaws driven by the cylinder, and punching, where the thrust of the pneumatic cylinder allows to mark an object.
However, deal with a compressible fluid has some not negligible consequences: the compression and expansion process of air involves thermodynamic losses due to entropy affecting the efficiency compared to the hydraulic actuators. If we consider the efficiency as the ratio between power consumption to obtain pressurized air and the output power of the cylinder it can be noticed that the pneumatic actuators are the less efficient in comparison to the hydraulic and electric ones. In particular, the pneumatic cylinders can reach up to 20% in efficiency against the 40% of the hydraulic pistons and the 80% of the electric [1]. On the other hand, air can be considered as an eco-friendly medium instead of oil-based medium that are used in the hydraulic cylinders: air is always available, and it can be considered as non-polluting since doesn't need any sort of processing thus avoiding the use of fluids from the oil industry.
The compressibility of the fluid entails relative low accuracy and slight resistance to external noises. Air leakages are also to be reckoned with. Nevertheless, for certain type of functioning they are preferred (i.e., systems that do not require high pressures). Friction losses are also source of lack in performance mainly due to the internal structure of the cylinder (the contact of piston and rod seals with the cylinder walls). Its chaotic and random behaviour is very hard to predict, and it is an obstacle in the optimal use of pneumatic pistons in positioning systems. The value of the friction is never the same and changes according to dozens of parameters.
Friction may occur in nonlinear manner and cause limit cycles and unexpected stick-slip oscillation at low operating velocities. These nonlinear characteristics of the friction make accurate simulation and position control of the fluid power cylinders difficult to achieve.

Predicting friction may also help evaluate the wear (to avoid unexpected failures) of the components other than increase the accuracy. Currently, a knowledge of this phenomena is also warranted since environmental regulations limit the use of lubricant mists in compressed air, and a trend towards more compact cylinders calls for new space-saving sealing arrangements [2]. To overcome these difficulties, it is, therefore, necessary to develop an accurate friction model for the pneumatic cylinders.

The contacts between the asperity of the surfaces of two objects generate friction. The friction force is naturally opposed to the direction of the displacement trying to stop the motion. Friction occurs also in static when the objects in contact are not relatively moving. This force is not easy to predict due to its non-linearity and compromise the accuracy of pneumatic cylinders in servo positioning system: without feedback sensors it is impossible to know the exact position of our system. There is still plenty of ongoing studies that try to replicate and model this phenomenon since there is not a model that can precisely estimate friction.

Friction force is usually subdivided into two regimes: the presliding regime and the gross-sliding regime. In the presliding regime the friction force is mainly a function of position, whereas in the gross-sliding regime the friction force appears as a function of velocity. Within these regimes the observed phenomena can be subdivided into static and dynamic phenomena. This is because frictional behaviours have their own internal dynamics, it thus does not instantaneously react on a change of velocity or displacement. The transition from pre- to gross-sliding occurs when the external applied force overcome a characteristic value, called breakaway force.

In presliding regime, the adhesive forces are dominant. Applying a load (without triggering the motion) means force the asperity to deform both elastically and plastically, behaving as a non-linear spring. As the force increases asperity deforms more and more until it achieves the maximum stiction force (breakaway point) in which the contacts between the asperities breaks as the limit in the stress-strain curve reaches and sliding occurs. In the static field it be noticed a hysteretic behavior due to the non-local memory of the junctions for which the deformation of the roughness depends only on the position of the object and not on the velocity given that it is still not moving. The hysteretic trend moves between two poles: the positive breakaway force and the negative one. What there is in the middle among those two extremes is a function of the micro-displacement of the object and contains internal loops each who moves between their poles given by the past deformations of the asperity. When the force is decreased to zero, not all displacement will be recovered, i.e., there will in general be a residual displacement. Hysteresis depends on the past events that occur in stiction but once the sliding regime starts, the phenomena completely disappears and in the case the object will stop, the hysteresis will start again without memory of the previous deformations.

Above the breakaway point, i.e., in the gross sliding regime, all the junctions are broken, and the friction is no further an only displacement function. Generally, at low velocities there is still a not negligible contribution due to the asperity deformation but when the speed increases more and more, since the asperities have less and less time to interact, the velocity takes the lead and friction is increasingly a velocity function. After the breakaway threshold, the object will suddenly accelerate, and the system will be critically stable. The resistance to the motion during gross sliding usually has its maximum value at the beginning of motion and decreases with increasing relative velocity [3].

The following paragraphs will describe some of the numerical models that are currently used to simulate the frictional behavior of sliding objects.

There are plenty of method that try to estimate the sliding regime in dry friction. Leonardo da Vinci in the 16th century stated the two basic laws of sliding friction: the frictional resistance is proportional to the load and it is independent of the apparent area of the sliding surfaces [4].

Later, in 1781, Coulomb formulated the dry friction laws in the form that is still used today for some simple cases. The Coulomb law is considered a static law in which velocity is not taken in account. Coulomb already divided the friction phenomena in two parts: static and sliding. Coulomb states that starting from rest position, it takes a minimum force $F_s = \mu_s F$ to move an object in contact with another surface. The coefficient μ_s stands for the static friction coefficient. In sliding condition, the coefficient that determines the Coulomb force changes in μ_d, the dynamic friction coefficient. The two coefficients depend on the materials property of the couple of objects in contact.

$$\begin{cases} F_{Coulomb} = \mu_d \, F \\ F_f = F_{Coulomb} \, sign(v) \end{cases}$$

Friction is presented as discontinuous, and its sign depends on the sign of the relative velocity v. In sliding condition, the force keeps constant. This model is considered as a static one in which there is an assumption that in the standstill friction conditions the relative motion between the rubbing bodies does not occur. Static models, with a simpler structure and fewer parameters than in the dynamic models, are mainly dedicated to the study of friction pairs with significant slip velocities and a small number of transitions between standstill and kinetic friction states, especially when these transitions run in a rapid manner [5].

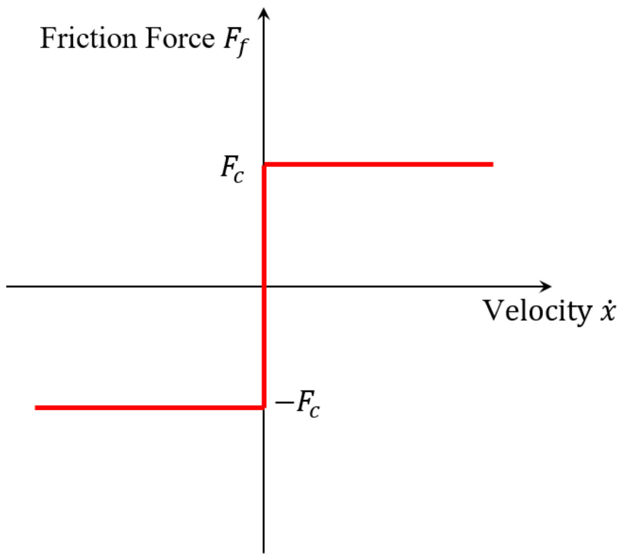

Figure 1.1 The Coulomb model.

The Coulomb stiction model is a variation of the classic Coulomb friction model that aims to capture the phenomenon of stiction. Stiction is observed when the applied force is not sufficient to overcome the static friction and initiate motion. When the relative velocity between the surfaces is greater than zero, the dynamic friction force comes into play and opposes the motion. However, when the relative velocity is zero (indicating stiction), the static friction force becomes the dominant force, preventing any motion from occurring.

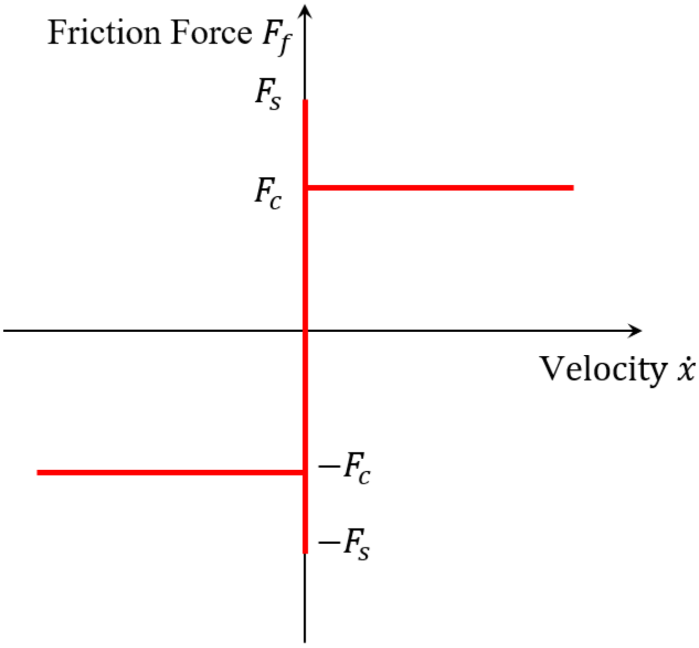

Figure 1.2 The Coulomb-stiction model.

Later, Karnopp tried to overcome the problem of the friction at zero velocity. The Karnopp model (1985) operates by taking the applied force on the object as an input and produces the resulting velocity of the object as an output. Within this model, there exists a defined interval of zero velocity ($|v| < DV$). During this interval, the internal state (which includes the velocity) can change and be non-zero, but the modeled velocity output remains zero. Depending on whether the state lies within or outside the zero-velocity interval, the friction force is determined using either a saturated version of the external force or a static function of the velocity.

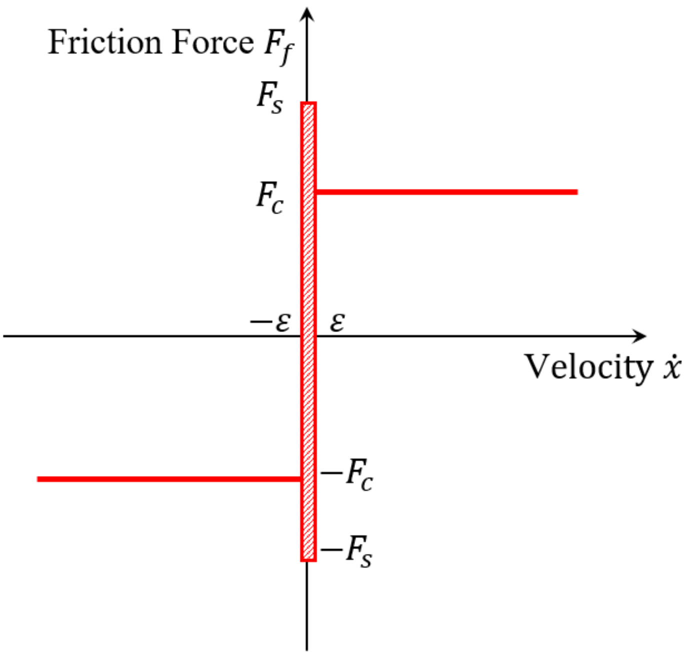

Figure 1.3 The Karnopp model.

Despite its advantages, the Karnopp model has a main drawback in that it requires the external force to be provided as an input, which is not always known. Additionally, the zero-velocity interval does not align with real friction characteristics. Nevertheless, the Karnopp model and its variations are still utilized because they allow for efficient simulations.

The continuous model, also referred to as the smooth Coulomb friction model, is a modified version of the traditional Coulomb model. It was developed to overcome the computational challenges caused by force discontinuity. Instead of a sudden change, a smooth curve is used to address the discontinuity around $v = 0$. An example of this is the investigation of the hyperbolic tangent smoothening function. The Coulomb law changes its formula in [6]:

$$F_f = -F_d \tanh\left(\frac{v}{v_d}\right)$$

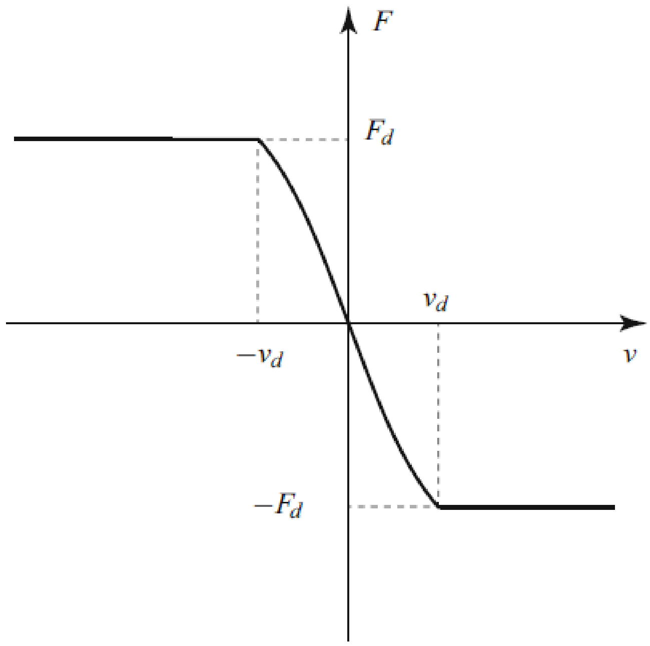

Figure 1.4 The Smooth-Coulomb model [6].

With v_d as the velocity tolerance and F_d is the dynamic friction force. However, this model cannot reproduce stiction because the force is equal to zero when velocity is null.

In the velocity-based friction model instead, an extra curve is incorporated specifically for the range that includes zero velocity. Within this model, F_d represents the dynamic friction force, F_s represents the static friction force, v_d represents the dynamic velocity tolerance, and v_s represents the static velocity tolerance. The curve is constructed by combining trigonometric functions, with F_d, F_s, v_d, and v_s serving as parameters. The formula used in this model is [6]:

$$F_f = -F_s \sin\left[C \tan^{-1}(B\,v) - E\left\{(B\,v) - \tan^{-1}(B\,v)\right\}\right]$$

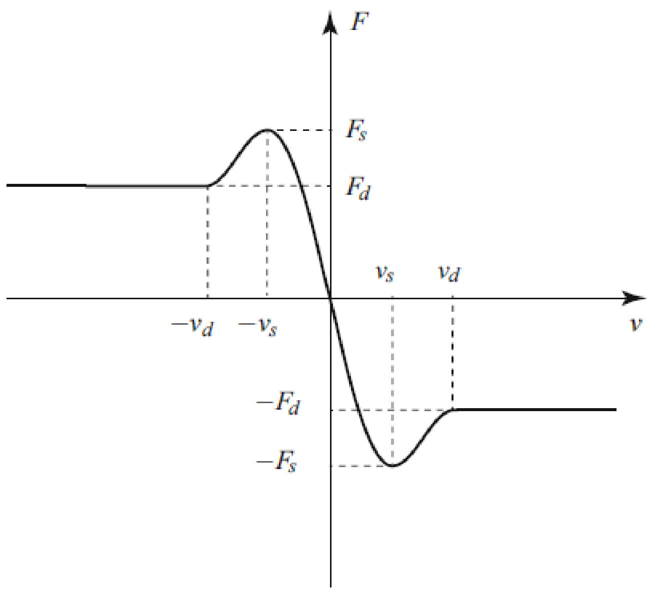

Figure 1.5 Velocity-based friction model [6].

It is important to note that this model falls short of accurately replicating stiction at zero velocity. Nonetheless, the presence of the friction force F_s helps to significantly reduce the relative velocity compared to the smooth Coulomb friction model.

A more complex model was implemented by Stribeck (1902) in which the dependence on velocity in sliding regime is highlighted for the first time. Stribeck modified the constant portion of the Coulomb model replacing it by the Stribeck function $s(v)$. The latter decreases in velocity and bounded by un upper limit at zero velocity equal to the static friction force F_s, and a lower limit equal to the Coulomb force F_c, and a viscous friction part [7]. Stribeck thought about replace the discontinuity of the Coulomb model with a line of finite slop, up to a very small threshold ε and doing experiments for constant velocities he observed that part of the friction force as a function of velocity (for constant velocity) has a negative friction force gradient with increasing speed.

$$F_f = \begin{cases} F_c + (F_s - F_c)e^{\left(\left|\frac{v}{V_s}\right|\right)^{\delta}}, & |v| > \varepsilon \\ \left(F_c + (F_s - F_c)e^{\left(\left|\frac{v}{V_s}\right|\right)^{\delta}}\right)\left(\frac{v}{\varepsilon}\right), & |v| \geq \varepsilon \end{cases}$$

With F_c represents the Coulomb friction force at zero velocity, F_s is the static friction force, V_s is the Stribeck velocity, that is the velocity in correspondence of the lowest value of friction force, and δ is the shaping factor of the Stribeck function, while ε is the threshold.

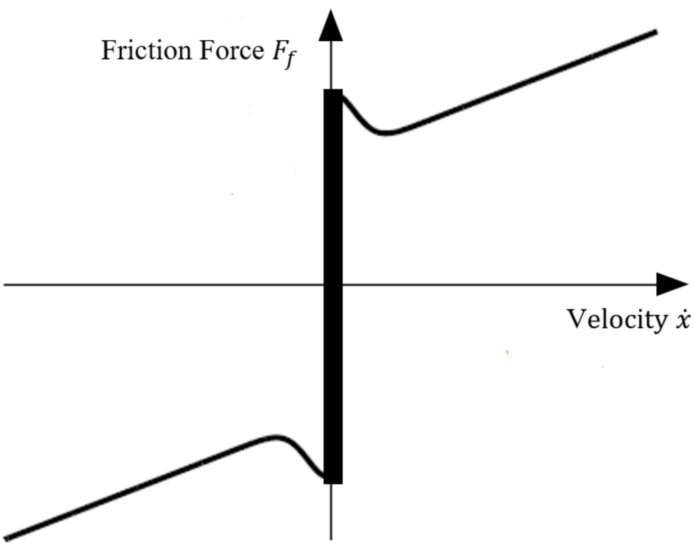

Figure 1.6 The Stribeck curve.

These Coulomb and Stribeck methods are impractical for friction compensation at motion stop and inversion, where stick-slip could arise, and discontinuity occurs.
Another model that tries to overcome the zero-velocity problem is presented in [8] where Lentini et al. proposed a static solution based on the Karnopp and Stribeck models.

$$F_f = \begin{cases} F(v), & |v| \geq \varepsilon \\ F_{ext}, \quad |v| < \varepsilon, & |F_{ext}| < F_s \\ F_s\, sign(F_{ext}), & otherwise \end{cases}$$

$$F(v) = \begin{cases} sign(v)F_{c1} + sign(v)(F_s - F_{c1})e^{-\left(\frac{|v|}{V_s}\right)^{\delta}} + c_1 v \\ sign(v)F_{c2} + c_2 v \end{cases}$$

Where F_s is the breakaway force, v_s is the Stribeck velocity, δ is a geometry dependent parameter, F_{C1} and F_{C2} stand for the Coulomb friction for increasing and decreasing speed, c_1 and c_2 are the viscous term for increasing and decreasing velocity respectively while ε is the Karnopp threshold that is needed to overcome the zero-velocity numerical problem.

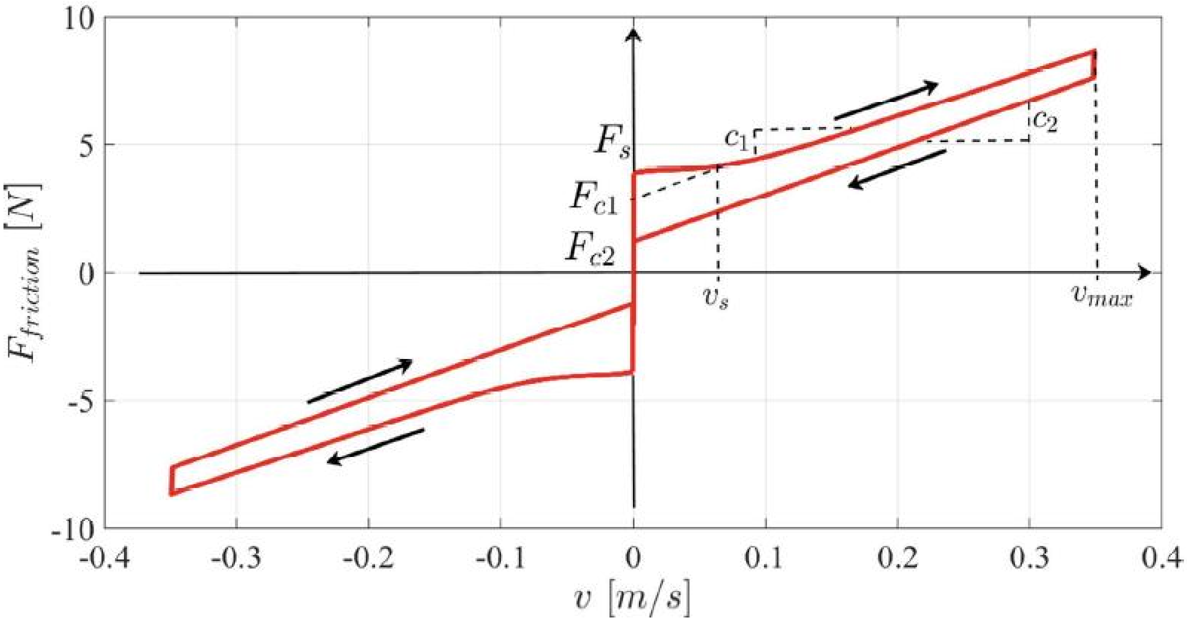

Figure 1.7 Friction model presented in [8].

A novel view about the contacts between the surfaces of two bodies: to overcome the problem due to the asperity deformation an analogy with the behavior of "bristles" was made. Asperities are now considered as some bristles with its own stiffness. Each asperity contributes to the total friction force as a spring would be. The change in the shape of each asperity is given by the stress-strain curve and they act as stiff beams deforming in the elasto-plastic field. Within a given applied load, the elastically deformed bristle adds a compliance and returns to its original position after the load is removed. Once the elastic resistance is overtaken, the entire brush moves, and a permanent displacement is produced [6].

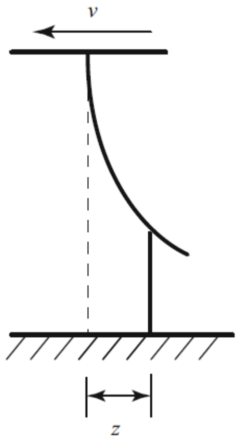

Figure 1.8 The bristle analogy [6].

The bristles idea was initially introduced in the Dahl model. The Dahl model attributes the origin of friction to the continuous formation and subsequent breaking of quasi-static bonds. These bonds give rise to a brush-like behavior, where the bristles of the brush bend in one direction during forward motion and then flop or bend in the opposite direction when the motion is reversed. The Dahl model is considered as a static model in which the presliding regime is not considered. For high velocities, the Dahl model exhibits similarities to Coulomb friction, which can be discerned by setting the derivative of displacement with respect to time (*dz/dt*) equal to zero. The main disadvantage of the Dahl model is its complexity that results in being highly computation-wise time-consuming and in generating high calibration costs [5].
The presliding friction has been approximated as a generalized first order model of the position x of the object. The sliding regime is approximated by a static friction F_s.

$$\frac{dF_f}{dx} = \sigma_0 \, sign\left(1 - \frac{F_f}{F_s}\right) \left|1 - \frac{F_f}{F_s}\right|^n$$

With σ_0 as the micro-stiffness, F_s the static friction force and n a shape factor.
The latter can be converted into an easier form for the numerical implementation:

$$\begin{cases} F_f = \sigma_0 \, z \\ \dfrac{dz}{dt} = v \; sign\left(1 - sign(v)\dfrac{\sigma_0 z}{F_c}\right) \left|1 - sign(v)\dfrac{\sigma_0 z}{F_c}\right|^n \end{cases}$$

With z the state variable interpreted as elastic deformation of surface asperities of adjacent bodies and v the sliding velocity but it does not correspond to any physical quantity, i.e., the parameters of this kind of model must be experimentally identified.

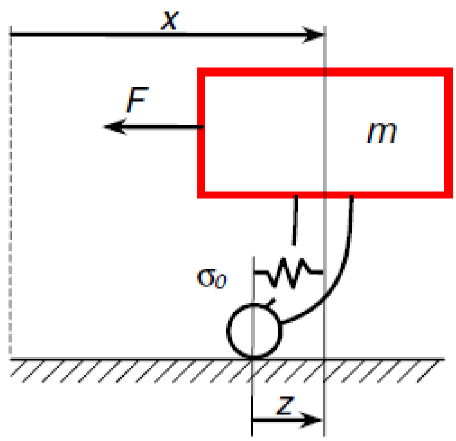

Figure 1.9 Representation of the variable z [5].

Notice that implicitly is assumed that σ_0 is time invariant. The Dahl model does not include the Stribeck effect nor stiction. Another disadvantage is that the Dahl model suffers from drift [9]. When the friction force is simulated by the Dahl model and an arbitrary small bias and small vibrations are put on the system it will drift, even though the applied force will stay below the break-away force. The reason for this drift is that the Dahl model only include a plastic component in its model when it describes the pre-sliding phenomenon. Not considering the elastic behavior of the asperities means that the value of the asperities deformation never resets.

Haessing and Friedland (1991) introduced two novel stick-slip friction models. One of them, called the Bristle model, aimed to depict the interactions occurring at the microscopic contact point between two surfaces. In this model, each contact point is conceptualized as a connection between pliable bristles. As the surfaces undergo movement, the strain within the bond intensifies. Consequently, the bristles function as springs, generating a force of friction.

$$F_f = \sum_{i=1}^{N} \sigma_0 \, (x_i - b_i)$$

With N the number of bristles, σ_0 the stiffness of the bristles, x_i the position of the bristles and b_i the location where the bond is formed. When the distance between $|x_i - b_i|$ equals δ_s, the bond breaks, resulting in the formation of a new bond at a random location relative to its previous position. However, the Bristle model has limited usage due to its computational inefficiency. To address this, Haessig and Friedland introduced the Reset Integrator model, which offers a more efficient approach to modeling friction. Rather than breaking the bristle, this model maintains a constant bond by halting the increase of strain at the point of rupture. To define the strain in the bond, an extra equation is proposed:

$$\frac{dz}{dt} = \begin{cases} 0 \ \ if \ (v > 0 \ and \ z \geq 0) \ or \ (v < 0 \ and \ z \leq 0) \\ \qquad\qquad\quad v \quad otherwise \end{cases}$$

The $\frac{dz}{dt}$ signal is fed to an integrator, to which the input is shut off according to the rules above. The friction force is then given by:

$$F_f = \left(1 + \alpha(z)\right) \sigma_0 z + \sigma_1 \frac{dz}{dt}$$

The term $\sigma_1 \frac{dz}{dt}$ is the damping term that is different from zero only in adhesion. Striction is realized by:

$$\alpha(z) = \begin{cases} a \ \ if \ (|z| < z_0) \\ 0 \quad otherwise \end{cases}$$

The variable z remains constant when the deflection reaches the z_0 value. At the same time, the friction force drops since *a(z)* is zero.
The main disadvantage of this model is that it requires detection of $z_0 > |z|$ that it is discontinuous.

Armstrong (1994) created a model that separates sticking and sliding into two different equations. The adhesion part is given by:

$$F_f = \sigma_0 \, x$$

While sliding is modeled by:

$$\begin{cases} F_f(v,t) = \left(F_c + F_s(\gamma, \tau_d) \dfrac{1}{1 + \left(\dfrac{v(t-\tau_t)}{v_s}\right)^2} \right) sign(v) + F_v \, v \\ F_s(\gamma, \tau_d) = F_{s,a} + \left(F_{s,\infty} - F_{s,a} \dfrac{\tau_d}{\tau_{d+\gamma}} \right) \end{cases}$$

The seven parameters that give the name to the model are: F_c the Coulomb friction force, F_v the viscous friction force coefficient, $F_{s,\infty}$ the magnitude of the Stribeck friction after a long time at rest, σ_0 the stiffness of the static contact, v_s the Stribeck velocity, τ_t the time-constant of the frictional memory, γ an empirical parameter. The other parameters are the dwell time τ_d, the rising static friction function $F_s(\gamma, \tau_d)$ and the value of the Stribeck friction at the end of the previous period $F_{s,a}$.
An important drawback is the requirement to initialize the states of the model whenever a switch occurs, necessitating a mechanism to govern this switching process. Whether the model can be classified as truly dynamic is a topic of debate. This is because it essentially combines two static relationships without inherent dynamics, even though it effectively describes phenomena related to dynamic friction.

In subsequent studies, dynamic models as the Lund-Grenoble (LuGre) model were introduced. “Dynamic model” means that both pre-sliding and gross sliding behavior are considered. The LuGre model is a modification of the Dahl model in which the pre-sliding regime is combined with the Stribeck curve $s(v)$ in sliding regime [10] and it is a bristle-based model. In order to describe the friction lag in sliding regime, that comes from hysteretic behaviors of the asperities, the authors introduced an internal state variable z and a first order nonlinear differential equation [11]:

$$\begin{cases} \dfrac{dz}{dv} = v - \sigma_0 \dfrac{v}{s(v)} z \\ s(v) = sign(v)\ (F_c + (F_s - F_c)e^{-\left|\frac{v}{V_s}\right|^{\delta}} \end{cases}$$

Where v is the velocity of the element under investigation, σ_0 represents the average bristle stiffness and $s(v)$ being the Stribeck curve, F_c is the Coulomb friction force, F_s is the stiction force, V_s is the Stribeck velocity and δ is an empirical factor called “the shape factor”.
Instead, the friction force comes up as a function of the velocity v and of the state variable z:

$$F_f = \sigma_0\, z + \sigma_1 \frac{dz}{dt} + \sigma_2\, v$$

With σ_1 as the micro-viscous friction coefficient and σ_2 representing the macroscopic viscous damping. The LuGre model is widely used and very popular in control applications despite the nonlinear properties. The model takes place mostly for identification, dissipative and adaptive control considerations [11].

From experimental trials it has been noted a hysteretic behavior during presliding regime. The Leuven model is a dynamic bristle-based model that tries to consider this response of the system during adhesion regime by adding a new term $F_h(z)$ that substitutes the first term of the LuGre model friction force equation. The identification of this term will be detailed further on during this study. This term appears during stiction and is function only of the position and does not depend on velocity. The remaining part of the LuGre equation is kept almost identical in the Leuven model a part of the state equation of the variable z.
The friction is identified with the following equation:

$$F_f = F_h(z) + \sigma_1 \frac{dz}{dt} + \sigma_2\, v$$

The parameter σ_1 and σ_2 are already descript in the LuGre model and v is the velocity.
Instead, the variable z comes from the state equation:

$$\frac{dz}{dt} = v\left(1 - sign\left(\frac{F_d(z)}{s(v) - F_b}\right)\left|\frac{F_{d(z)}}{s(v) - F_b}\right|^{n}\right)$$

$s(v)$ is the Stribeck curve, F_d is a point-symmetrical strictly increasing function of z, F_b is the value of the friction force at the velocity reversal and n is the Leuven shape factor determining the transformation between the state variable z and the position of the moving mass. This equation will further modify to avoid some mathematical issues.
Instead, the parameter $F_h(z)$ that takes in account the hysteretic behavior during stiction, is given by:

$$F_h(z) = F_b + F_d(z)$$

This method presents more problem during his implementation respect to the LuGre method but is more precise due to the parameter that consider hysteresis.

The authors of the Leuven model also introduced the Generalized Maxwell-Slip (GMS) model as a response to a limitation of the LuGre model. The primary motivation behind developing the GMS model was to address the absence of nonlocal memory characteristics in the hysteresis behavior during the presliding regime.
In the GMS model, N elasto-sliding elements are connected in parallel. Each of these massless model shares the same input (velocity, force, or displacement) and dynamics model but possesses distinct parameter sets. Additionally, each individual friction model includes a logical state indicating whether the element is in a sticking or slipping state.
Each mass is characterized by its own maximum force W_i, a linear spring-constant K_i and a state variable δ_i that describes the position of the *i-th* element.

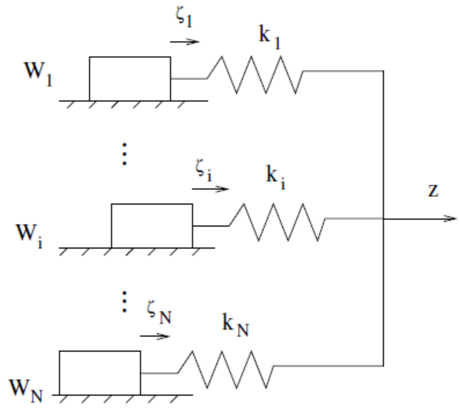

Figure 1.10 Maxwell slip model configuration [11].

The physics of each elementary mass are determined by the following rules:

$$\begin{cases} \dfrac{d\delta_i}{dt} = v \quad if\ \delta_i < s_i(v)\ in\ adhesion \\ \dfrac{d\delta_i}{dt} = sign(v)\ C_i \left(1 - \dfrac{\delta_i}{s_i(v)}\right) \quad in\ sliding \\ s_i(v) = s_i\,(0) + \left(\, s_i(0) - s_i(\infty)\right)(e^{-\left(\frac{v}{V_s}\right)} - 1) \end{cases}$$

Where v is the common input for all the models (v stands for velocity in this case), δ_i is the *i-th* spring displacement, C is a parameter that determines how quick δ_i converges to $s_i(v)$ that is the i-th Stribeck velocity.
The friction force comes from the summatory of all the elasto-plastic models plus some parameters:

$$F_f(v) = \sum_{i=1}^{N} \left(k_i\,\delta_i + \sigma_i\,\dot{\delta}_i\right) + f(v)$$

Where $f(v)$ is the velocity strengthening component that usually is proportional to v to express the viscous friction. Inside the summatory the first term represents the elasto-sliding friction force while the second one is the viscoelastic part.
It is possible to obtain the basic Maxwell slip model replacing δ_i with $\frac{W_i}{k_i}$ and applying the Coulomb law for friction. The Maxwell slip model can be helpful in the Leuven method to approximate the hysteretic behavior.
The model's disadvantage lies in the substantial amount of experimentation required to determine the parameters. One approach to determine the model is by comparing the hysteresis loops produced by the N elements with experimentally derived hysteresis loops.

Two of the newest models about friction are The Non-Linear Regression (NLR) and Dynamic NonLinear Regression with direct application of eXcitation (DNLRX) techniques that are built upon the fundamental Maxwell Slip model. This underlying model incorporates nonlocal memory to capture presliding hysteresis but only offers a fixed sliding friction. Both the NLR and DNLRX models comprise N parallel elasto-slide elements that are weightless and experience identical displacement excitation $x(t)$.
If the absolute deformation of an element's spring, denoted as δ_i, is less than the threshold Δ_i ($|\delta_i(t)| < \Delta_i$), the element remains stuck. However, if the deformation exceeds the threshold, the element starts to slip, and the spring deformation is determined as $\delta_i(t) = \Delta_i$.

$$\delta_i(t) = sign\,[x(t) - x(t-1) + \delta_i(t-1)] \cdot min\{|x(t) - x(t-1) + \delta_i(t-1), \Delta_i\}$$

The whole system is in adhesion if at least one element sticks. The system slide when all the elements do.

- In the NLR model the friction force is given by:

$$F_f(t) = \sum_{i=1}^{N} k_i\ \cdot \delta_i(t)$$

- In the DNLRX model instead:

$$F_f(t) = \sum_{r=0}^{n_x} c_r \cdot x(t-r) + \sum_{r=0}^{n_\delta} \chi_r^T \cdot \delta(t-r)$$

The main drawback of the NLR model is that it only accounts for constant sliding friction.
To address the limitations of the NLR model, the DNLRX model is proposed as a modification of the linear component of the NLR model. In this modified model, the frictional force is allowed to vary based on both current and past values of spring deformations and displacements. This is achieved by passing the applied displacement *x(t)* through a Finite Impulse Response (FIR) filter with n_x coefficients c_r (where r = 0, . . ., n_x), and the spring deformation vector *δ(t)* through an *N*-dimensional FIR filter with n coefficients θ_r (where r = 0, . . ., n).

$$\delta_t = [\delta_1(t), \dots \delta_N(t)]^T$$

Here is the list of all the parameters: *N* is the number of elements, *x(t)* is the displacement input, k_i the stiffness of the *i-th* element, Δ_i is the maximum spring deformation before the *i-th* element start moving, χ_r is the vector of coefficient for spring displacement FIR filter, n_δ is the spring displacement FIR filter order, c_r are the coefficients of displacement FIR filter, n_x is the displacement FIR filter orders, δ the spring deformation vector while δ_i is the *i-th* spring deformation.
The initial component of the DNLRX equation introduces the capability for friction to be influenced by the history of displacements, as well as incorporating viscous friction and frictional lag. This is achieved by numerically differentiating the displacement to obtain the velocity. The second part of the equation considers the dependence of friction on both present and past values of spring deformations, which can be seen as a discrete-time representation of the micro-viscous effect. Again, the velocity is obtained by numerically differentiating the spring displacement.
However, there are certain limitations to the model. It fails to capture the Stribeck effect (velocity weakening), and the physical interpretation of the FIR coefficients is not straightforward. Nevertheless, the DNLRX model has been successfully identified and utilized for feedforward compensation.

1.2 Identification of the friction model parameters

The friction models parameters have not a physical meaning since they do not really exist, and they must be empirically found. In the literature there are many examples of experimental analysis of the friction models parameters. Those parameters also depend on each study case and must be evaluated before each experiment.
The authors of [11] tried to find the parameters of 4 types of friction models for a machine tool table system at low velocities. One of those 4 types is static (Stribeck modified), while the other are dynamics (Dahl, LuGre, Leuven).

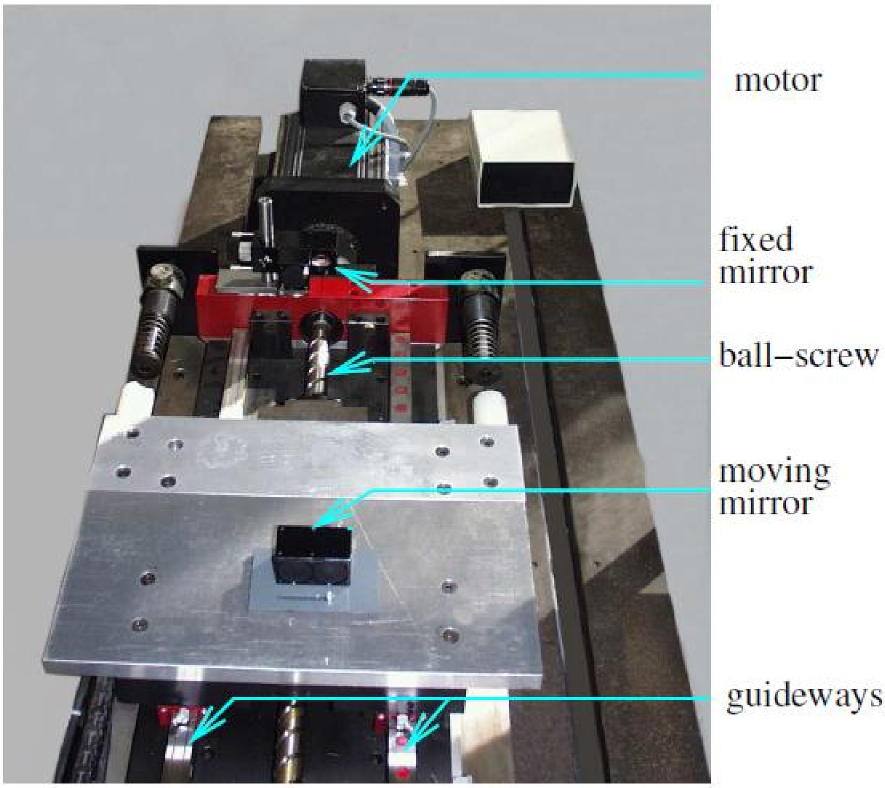

Figure 1.11 Experimental set-up in [11].

The experimental validation of the friction models is demonstrated in Figure 1, which illustrates the implementation of a linear table system for machine tools. This system comprises two recirculating-roller guideways, each equipped with two carriages, that guide and support the table. All the bearings utilized in this setup are of the rolling-element variety. Connecting the table to a screw is a 50-mm pitch-size ball-screw, which, in turn, is directly linked to the rotor of a brushless permanent magnet servo motor (specifically, the Parvex LD840EE model) using a rigid coupling, without incorporating any form of reduction mechanism.

The position of the table is measured using a Renishaw interferometer. This measurement is based on determining the relative distance between two mirrors, with one mirror fixed to the frame and the other attached to the table. To control the system, a voltage input is provided. This voltage is converted by the motor's current amplifier into a current signal that is directly proportional to the applied force on the rotor.

In the case of the static model, the friction equation was:

$$F_f = \sigma_2\, v + sign(v)\, (F_c + (F_s - F_c)e^{-\left|\frac{v}{V_s}\right|^{\delta}}$$

All parameters have been already stated and the formula is like the Stribeck model but with the sum of $\sigma_2 v$, where v is the velocities and σ_2 the macroscopic viscous damping (the same of LuGre and Leuven). To determine the parameters of this static model, various constant velocities are applied to the system utilizing a position and velocity feedback controller with low gain. Due to the constant velocity, the inertial forces are negligible, causing the friction force to be equal to the applied force.

The friction force associated with each measurement point is obtained by averaging data samples collected during five experiments.

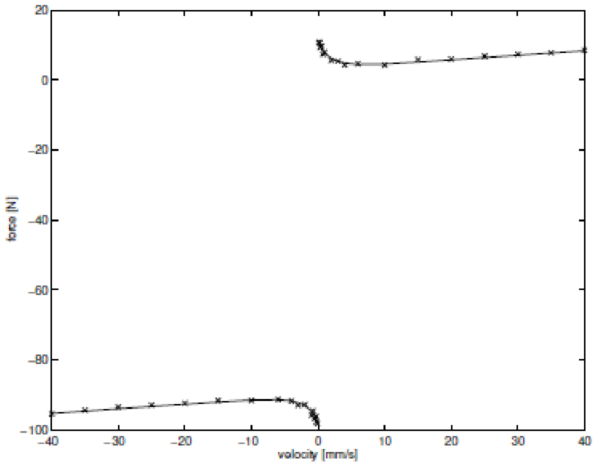

Figure 1.12 Result of the static model in [11].

In the figure the cross are the measured points while the curve is the one that fit better those points using a nonlinear least squares identification algorithm.

In Leuven model the hysteretic behavior, descript in $F_h(z)$, must be find. Obviously, the variable z can not be directly measured. To bypass this problem, it is possible to approximate z with the micro-displacement x of the mass. Evidently this approximation can work only if the system stays in the adhesion regime. At this point, a periodic signal at low frequency with low amplitude is applied to the system. The theory of the Maxwell slip model is applied to model the hysteresis curve and several elements are defined (in this case 10) and the maximum force W_i and linear spring-constant k_i of each element is identified using curve-fitting techniques.

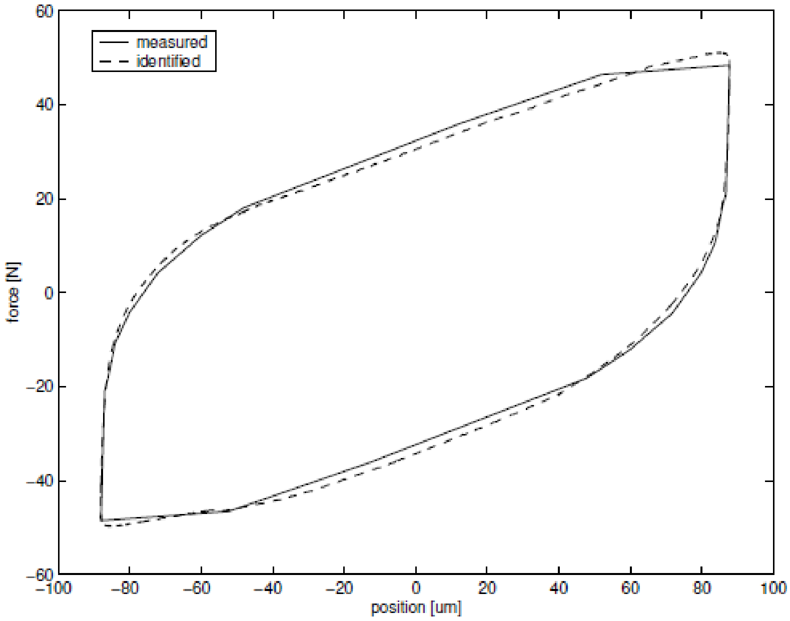

Figure 1.13 Measured and estimated curve in [11].

The remaining parameters (σ_0, σ_1 and n) have been identified by minimizing the peak tracking error.

Another approach was made by the authors of [12]. The aim of their studies was to find the parameters of the same friction models of [11]: one static model and 2 dynamic models (Dahl and LuGre).
The primary components of the experimental setup are a ball screw, a motor, and a brass block. The ball screw and the motor shaft are linked together using a beam coupler. To monitor the shaft's movement, an optical encoder is utilized. A thin metal plate is fastened to the ball screw nut to transmit the longitudinal motion to the brass block. To prevent any bending during the experiments, a load cell creates a sturdy connection between the thin metal plate and the brass block. The micrometer head is employed to calibrate a specialized high-sensitivity sensor, which is essential for determining parameters in the LuGre model.
The beam coupler facilitates the transfer of rotary motion from the shaft to the ball screw shaft. As a result, the ball screw nut undergoes linear movement along the longitudinal axis. The metal plate, known for its high stiffness, combined with the load cell, guarantees precise reproduction of one-dimensional sliding motion on the brass block. The load cell is employed for the continuous measurement of either the tension or compression force exerted on the brass block. To gauge the linear displacement of the mass, an optical encoder is utilized.
Accurately measuring the micro-displacement of the block prior to significant sliding has long been a recognized obstacle for encoder-based displacement sensing systems. This displacement, commonly referred to as pre-sliding, plays a crucial role in the identification process of the LuGre model and typically occurs at a scale of a few micrometers. To capture and record the pre-sliding of the block, a capacitance displacement sensor with exceptional sensitivity has been specifically designed and constructed.

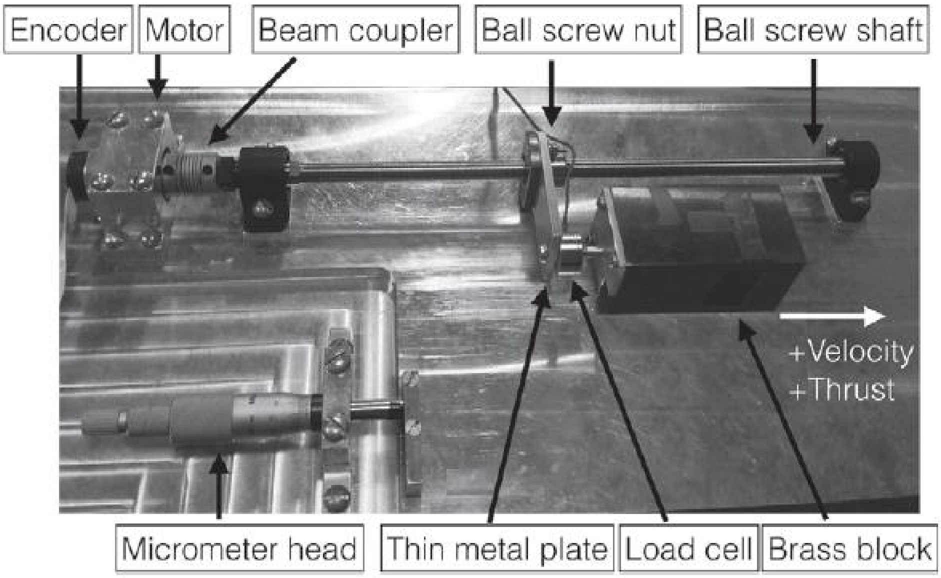

Figure 1.14 Experimental set-up in [12].

All the trials are carried out computing the friction force from the Newton's second law:

$$F_{ext} - F_f = m\,\ddot{x}$$

Where F_{ext} is the external force, m corresponds to the mass of the block and $\ddot{x}$ is its linear acceleration.
For the classical static model, the parameters F_c, F_s and σ_2 have been found going through two types of experiment: once wants to find the friction force at constant velocity while the other cares about the Coulomb friction force for which the block start sliding. The first experiment involves conducting 15 trials with varying desired velocities, ranging from v = ±2.0mm/s to ±5.5mm/s, using equal intervals of 0.5mm/s. A PID controller is used to control the velocity output and functions based on tracking error. In the steady state, the friction experienced by the block is equal to the force exerted on it because there is no acceleration. In the next step, the objective is to determine the maximum load that can be applied before the block start its dynamic motion. This is accomplished by conducting 13 trials, where the desired input force is assigned to a closed-loop force PID controller. After these two experiments, the Stribeck curve can be built.
Regarding the Dahl model, the parameters σ and F_c are identified through 16 trials in which the input excitation has a sinusoidal shape and it's regulated with a PID controller.

$$\frac{dF_f}{dx} = \sigma_0\, sign\left(1 - \frac{F_f}{F_s}\right)\left|1 - \frac{F_f}{F_s}\right|^n$$

In those experiments the parameters n and the $sign\left(1 - \frac{F_f}{f_s}\right)$ are considered equal to 1 while the remaining parameters have been found through the least squares method on Matlab to find the best fitting curve. The parameters identified within the positive and negative velocity regions are averaged out to obtain the nominal parameters.
With respect to the LuGre model, 6 parameters must be found but 4 comes from the Stribeck curve that has been already detected during the static model experiment. The remaining "dynamic" parameters σ_0 and σ_1 are identified during 6 trials. A force is applied thanks to a PID controller that

also operates on tracking errors. The time series of the micro-displacement resulting from each trial contributes to one set of the dynamic parameters. The displacement is sensed by the capacitance sensor, and it is related to the known force applied. In the pre-sliding regime, the approximation $z = x$ has been made to obtain the following equation:

$$F_f = \sigma_0 \, x + \sigma_1 \frac{dx}{dt} + \sigma_2 \, v$$

Substituting the latter inside the Newton's second law it is possible to directly compute σ_0 because, after some mathematical simplification, the equation:

$$F_f = \sigma_0 \, x + (\sigma_1 + \sigma_2) \frac{dx}{dt} + m \, \ddot{x}$$

Can be reduced to:

$$F_f = \sigma_0 \, x$$

The different values of σ_0 coming from the different trials are averaged and a final value of σ_0 is obtained.
Once σ_0 has been identified, the value of σ_1 is calculated from the not simplified Newton's second law equation.
In the studies carried on in [13] the experimental arrangement consists of two friction pads (1) that exert pressure on a mobile mass(2). This mass is supported by two thin steel sheets (3), which provide the spring force. The mobile mass is composed of AISI 1018 steel, while the friction pads are made from automotive carbon brake pads. Despite being commonly used for sliding contact purposes, these materials are suitable for bristles-based applications because of the flat contact surfaces. An electrodynamic shaker is directly connected to the mobile mass using a stinger. Additionally, the design incorporates two piezoelectric stack actuators (4), enabling the real-time adjustment of the normal force.

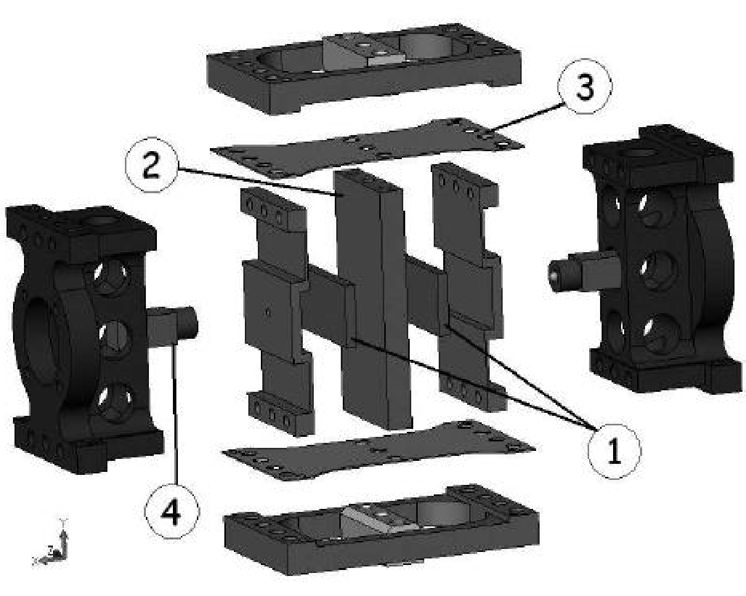

Figure 1.15 CAD model of the damper in [13].

An impedance head measures the force and acceleration while the input vibrational behavior comes from 2 different vibration shakers.

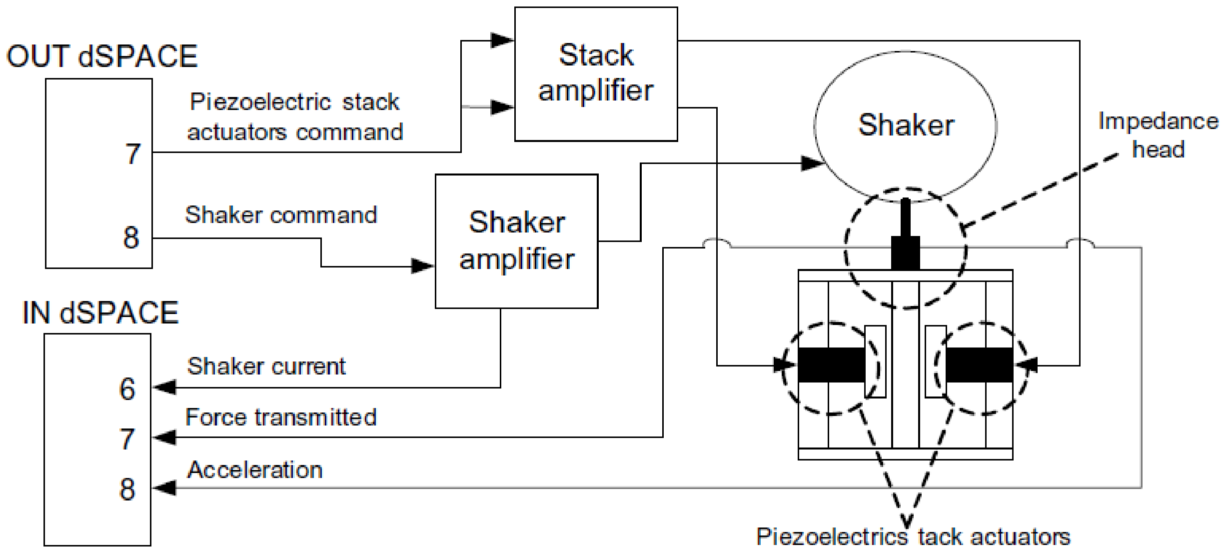

Figure 1.16 Block diagram of the experimental set-up in [13].

The friction force is indirectly computed measuring the displacement x, the velocity v, the acceleration $\ddot{x}$ and the external force F_{ext}:

$$F_f = -m\ddot{x} - c\,v - k\,x + F_{ext}$$

The evaluation of the external force is not trivial because the force is not directly applied on the mass. To avoid this problem the external force is computed assuming a single degree of freedom system (SDOF) of this type:

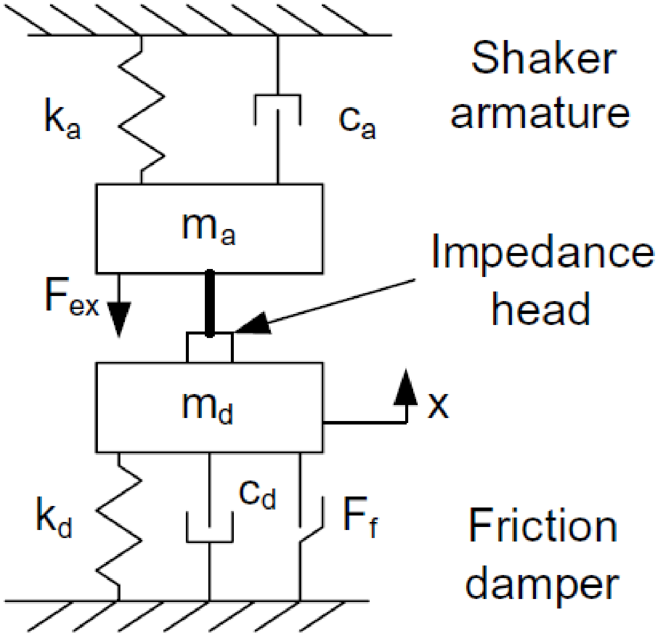

Figure 1.17 The SDOF used in [13].

The identification of the mass, stiffness and damping of the SDOF is fundamental to compute the friction force. To acquire the accelerance transfer function, a dual channel analyzer was utilized. This function corresponds to the relationship between the input current applied to the shaker and the accelerometer signal measured from the impedance head installed on the moving mass. Notably, this measurement was obtained in the absence of any friction force. The authors employed two distinct vibration shakers to confirm that the parameters of the friction model remain consistent regardless of the specific vibration shaker used. Consequently, these parameters remain independent of the system parameters determined without the presence of friction. To determine the parameters of the SDOF, a second-order identification procedure was employed.

Now that the system is complete, it is possible to look for the LuGre parameters. First, it is necessary to find the Frequency Response Function (FRF) of the system in pre-sliding regime. The FRF was obtained applying a white noise with a certain amplitude and contemporarily measuring the friction force. To identify the static parameters of the LuGre friction model, a harmonic forcing function was generated using the shaker. This specific function was designed to induce a stick-slip response from the friction damper. The stick-slip regime was chosen because it provides a distinct visual representation of the bristles.

By introducing micro-slip oscillations, the stick-slip regime enables the examination of the bristles' stiffness and damping characteristics. These oscillations are closely associated with the behavior of the bristles themselves.

In the specific case of pneumatic cylinders, Raparelli et al. in [14] tried to find experimentally a trend of the friction coefficient by for the contact between seal and cylinder without passing through the numerical models parameters listed before.

The experimental set-up for the identification of the friction force mimics a typical piston-bore configuration, and the seal being tested operates under realistic conditions. Both the piston seal and the bore were lubricated to mimic standard working conditions.

The piston is housed within a reciprocating bore controlled by a crosshead connected to the rod of a hydraulic cylinder. The pneumatic cylinder bore is linked to the hydraulic cylinder rod through a load cell. The crosshead, which runs on longitudinal slides, guides the cylinder, preventing the transducer from bearing its weight. Two electric limit switches allow for cylinder stroke adjustment up to a maximum value. The test rig is equipped with sensors for load, pressure, and speed, as well as an automatic data acquisition system. Air enters the piston chamber through the hollow rod attached to the piston. Sealing is achieved by the test seal on one end and by an aerostatic bush on the other end. The aerostatic bush maintains chamber pressure without introducing significant friction forces. The motion between surfaces is achieved through the sliding action of the cylinder bore due to the hydraulic cylinder. Guide rings at both ends of the piston ensure proper positioning of the piston within the bore. The holes located to the left of the aerostatic bush allow for air exhaust upstream of the left guide rings.

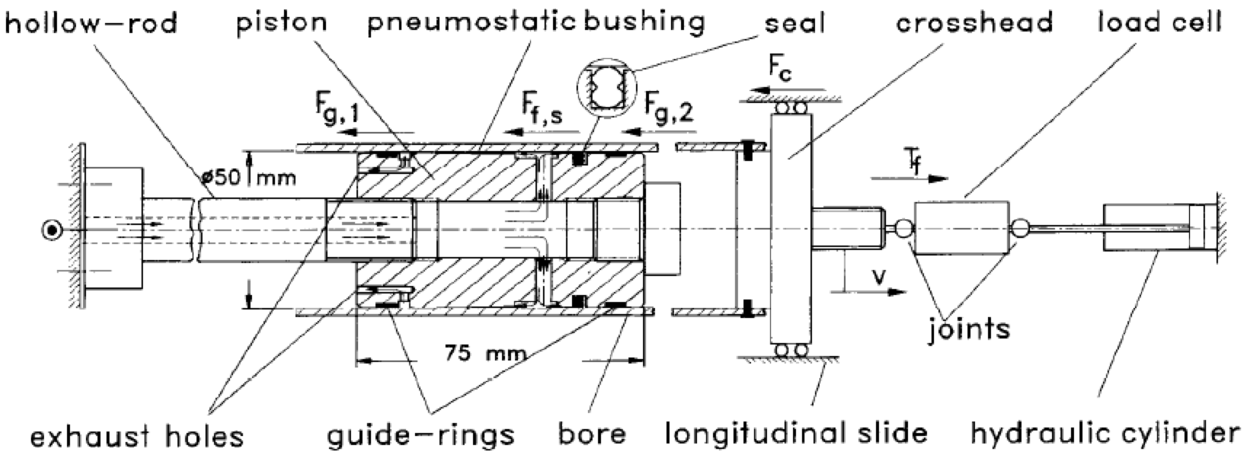

Figure 1.18 Experimental set-up used in [14].

All the forces acting on the system are sketched in the set-up image. $F_{g1,2}$ are the reaction forces due to the presence of the guide-rings, F_c corresponds to the crosshead reaction and $F_{f,s}$ is the friction force due to sealing. The friction force will result from the difference between the force acting on the cylinder T_f and the force T'_f. In the first case, T_f is measured considering the presence of the seal, instead T'_f comes from measurements without the sealing.

$$F_f = T_f - T_f'$$

Another experimental test was made to find the friction coefficient of the seal. Through this test, it became feasible to quantify the friction coefficient between a test specimen and a standard moving surface as a function of velocity. The testing arrangement comprises a moving plate that is activated by a pneumatic cylinder. The seal being tested is pressed against the plate with a specific load, resulting in contact pressures equivalent to those anticipated at the seal-bore interface during the experimental friction test.

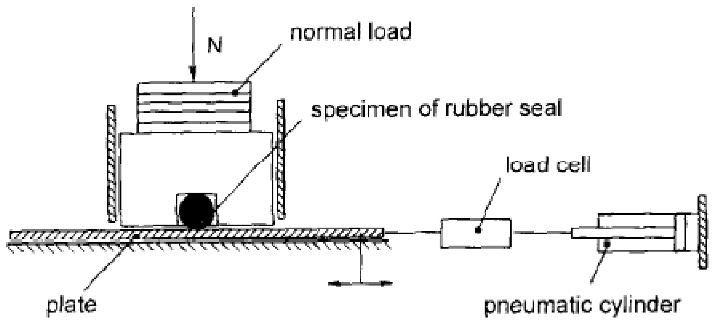

Figure 1.19 Test set-up for friction coefficients [14].

In these tests, a sliding plate is employed to simulate the bore wall utilized for the friction test. The roughness of the plate was assessed using an instrument equipped with a sharp-pointed stylus, which traced the surface profile irregularities. The measured roughness represents the average of three readings taken at 120° intervals around the cylinder bore. It is worth noting that the grease used for these tests is identical to the one employed in the friction force test. The tests were conducted under dry conditions, evaluating both boundary and fluid lubrication scenarios.

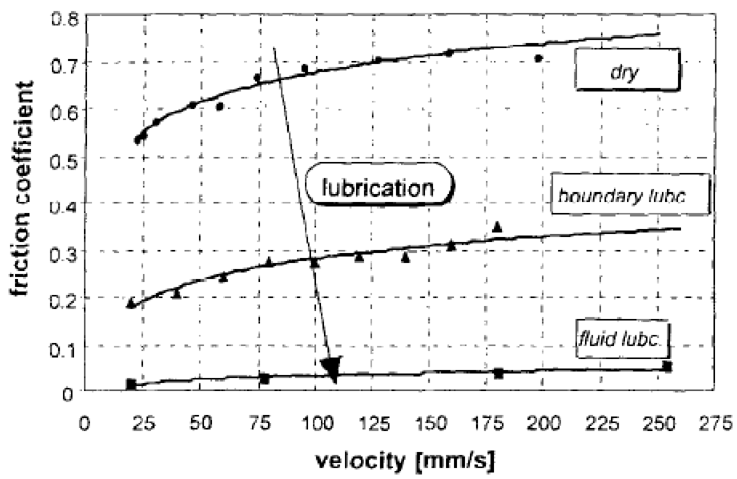

Figure 1.20 Friction coefficients in [14].

The following figures show the measured friction force by varying the speed and the pressure in the chambers at constant level of lubrication.

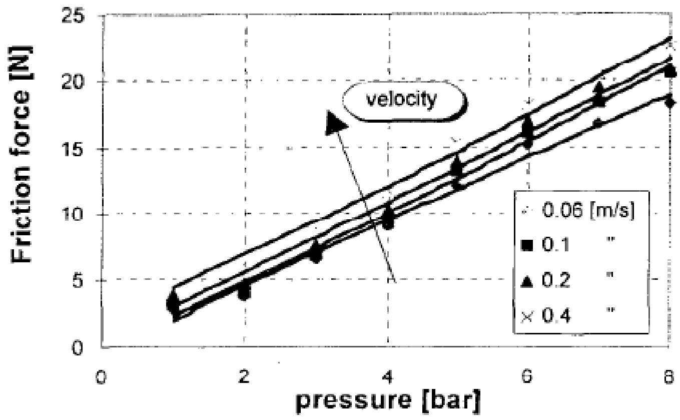

Figure 1.21 Friction force-Pressure in [14].

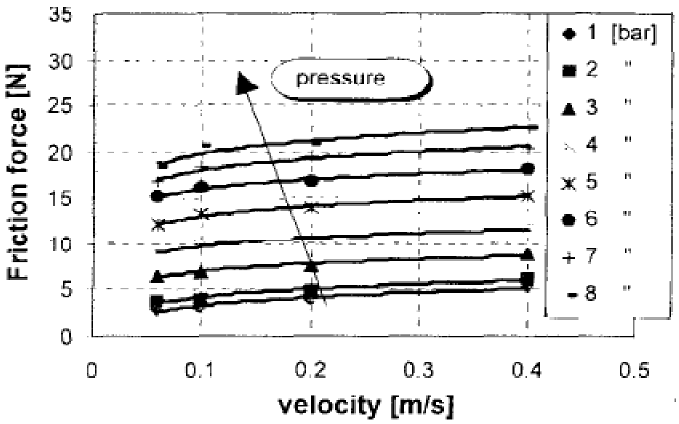

Figure 1.22 Friction force-velocity in [14].

CHAPTER 2

This chapter describes the typical physical phenomena related to friction that are usually experienced in dry and lubricated contacts. The chapter also describes some lumped parameter friction models that are currently used in Literature: Polito, Dahl, LuGre and Leuven models. These mathematical frameworks can be classified as static or dynamic models. The static models (Polito) do not include a state equation to simulate pre-sliding, while the dynamic ones (Dahl, LuGre, Leuven) do. Those models need a time-advanced scheme to obtain a time evolution of the model during time, i.e., implicit Euler, explicit Euler, and software solvers already implemented in Matlab.

2.1 The friction phenomenon

Friction is a phenomenon that occurs whenever two surfaces are in contact and there is an attempt to slide one surface over the other. It manifests as a force that opposes to the relative motion between the surfaces. Depending on the intensity driving force, it is possible to distinguish a presliding and a gross sliding regime. The pre-sliding regimes characterized by the presence of microscopic deflections of the asperities of the mating surfaces. Once the applied force exceeds the breakaway force and the object starts to move, the friction between the surfaces transitions from static to gross-sliding friction. This friction force opposes the motion of the object that's already sliding. Understanding the transition from pre-sliding to gross-sliding is important in engineering and various practical applications. Each of the three regimes (pre-sliding, transition and gross-sliding) has a strong dependance on a physical quantity: position for pre-sliding, position-velocity for transition and velocity for gross-sliding.

In pre-sliding conditions, the phenomenon of hysteresis occurs. It appears in various scientific and engineering contexts. Hysteresis describes the lagging or delayed effect of a system's output, especially in response to changes in the system's input. In simple terms, hysteresis refers to a situation where the current state of a system depends not only on its current input but also on its history.

Hysteresis is a complex phenomenon that arises from the interplay of various factors, including energy dissipation, material properties, and system dynamics. It's a fundamental concept in physics, engineering, and materials science, and understanding hysteresis is crucial for designing and analyzing systems that involve cyclic or history-dependent behavior. Hysteresis in the context of friction due to asperity deformations or bristle deformations refers to the phenomenon where the frictional force between two surfaces depends not only on their relative velocity but also on their history of interaction. In other words, the friction force doesn't only depend on the instantaneous conditions but also on the past conditions the surfaces have experienced. This is called hysteresis with non-local memory. Hysteresis with non-local memory involves that the future friction force values at a particular point in time being influenced by more than just its current value at that specific moment and the ongoing displacement. It also considers the past extreme friction values.

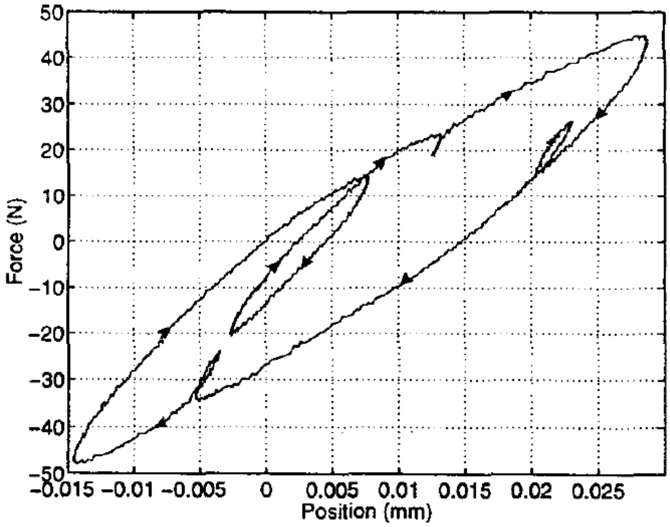

Figure 2.1 Hysteresis phenomenon in [15].

When two rough surfaces come into contact, such as in the case of solid-solid interactions, the actual contact points are the asperities on the surfaces. These contact points can deform and interact in complex ways, leading to hysteresis effects in friction. Similarly, in cases involving flexible bristle-like structures, their deformation and interaction with a surface can lead to similar hysteresis behavior. As two surfaces come into contact and relative motion occurs, the contact points experience forces that cause them to deform. During loading (when the surfaces approach each other), the asperities or bristles are compressed. This compression contributes to the frictional force opposing the relative motion. However, even after the surfaces start moving apart, the asperities or bristles may not immediately return to their original state due to factors like material deformation and adhesion. This delayed or incomplete recovery during unloading leads to hysteresis. The frictional force during the motion will depend not only on the current relative velocity but also on how the contact points were deformed during previous cycles of loading and unloading. This dependence on the history is the trademark of hysteresis. It means that the friction force can be different when the same relative velocity is reached during the loading phase compared to the unloading phase. Modeling and understanding hysteresis in friction due to asperity or bristle deformations can be quite challenging due to the intricate nature of the interactions.

When the body starts its motion, in between the pre-sliding regime and the gross-sliding regime, a transition phase appears. During this stage the phenomena of stick-slip can happen. It occurs when two surfaces in contact experience a combination of static friction and kinetic friction, leading to irregular motion. It is commonly observed in various mechanical systems and natural phenomena. When two surfaces are in contact, static friction prevents them from sliding against each other if the applied force is not sufficient to overcome this frictional force. However, when the force exceeds the threshold of static friction, the surfaces begin to move relative to each other, transitioning into the gross-sliding regime.

To simulate the stick-slip condition of the rod-piston-carriage system, an MSD system was developed. This system is commonly used in the literature to study the stick-slip behavior in both dry and lubricated friction. This model simplified the mechanical structure of a pneumatic cylinder. It is possible to consider the piston as a mass that slide on a surface: the friction between them will simulate the friction acting because of the seal on the exit hole of the piston and the seal between piston and rod.

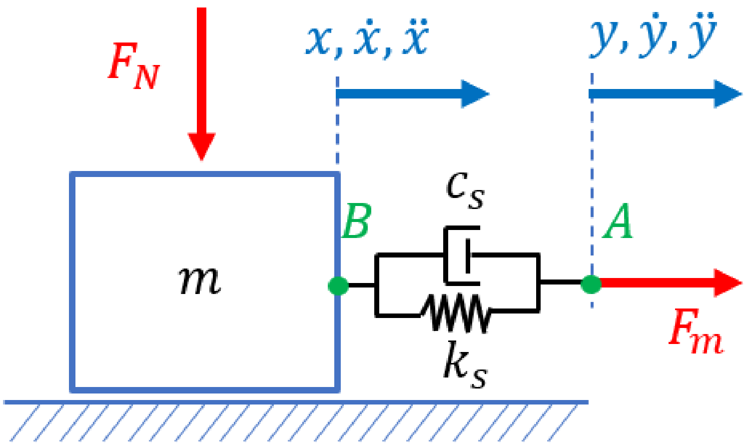

Figure 2.2 The SDOF used in the simulation.

The normal force F_N is an equivalent force depending on the difference in pressure between the two chambers and from the average pressure inside the chambers. The mass is linked to a spring and a damper through which the motion happens. In this way the mass can be easily pulled with a constant velocity. The assumption of constant velocity is necessary to simulate the stick and slip behavior.

The FBD relative to the mass can be represented in the following figure:

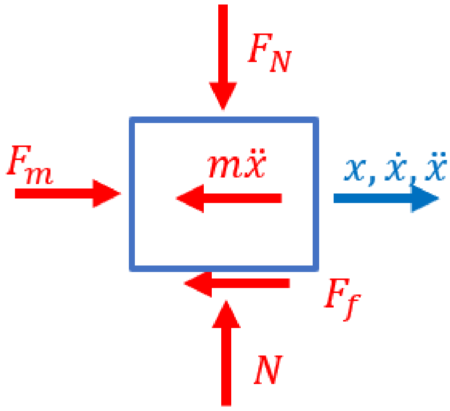

Figure 2.3 The FBD of the mass.

Where N is the normal reaction of the contact surface, F_N an equivalent normal force due to the mass weight and chamber pressures, F_m is the driving force, F_f corresponds to the friction force while $m\ddot{x}$ is the inertial term containing the mass m and the acceleration $\ddot{x}$. All these forces can be collected in the Equation of Motion given by the equilibrium of the forces along the horizontal axes:

$$F_f = F_m - m\ddot{x}$$

The driving force is produced by the difference in displacement between the reference system (x,$\dot{x}$,$\ddot{x}$) of the mass and the reference system of the driving force position (y,$\dot{y}$, $\ddot{y}$). The amplitude of this force is proportional to the stiffness of the spring and to the damping coefficient of the damper.

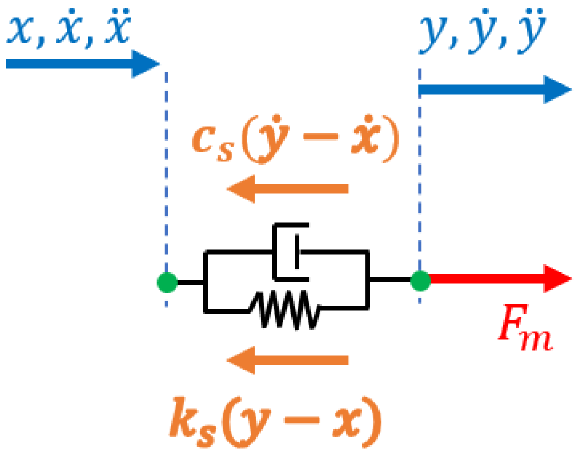

Figure 2.4 Representation of the driving force F_m.

If we consider c_s the damping factor and k_s the stiffness, as it is shown the figure, the driving force is given by the following equation:

$$F_m = c_s(\dot{y} - \dot{x}) + k_s(y - x)$$

This formula can be included in the previous formula of the Equation of Motion for the MSD system.

$$F_f = c_s(\dot{y} - \dot{x}) + k_s(y - x) - m\ddot{x}$$

In our study the assumption of no damping factor is implemented. That means that the driving force depends only on the spring deformation. The latter formula will be the core of the time-advanced scheme that are used in the numerical simulation. During the comparison with experimental results, the driven force will be given by the pressures inside the chambers of the pneumatic cylinder. Assuming a constant driving velocity for the MSD previous described, the position during time presents this behavior:

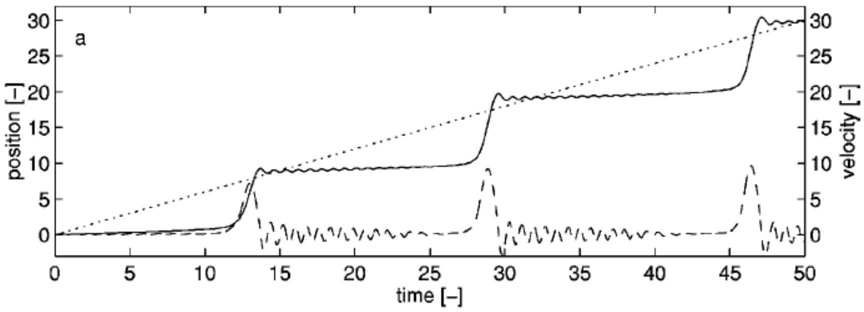

Figure 2.5 Stick-slip showed in the position-velocity chart in [16].

During stick-slip behavior, the surfaces alternate between periods of sticking (static friction dominates) and slipping (kinetic friction dominates). Initially, the applied force gradually increases until it overcomes static friction, causing a sudden release of stored energy. This results in rapid acceleration of the sliding surfaces, leading to slipping. However, as the surfaces move, kinetic friction comes into play, gradually reducing the speed and eventually bringing the motion to a stop. Once, the motion ceases, static friction takes over again, preventing further sliding until the applied force surpasses the static friction threshold once more. This cyclic process of sticking and slipping continues, producing a characteristic oscillatory motion. Stick-slip behavior can be observed in various situations, such as in mechanical systems like brakes, clutches, and drilling processes. It is also prevalent in natural phenomena like earthquakes, where the accumulated stress between tectonic plates causes them to stick until it exceeds the frictional resistance, resulting in sudden slipping and seismic activity. Understanding and controlling stick-slip behavior is crucial in engineering applications, as it can affect the performance, efficiency, and safety of mechanical systems. Engineers often employ strategies to minimize stick-slip, such as lubrication, surface treatments, or optimizing design parameters to reduce frictional forces and promote smoother motion. In this thesis the lubrication will not be considered, and just dry friction will be analyzed.

When speed increases the transition regime ends and the gross-sliding regime occurs. Friction in the sliding regime is also known as kinetic friction or dynamic friction. In this case the asperities don’t have enough time to interact and friction completely depends on the relative speed between the two bodies and it is proportional to a viscous term. Understanding friction in the sliding regime is crucial for various applications, ranging from designing machinery to controlling the movement of mechatronics systems.

2.2 Numerical models

To simulate the described behavior due to friction force, some of the numerical models found in literature were implemented. Starting from static models as the Polito model and then implementing dynamic models that present a state equation as the Dahl, LuGre and Leuven model. Each of them as its peculiarity and different accuracy.

2.2.1 Polito

The Polito model, presented in [8], is a static model based on the Stribeck and Karnopp models. It presents a modification of the Stribeck curve: depending on the velocity sign, the coefficients characterizing the value of the friction force are different. This model tries to overcome the mathematical jump that the Coulomb friction model has when the velocity is null in the same way as Karnopp does.

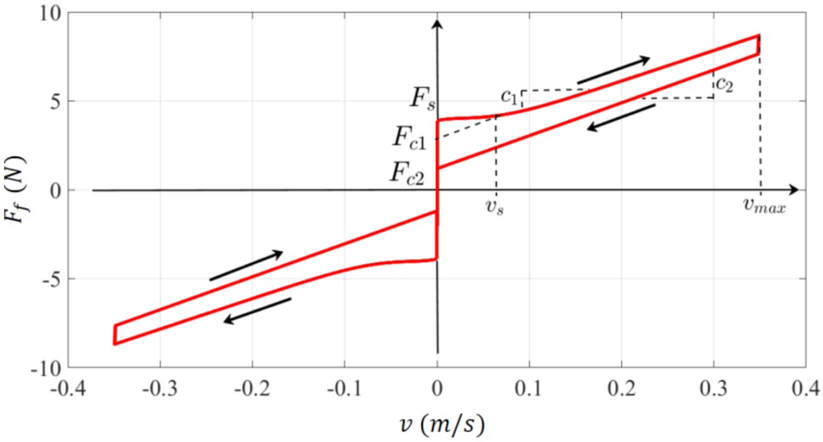

Figure 2.5 The Polito model curve showed in [8].

This model is relatively easy to implement but it presents some problems when it is developed with implicit time advanced scheme. Indeed, it is necessary knowing a priori the sign of the velocity and acceleration for each time step. This is not feasible and to overcome this problem some simplification can be done at the expense of the precision.

2.2.2 Dahl

The Dahl friction model is used in the modeling and simulation of mechanical systems [10], particularly in the field of control engineering and dynamics analysis. It is used to describe the frictional behavior of a system, especially in systems where accurate representation of friction is crucial for control or analysis purposes. The Dahl model is one of several models used to represent friction, each with its own level of complexity and accuracy. The Dahl model ascribes the source of friction to the continual formation and subsequent breaking of quasi-static bonds. These bonds give rise to a behavior of a brush, where the bristles of the brush bend in a specific direction during forward motion and then flex or bend in the opposite direction when the motion is reversed. The Dahl model is characterized as a dynamic model due to the presence of the state equation that describes $\dot{z}$. The model advantages definitely contain the relatively easy implementation and the dynamic nature of the model. The disadvantages are the accuracy also due to the presence of the drift phenomenon: the bristle deformation does not recover its elastic deformation causing a "drift" in the prediction of the displacement. It's important to note that while the Dahl model provides a simple representation of friction, friction itself can be quite complex and can exhibit nonlinear behavior in various situations. Therefore, more advanced models like the LuGre friction model or the Stribeck model are often used for more accurate representations of friction in complex systems.

2.2.3 LuGre

The Lund-Grenoble method is a popular friction compensator used in the field of robotics and mechatronics [10]. It is primarily employed to model and control friction phenomena in mechanical systems. This method is a numerical method that tries to simulate the friction behavior by exploiting the bristle theory. This is an approach to friction modelling in which the asperities between two surfaces in contact are represented by bristles with their own stiffness. This idea was first introduced in the Dahl model. The LuGre model puts a step forward respect to the Dahl model and modifies its equations. It consists of three main components: the Stribeck, viscous, and Coulomb friction elements. The Stribeck element accounts for the static friction and its dependence on velocity, while the viscous element represents the dynamic friction and its relation to velocity. The Coulomb element models the boundary condition of friction, describing the sudden transition between static and dynamic friction. The aim of this numerical simulation is to understand the trend of the MSD system previous detailed under low velocities condition through the LuGre method. This gives us the opportunity to highlight its behavior under stick-slip conditions. The LuGre model presents some advantages as it provides a nonlinear representation of friction that can capture complex friction behavior more accurately than simpler linear models, it includes separate components representing viscous and Coulomb friction, allowing it to capture different friction modes and the LuGre model can adapt to changing friction conditions in real-time is beneficial for control systems that require accurate friction compensation. The main disadvantages are the complexity of implementation and the parameters identification that can influence the accuracy.

2.2.4 Leuven

A more elaborated model was presented after the LuGre model [17]. The Leuven model is a modification of the LuGre model in which the term representing the friction part due to micro-stiffness of the bristles is replaced by an expression function of the deformation z that describes the hysteresis behavior at zero velocity. Considering hysteresis means to be more precise. Hysteresis is a real phenomenon despite the expression characterizing it, is function of a non-existing parameter as z. Through z it is possible to simulate this behavior that is not considered in the other models. The other two parameters inside the formula are the same of the LuGre model. Indeed, the Leuven model has the same difficulty in finding the viscous and micro-viscous parameters. Furthermore, the identification of the hysteresis expression, is very hard.

2.3 Time advanced schemes

To implement the listed numerical methods, they require a time-advanced scheme to discretize them on time. This scheme can be already implemented by a Matlab solver.

One of the easiest methods for the implementation of the friction models is the explicit Euler scheme. explicit Euler, also known as the forward Euler method, is a numerical method used for approximating the solutions of ordinary differential equations (ODEs). The method is relatively straightforward and involves approximating the solution of an ODE by taking small time steps and using a first-order

Taylor series expansion. Given an initial value problem in the form of a first-order ODE: $\frac{dy}{dt} = f(t, y)$ with an initial condition $y(t = 0) = y_0$ it is possible to identify a time step Δt of certain size. This step corresponds to the interval at which the approximation will be computed. The procedure starts with the initial condition y_0 and t_0 and approximate the solution at the next step $t_1 = t_0 + \Delta t$ using the formula:

$$y_1 \simeq y_0 + \Delta t \cdot f(t_0, y_0)$$

With $f(t_0, y_0)$ that is a function representing the derivative evaluated at the current time step. This process continues until the desired endpoint is reached. The explicit Euler method is easy to implement and computationally inexpensive when the chosen time step is not too small. However, it has certain limitations. One major drawback is that the method is only first-order accurate, meaning that the error introduced at each step is proportional to the step size Δt. Consequently, the method tends to accumulate errors over long integration intervals or when the step size is too large. Another limitation is that the explicit Euler method is not always stable for certain types of ODEs. If the ODE system is stiff (i.e., has rapidly varying components with different time scales), the explicit Euler method may produce inaccurate or oscillatory solutions. In such cases, more advanced numerical methods like implicit methods or higher-order methods such as the Runge-Kutta methods are often employed. Despite its limitations, explicit Euler remains a useful and widely used method for simple ODEs or as a building block for more sophisticated numerical methods. It provides a good starting point for understanding numerical integration techniques and their applications in solving differential equations.

Euler devised also an implicit method called the implicit Euler method, also known as the backward Euler method. It is another numerical method used for approximating the solutions of ordinary differential equations (ODEs). It is like the explicit Euler method but differs in the way it computes the approximation at each time step. While the explicit Euler method calculates the approximation at the next time step using the derivative evaluated at the current time and state, the implicit Euler method instead uses the derivative evaluated at the next time step. This makes the implicit Euler method an implicit scheme. As it was for the explicit Euler, given an initial value problem: $\frac{dy}{dt} = f(t, y)$ with an initial condition $y(t = 0) = y_0$. A time step size Δt is chosen, which determines the interval at which the approximation will be computed. Then, starting with the initial condition y_0 at time t_0 and approximate the solution at the next time step $t_1 = t_0 + \Delta t$ using the formula:

$$y_1 \simeq y_0 + \Delta t \cdot f(t_1, y_1)$$

Where $f(t_1, y_1)$ represents the derivative evaluated at the next time step t_1 and an unknown value y_1. This equation is typically nonlinear and may require numerical techniques such as iteration or root-finding algorithms to solve it. Once y_1 is determined, the process is repeated to compute the approximation at the next time step.

The key difference between the implicit Euler method and the explicit Euler method lies in the implicit nature of the former. In the implicit Euler method, the approximation at each time step depends on the unknown value of the next time step. This means that each step requires solving an equation, which can be more computationally demanding compared to the explicit approach.

However, the implicit Euler method has some advantages over the explicit counterpart. Firstly, it is unconditionally stable for linear, time-invariant systems, meaning that it can handle stiff equations and larger time steps without stability issues. It is possible to demonstrate this advantages respect to the explicit Euler inserting the same time step for the two methods imposing the same input data and signal. The chosen time steps are:

$$time\ step1 = 10^{-5}$$
$$time\ step2 = 10^{-3}$$

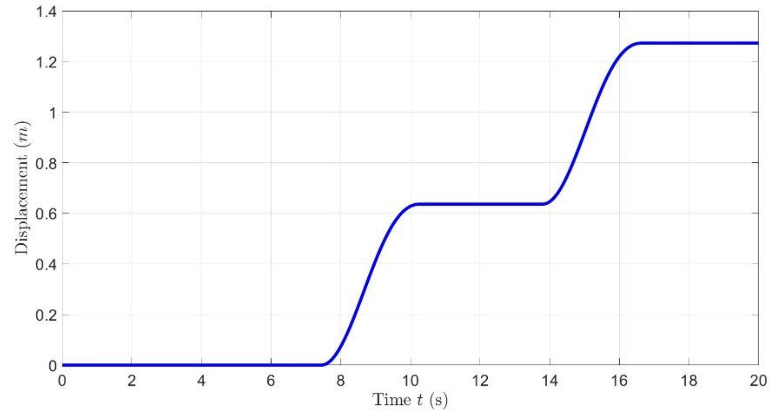

Figure 2.6a Explicit Euler with time step1.

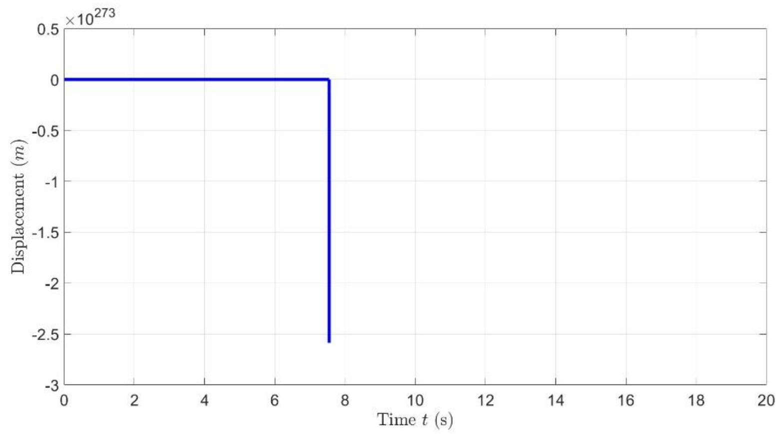

Figure 2.6b Explicit Euler with time step2.

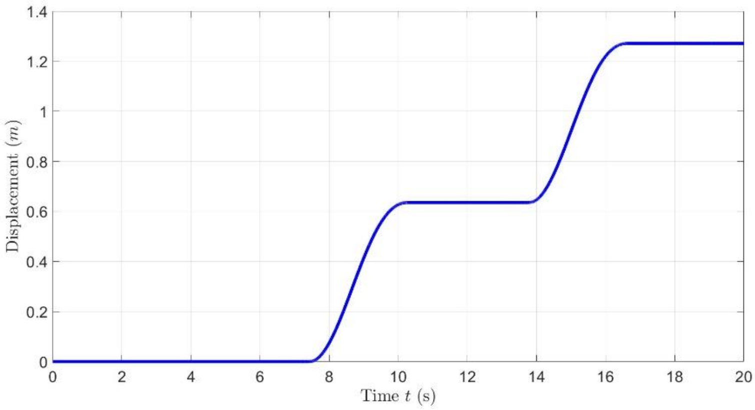

Figure 2.6c Implicit Euler with time step1.

It is possible to note that in the case of time step1, the time step is small enough to allow the correct displacement prediction by explicit Euler. In the second case the time step is much larger, and the explicit Euler diverge and cannot follow anymore the displacement of the body. Implicit Euler instead does not have this problem. Secondly, it is numerically more accurate for certain types of ODEs, especially those with rapidly varying components or oscillatory behavior. Nevertheless, the implicit Euler method also has its limitations. Solving the equation at each time step involves additional computational effort, especially for large systems of equations. Additionally, if the equation is highly nonlinear, convergence issues may arise, requiring more advanced numerical techniques. In summary, the implicit Euler method is a numerical scheme that provides stability and accuracy advantages over the explicit Euler method, particularly for stiff or oscillatory ODEs. However, it requires solving equations at each time step, making it more computationally intensive. The choice between the two methods depends on the specific characteristics of the problem at hand and the trade-off between computational cost and accuracy requirements.

The Runge-Kutta method is another numerical method used for solving ordinary differential equations (ODEs). It is a family of numerical integration methods that approximate the solution of an ODE by advancing the solution over small time intervals. Those methods can be either explicit or implicit. The most used variant of the Runge-Kutta method is the fourth order Runge-Kutta (RK4) method. In the RK4 method each next time step is given by the formula:

$$y_{k+1} = y_k + \Delta t \cdot \left(\frac{1}{6} f_1 + \frac{1}{3} f_2 + \frac{1}{3} f_3 + \frac{1}{6} f_4\right)$$

With:

$$f_1 = f(y_k, t_k)$$
$$f_2 = f\left(y_k + \frac{1}{2}\Delta t \cdot f_1, t_k + \frac{1}{2}\Delta t\right)$$
$$f_3 = f\left(y_k + \frac{1}{2}\Delta t \cdot f_2, t_k + \frac{1}{2}\Delta t\right)$$
$$f_4 = f(y_k + \Delta t \cdot f_3, t_k + \Delta t)$$

This process is repeated for subsequent time steps to obtain the numerical solution of the ODE. The RK4 method is known for its high accuracy and stability, making it a popular choice for solving ODEs numerically. It strikes a balance between computational efficiency and accuracy by using a combination of weighted averages of different derivative estimates. However, it is important to note that the RK4 method may not be suitable for all types of ODEs, especially those with stiff or highly oscillatory behavior, for which specialized methods may be more appropriate. Other variants of the Runge-Kutta method exist, such as RK3, which use similar principles but with fewer derivative estimates. This variant has lower accuracy but may be computationally faster in certain scenarios. The RK3 scheme can be described as:

$$y_{k+1} = y_k + \Delta t \cdot \left(\frac{2}{9} f_1 + \frac{1}{3} f_2 + \frac{4}{9} f_3\right)$$

Where the addends on the right-hand side are recursively defined by:

$$f_1 = f(y_k, t_k)$$
$$f_2 = f\left(y_k + \frac{1}{2}\Delta t \cdot f_1, t_k + \frac{1}{2}\Delta t\right)$$
$$f_3 = f\left(y_k + \frac{3}{4}\Delta t \cdot f_2, t_k + \frac{3}{4}\Delta t\right)$$

Overall, the Runge-Kutta method, particularly RK4, is a widely used and effective numerical technique for solving ODEs, providing a reliable approximation to the continuous solution of the differential equation.

The ode15s function in MATLAB is a solver designed to numerically solve stiff and non-stiff systems of ordinary differential equations (ODEs). The "s" in ode15s stands for "stiff," indicating its suitability for stiff systems. The ode15s solver is based on the Rosenbrock method, which is an implicit Runge-Kutta method. It combines the efficiency of implicit methods with the ability to handle stiff systems. It employs variable step sizes to adaptively control the accuracy of the solution and adjust the step size according to the stiffness properties of the system. To use ode15s, you need to define the system of ODEs you want to solve in MATLAB as a function of the form $\frac{dy}{dt} = f(t, y)$. Here, t represents the independent variable, i.e., time, and y is a vector representing the dependent variables. The function f should return a vector that contains the derivatives of the dependent variables with respect to the independent variable. The output of ode15s is the solution at specific time points stored in the vectors t and y. The vector t contains the time points at which the solution is evaluated, and the matrix y contains the corresponding values of the dependent variables. Ode15s is capable of handling stiff systems efficiently. It automatically detects stiffness in the system and adjusts the integration parameters accordingly. It uses an internal algorithm to estimate the Jacobian matrix of the system, which is necessary for solving stiff systems. The ode15s solver is part of MATLAB's ODE suite and provides a robust and versatile tool for solving a wide range of ODE problems. It is particularly useful when dealing with stiff systems, where explicit methods like ode45 may be inefficient or unstable.

Another Matlab solver for solving ordinary differential equation is ode45. It stands for "Ordinary Differential Equation 4th/5th order." ode45 is one of the most used solvers in MATLAB because of its versatility and robustness. It uses a combination of fourth and fifth order Runge-Kutta methods to approximate the solution of the ODE. The output of the solver gives two column vectors: one containing the time points at which the solution is computed and the other where each column represents the solution at the corresponding time point.The algorithm used by ode45 automatically adjusts the step size based on the error estimate, allowing it to handle both stiff and non-stiff systems of ODEs efficiently. For stiff systems, it employs a smaller step size to capture rapid changes, while for non-stiff systems, it takes larger steps to improve efficiency. ode45 is often a good choice for solving ODEs because it provides a balance between accuracy and efficiency. However, depending on the specific problem characteristics, other solvers like might be more appropriate. Overall, ode45 is a powerful tool in MATLAB for solving ODEs numerically and is widely used in various fields, including physics, engineering, biology, and mathematical modeling.

2.4 The numerical implementation

Polito

In the Polito model the friction force follows:

$$F_f = \begin{cases} F(v), & |v| \geq \varepsilon \\ F_{ext}, \quad |v| < \varepsilon, & |F_{ext}| < F_s \\ F_s\, sign(F_{ext}), & otherwise \end{cases}$$

$$F(v) = \begin{cases} sign(v)F_{c1} + sign(v)(F_s - F_{c1})e^{-\left(\frac{|v|}{V_s}\right)^{\delta}} + c_1 v & if\ \ddot{x} > 0 \\ sign(v)F_{c2} + c_2 v & if\ \ddot{x} \leq 0 \end{cases}$$

Where F_{ext} is the driving force, v the velocity, ε the Karnopp velocity, F_s the stiction force, F_{C1} and F_{C2} the Coulomb force (for positive and negative velocities), c_1 and c_2 are the viscous coefficient (for positive and negative velocities), v_s is the Stribeck velocity. The method is implemented only with explicit Euler for the reason previous detailed. A simplification is necessary to overcome the problem of knowing a priori the “k-th” acceleration:

$$\ddot{x}_k \simeq \ddot{x}_{k+1} = \frac{\dot{x}_{k+1} - \dot{x}_k}{\Delta t}$$

In this way it is possible to do the first choice depending on the sign of the acceleration. The function F(v) can be found. The friction force depends on the module of the velocity, but it is a known value that comes from the equation of motion of the body:

$$\dot{x}_{k+1} = \dot{x}_k + \frac{\left(F_{ext_k} - F_{f_k}\right)\Delta t}{m}$$

As consequence:

$$x_{k+1} = x_k + \dot{x}_k \Delta t$$

Of course, it needs initial conditions:

$$\begin{cases} x|_{k=0} = x_0 \\ \dot{x}|_{k=0} = \dot{x}_0 \end{cases}$$

Dahl

In the Dahl model instead, the friction force is obtained by:

$$F_f = \sigma_0 \, z$$

If we put this equation in the Equation of Motion of the MSD system:

$$\sigma_0 \, z = F_m - m\ddot{x}$$

This model needs a time advancing scheme to be implemented. In this thesis, the explicit Euler and the implicit Euler are taken in account. The developing on time of the phenomena is divided into "k-th" time steps.

- Applying the explicit Euler to the Equation of motion, it is possible to write:

$$\sigma_0 \, z_k = F_{m_k} - \frac{m}{\Delta t}(\dot{x}_{k+1} - \dot{x}_k)$$

With initial conditions:

$$\begin{cases} x|_{k=0} = x_0 \\ \dot{x}|_{k=0} = \dot{x}_0 \end{cases}$$

$$\begin{cases} z|_{k=0} = z_0 \\ \dot{z}|_{k=0} = \dot{z}_0 \end{cases}$$

The term z_{k+1} can be found from the state equation proposed by Dahl:

$$z_{k+1} = z_k + \Delta t \left(\dot{x}_k - \sigma_0 \, |\dot{x}_k| \frac{z_k}{F_c} \right)$$

- In a similar way it is possible to use the implicit Euler method, but it requires the application of a method that solves nonlinear equations. In this case the Regula Falsi method has been used.

$$\sigma_0 \, z_k = F_{m_k} - \frac{m}{\Delta t}(\dot{x}_k - \dot{x}_{k-1})$$

The remaining terms can be computed from:

$$x_k = x_{k-1} + \Delta t \, \dot{x}_k$$

$$z_k = (\Delta t \, \dot{x}_k + z_{k-1}) \left(\frac{F_c}{F_c + \Delta t \, \sigma_0 \, |\dot{x}_k|} \right)$$

$$\dot{z}_k = \frac{z_k - z_{k-1}}{\Delta t}$$

LuGre

The more complicated LuGre equations are typically formulated as a set of first-order differential equations. These equations incorporate various parameters that can be estimated or identified experimentally.

The friction force is described by:

$$F_f = \sigma_0\, z + \sigma_1 \frac{dz}{dt} + \sigma_2\, \dot{x}$$

This formula must be included in the Equation of Motion coming from the balance forces equation of the MSD system.

$$\sigma_0\, z + \sigma_1 \frac{dz}{dt} + \sigma_2 \dot{x} = F_m - m\ddot{x}$$

- Applying Explicing Euler to the acceleration term and indicating the "k-th" instant of time with the letter "k" the latter became:

$$\sigma_0\, z_k + \sigma_1 \dot{z}_k + \sigma_2\, \dot{x}_k = F_{m_k} - \frac{m}{\Delta t}(\dot{x}_{k+1} - \dot{x}_k)$$

Starting from some initial conditions, it is possible to find the unknown velocity $\dot{x}_{k+1}$ and therefore the position x_{k+1}:

$$\begin{cases} x|_{k=0} = x_0 \\ \dot{x}|_{k=0} = \dot{x}_0 \end{cases}$$

$$\begin{cases} z|_{k=0} = z_0 \\ \dot{z}|_{k=0} = \dot{z}_0 \end{cases}$$

On the other hand, the values of $\dot{z}_{k+1}$ and z_{k+1} come from the state equation:

$$z_{k+1} = z_k + \Delta t \left(\dot{x}_k - \sigma_0\, |\dot{x}_k| \frac{z_k}{g(\dot{x}_k)_k} \right)$$

With:

$$g(\dot{x}_k)_k = F_c + (F_s - F_c) \exp\left(- \left(\frac{|\dot{x}_k|}{v_s} \right)^{\delta} \right)$$

- It is possible to apply the implicit Euler formula using the same initial conditions of the previous case. This changes the Equation of Motion in:

$$\sigma_0\, z_k + \sigma_1 \dot{z}_k + \sigma_2\, \dot{x}_k = F_{m_k} - \frac{m}{\Delta t}(\dot{x}_k - \dot{x}_{k-1})$$

  This method is harder to implement due to the application of a method that solves nonlinear equations. In this case, the Regula Falsi method. Indeed, unlike explicit Euler, the values of z_k and $\dot{z}_k$ are not known. Once the velocity $\dot{x}_k$ has been computed through the Regula Falsi method, it is trivial to obtain the other quantities:

$$x_k = x_{k-1} + \Delta t\, \dot{x}_k$$

$$\dot{z}_k = \left(\dot{x}_k - \frac{\sigma_0\, |\dot{x}_k|\ z_{k-1}}{F_c + (F_s - F_c) \exp\left(- \left(\frac{|\dot{x}_k|}{v_s} \right)^{\delta} \right)} \right) \cdot \left(\frac{F_c + (F_s - F_c) \exp\left(- \left(\frac{|\dot{x}_k|}{v_s} \right)^{\delta} \right)}{1 + \Delta t\, \sigma_0\, |\dot{x}_k|} \right)$$

$$z_k = z_{k-1} + \Delta t\, \dot{z}_k$$

Leuven

A modified version of the LuGre method is the Leuven model, where the friction force is obtained by:

$$F_f = F_h(z) + \sigma_1 \frac{dz}{dt} + \sigma_2 v$$

With:

$$F_h(z) = F_b + F_d(z)$$

$$\frac{dz}{dt} = v \left(1 - sign\left(\frac{F_d(z)}{s(v) - F_b}\right) \left|\frac{F_{d(z)}}{s(v) - F_b}\right|^n \right)$$

The term $F_h(z)$ is introduced to take in account the hysteresis effects and substitutes the first term of the LuGre equation. This term is different from zero only when the velocity is null. It consists in an expression function of the bristle deformation *z*. Its value at the initiation of a transition curve (such as during a velocity reversal) is denoted as F_b. The transition curve that becomes active at a specific moment is symbolized as $F_d(z)$. $F_d(z)$ constitutes a symmetrical point-wise function of z that consistently increases. The implementation of $F_h(z)$, necessitates the utilization of two memory stacks: one to store the ascending-ordered minima of F_h (referred to as stack min), and another to house the descending-ordered maxima of F_h (referred to as stack max). These stacks expand during velocity reversals and contract when internal loops are closed. The computation of F_b, $F_d(z)$, and z adheres to the subsequent set of regulations [17] :

- During a velocity reversal, the initiation of a new transition curve occurs. The state variable z and $F_d(z)$ are both reset, while the preceding value of $F_h(z)$ is recorded in a memory stack called (f_m and f_M) while the corresponding value of z is memorized in the memory stacks called z_m and z_M. The recorded value of $F_h(z)$ then assumes the role of the new F_b.
- Performing the closure of an internal loop, referred to as "wiping out," involves removing the most recent values from all the stacks (z_m, z_M, f_m, f_M) associated with this internal loop. For positive/negative velocity, the last value on the stack f_M (or f_m) becomes the updated F_b. Recalculations are carried out for the values of z and $F_d(z)$ in a manner that enables the initiation of a new transition curve using the newly determined F_b value [18].
- Once the velocity is different from zero and the sliding regime occurs, all the parameters are reset.

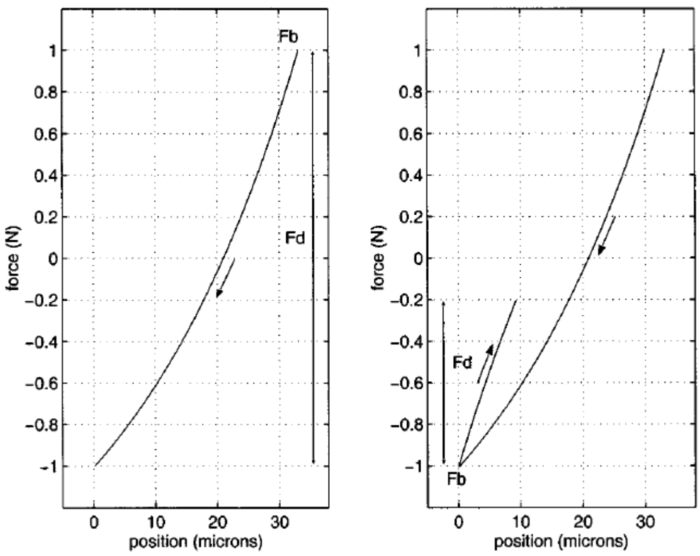

Figure 2.7 Representation of the behavior of F_h, F_b and F_c at velocity reversal [17]

In our purposes, two modifications were made to simplify its implementation:

- To overcome the discontinuity in the friction force, the argument of the nonlinear state equation $\frac{F_d(z)}{s(v)-F_b(z)}$ is changed to $\frac{F_h(z)}{s(v)}$ [18].With this argument, the new nonlinear state equation becomes:

$$\frac{dz}{dt} = v\left(1 - sign\left(\frac{F_h(z)}{s(v)}\right)\left|\frac{F_{h(z)}}{s(v)}\right|^n\right)$$

- The initial curve or virgin curve is computed in a similar way respect to [19] where the expression of this curve by:

$$f(x) = k_1 x - f_1\left(\exp(-f_2 \cdot x) - 1\right)$$

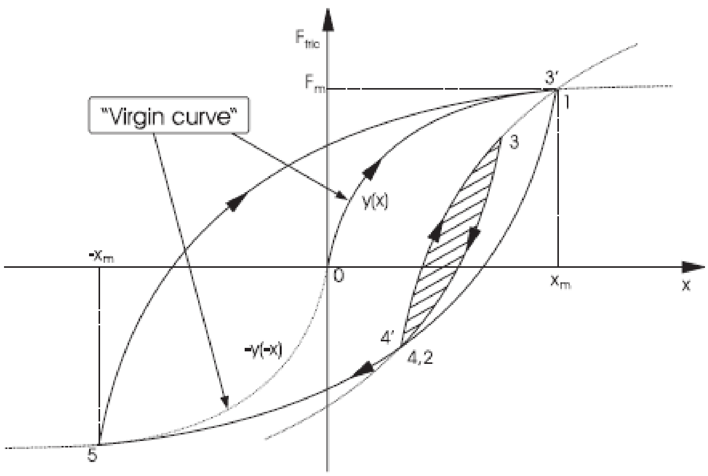

Figure 2.8 The virgin curve [19].

This formula represents the stress-strain curve due to the asperity deformation. It is possible to define an elastic and plastic domain. After the rupture, motion happens.

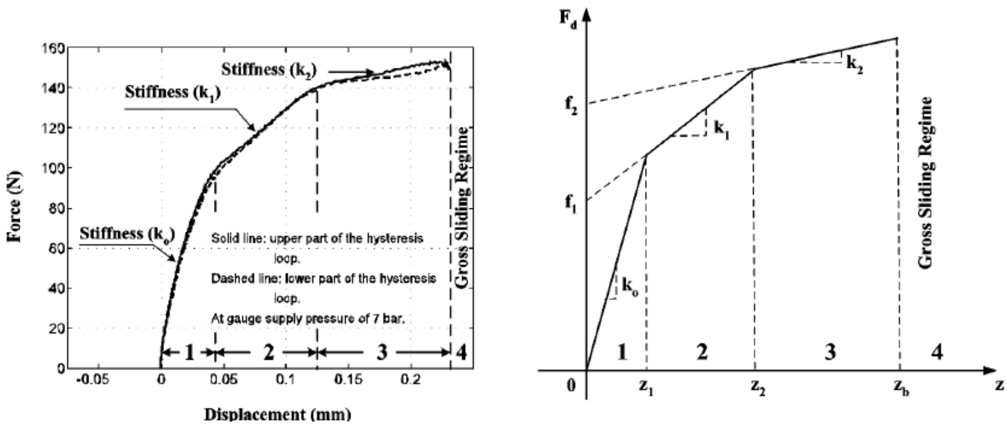

Figure 2.9 Virgini curve parameters [15].

The parameters k_1, f_1 and f_2 depends case by case on the different type of materials in contact. In our study they have been found with a Matlab fitting curve toolbox.

It is possible to schematize the behavior of the hysteresis at zero velocity in the following way:

$$
\dot{z}(i) = 0 \begin{cases}
\begin{array}{c}\text{Maximum}\\ z(i-1) > z(i)\end{array} \begin{cases}
\begin{array}{c}\text{Absolute maximum}\\ z(i) > max(z_M)\end{array} \begin{cases} z_M = [z(i)] \\ z_m = [-z(i)] \\ f_M = [F_h(i)] \\ f_m = [-F_h(i)] \end{cases} \\
\begin{array}{c}\text{Relative maximum}\\ z(i) \le max(z_M)\end{array} \begin{cases}
z(i) > z_M(\text{end}) \begin{cases} z_M = z_M(\text{end-1}) \\ z_m = z_m(\text{end-1}) \\ f_M = f_M(\text{end-1}) \\ f_m = f_m(\text{end-1}) \end{cases} \\
z(i) = z_M(\text{end}) \\
z(i) < z_M(\text{end}) \begin{cases} z_M = [z_M \;\; z(i)] \\ f_M = [f_M \;\; F_h(i)] \end{cases}
\end{cases}
\end{cases} \\
\begin{array}{c}\text{Minimum}\\ z(i-1) < z(i)\end{array} \begin{cases}
\begin{array}{c}\text{Absolute minimum}\\ z(i) < min(z_m)\end{array} \begin{cases} z_M = [-z(i)] \\ z_m = [z(i)] \\ f_M = [-F_h(i)] \\ f_m = [F_h(i)] \end{cases} \\
\begin{array}{c}\text{Relative minimum}\\ z(i) \ge min(z_m)\end{array} \begin{cases}
z(i) < z_m(\text{end}) \begin{cases} z_M = z_M(\text{end-1}) \\ z_m = z_m(\text{end-1}) \\ f_M = f_M(\text{end-1}) \\ f_m = f_m(\text{end-1}) \end{cases} \\
z(i) = z_m(\text{end}) \\
z(i) > z_m(\text{end}) \begin{cases} z_m = [z_m \;\; z(i)] \\ f_m = [f_m \;\; F_h(i)] \end{cases}
\end{cases}
\end{cases}
\end{cases}
$$

$$
\dot{z}(i) > 0 \begin{cases}
\begin{array}{c} z(i) > max(z_M) \\ \text{Virgin curve}\end{array} \quad F_h(i) = k_1 z(i) - f_1\left(e^{-f_1 z(i)} - 1\right) \\
\begin{array}{c} z(i) \le max(z_M) \\ \text{Internal loop}\end{array} \begin{cases}
z(i) > z_M(end) \begin{cases} z_M = z_M(1{:}\,\text{end}-1) \\ f_M = f_M(1{:}\,\text{end}-1) \\ z_m = z_m(1{:}\,\text{end}-1) \\ f_m = f_m(1{:}\,\text{end}-1) \end{cases} \\
z(i) \le z_M(end)
\end{cases}
\end{cases}
\begin{cases} f_b = f_m \\ z_s = \left(\dfrac{z(i) - z_m}{2}\right) \\ F_h(i) = F_b + 2\left[k_1 z_s - f_1\left(e^{-f_1 z_s} - 1\right)\right] \end{cases}
$$

$$
\dot{z}(i) < 0 \begin{cases}
\begin{array}{c} z(i) < min(z_M) \\ \text{Virgin curve}\end{array} \quad F_h(i) = -\left[-k_1 z(i) - f_1\left(e^{f_1 z(i)} - 1\right)\right] \\
\begin{array}{c} z(i) \ge min(z_M) \\ \text{Internal loop}\end{array} \begin{cases}
z(i) < z_m(end) \begin{cases} z_M = z_M(1{:}\,\text{end}-1) \\ f_M = f_M(1{:}\,\text{end}-1) \\ z_m = z_m(1{:}\,\text{end}-1) \\ f_m = f_m(1{:}\,\text{end}-1) \end{cases} \\
z(i) \ge z_m(end)
\end{cases}
\end{cases}
\begin{cases} F_b = f_M \\ z_s = \left(\dfrac{z_M - z(i)}{2}\right) \\ F_h(i) = F_b - 2\left[k_1 z_s - f_1\left(e^{-f_1 z_s} - 1\right)\right] \end{cases}
$$

- If $\dot{z} = 0$ it means that this is a velocity reversal point. A velocity reversal can correspond to a minimum or a maximum and each of them can be absolute or relative. If they are absolute, the point finds out of the two extremes, and it coincides with a point on the virgin curve. In this case all the values in all the stacks are deleted and replaced with the value in that point: z_M is replaced with the value of z_i at the reversal, z_m is replaced with the negative value of z_i, f_M is substitutes with the value of the function in z_i and f_m is replaced by the negative value of the function in z_i. In the case of relative maximum or minimum, it means that z_i is in between the two extremes and the point fall into an internal loop. In the case of relative maximum but z_i larger than the last recorded value of z_M, the previous internal loop is closed and all the last values of all the stack must be removed. If z_i is less than the last value recorded in z_M a new internal loop begins and all the stacks are updated with this new value. Instead in the case of relative minimum and z_i less than the last value of z_m, the last internal loop is closed and all the last values of all the stack are eliminated. If z_i is greater than the last value of z_m a new internal loop initiates and all the stacks are revised with the new values.

- If $\dot{z} > 0$ there will be a motion through the right side of the hysteresis curve and the point on the hysteresis curve can be on part of the virgin curve or can be part of an internal loop.
  If the z_i value is greater than the maximum value of the values included in the stack, that means the z_i is on the virgin curve and its value follows the equation for the stress strain curve or the equation given by:

  $$F_h(z) = f(x)$$

  $$f(x) = y(x)$$

  Where:

  $$f(x) = k_1 x - f_1\,(\exp(-f_2 \cdot x) - 1)$$

  On the other side, if z_i is less than the maximum value of the stack, it is part of an internal loop. If z_i is greater than the last value recorded on the stack of the maximum points z_M it means that a new internal loop is going to create and the previous internal loop is closed: the last values recorded on the all stacks (stack of maximum z_M, stack of minimum z_m, stack corresponding to the values of *f(z)* computed in the maximum f_M and stack corresponding to the values of *f(z)* calculated in the minimum f_m) must be deleted. If z_i is less than the last value of the stack of the maximum points, the internal loop is not closed. In both cases, the value of the friction force is given by the formula from the formula:

  $$F_h(z) = f(x)$$

  $$f(x) = -y(-x)$$

- If $\dot{z} < 0$ there will be a motion through the left side of the hysteresis curve and the point on the hysteresis curve can be on part of the virgin curve or can be part of an internal loop.

If the z_i displacement is less than the minimum value of the stack of z_m that means z_i is outside of the minimum extreme and the value of F_h follows the equation of the virgin curve. If z_i is greater than the minimum value recorded in the stack of the minimum values z_m , z_i is in an internal loop. In the case z_i less than the last value recorded in the stack of minimum values z_m, the last internal loop is closed and all the last values from all the stacks must be deleted. If z_i is equal or greater than the last recorded value of z_m the internal loop is still running. In both cases the function describing F_h follows the equation:

$$F_h(z) = f(x)$$

$$f(x) = -y(-x)$$

2.5 Test bench description

This chapter describes the test bench utilized in the thesis. It consists of enumerating its diverse components and presenting key details regarding its construction and operational features. Before proceeding with the description of the components, it's important to explain the functioning of the bench. A proportional flow control valve receives an input voltage signal that determines the displacement of the spool, consequently regulating the compressed air flow that powers the circuit and actuates the cylinder. The end of the stem is then attached to a carriage that moves along a linear guide with recirculating ball bearings, reducing friction's impact. The experimentation involves controlling the valve using different signals and comparing the level of accuracy between experimental data collected from sensors and the numerical values calculated by the implemented model. In this study will be analyze two types of signals for this specific test bench: a sinusoidal signal and one step signal that try to simulate the stick and slip phenomena.

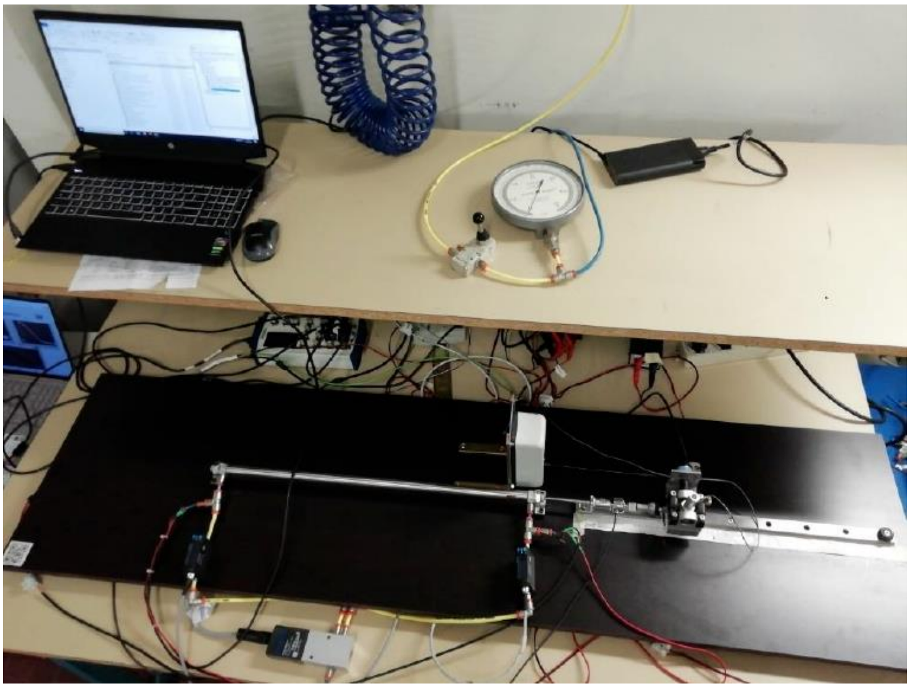

Figure 2.10 Test bench in [20].

The experimental setup includes a 5/3-way flow proportional valve (FESTO, MPYE-5-M5-010-B) and a pneumatic cylinder (Camozzi, 24N2A16A500) used for controlling the position of a cart weighing 0.75 kg. The cart is guided by a recirculating ball bearing guide (Misumi, SEBL 20-510). The pneumatic cylinder features a 500 mm stroke, a 16 mm bore diameter, and a 6 mm rod. Flow rates through the valve ports were measured using two bidirectional hot wire flowmeters (FESTO, SFAH-200B-Q65-PNLK-PNVBA-M8). Pressure readings within the cylinder chambers were obtained using two pressure sensors (Honeywell, 40PC-150G). The force applied to the cart during actuation was quantified using a load cell (HBM, U9C 200N) positioned between the cylinder rod and the cart. The position and velocity of the cart were continuously monitored using a wire linear position transducer (Celesco, DV301-0040-111-1110). Cart acceleration was measured with an accelerometer (Brüel & Kjær 4507 B 004), securely attached using cyanoacrylate-based adhesive. To control the system, a computer provided the driving voltage signal to the valve via a D/A converter. Data from the various sensors and transducers were visualized and recorded using a data acquisition system (USB-6212 BNC Bus-Powered M Series, 16 AI, 16-bit, 400 kS/s). It's essential to note that, in these experiments, the pneumatic positioning system was tested without the use of a closed-loop control system. Figure 2.11a schematize the test set-up. In Figure 2.11b, the test bench configuration has been modified to perform friction identification test. The 5/3-ways proportional flow valve was removed and a Camozzi ER238-90AP pressure regulator was used to supply air to one of the cylinder chambers, whereas the other one was kept plugged.

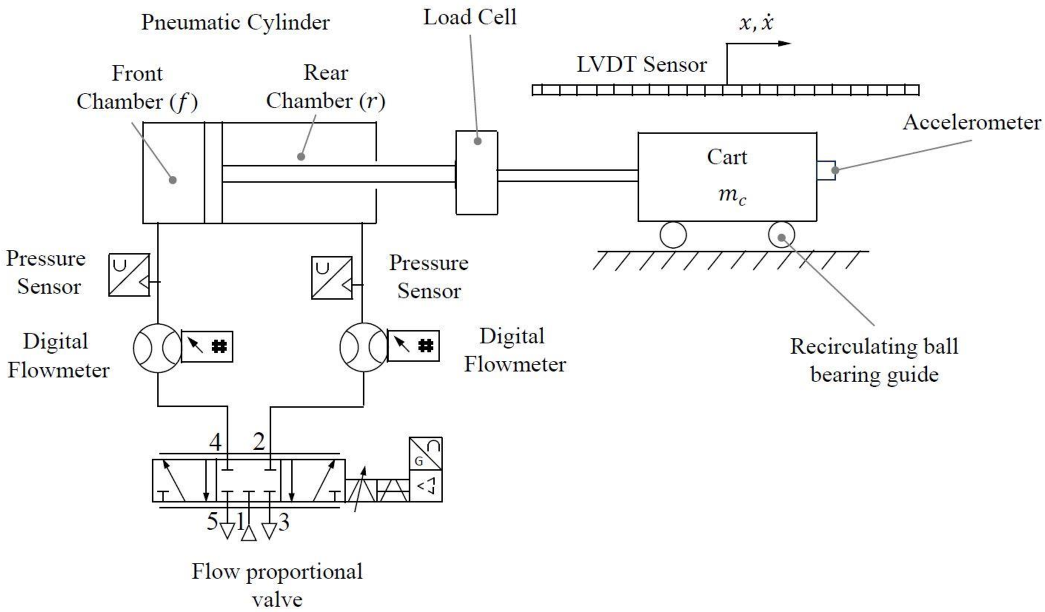

Figure 2.11a Schematization of the test bench [20].

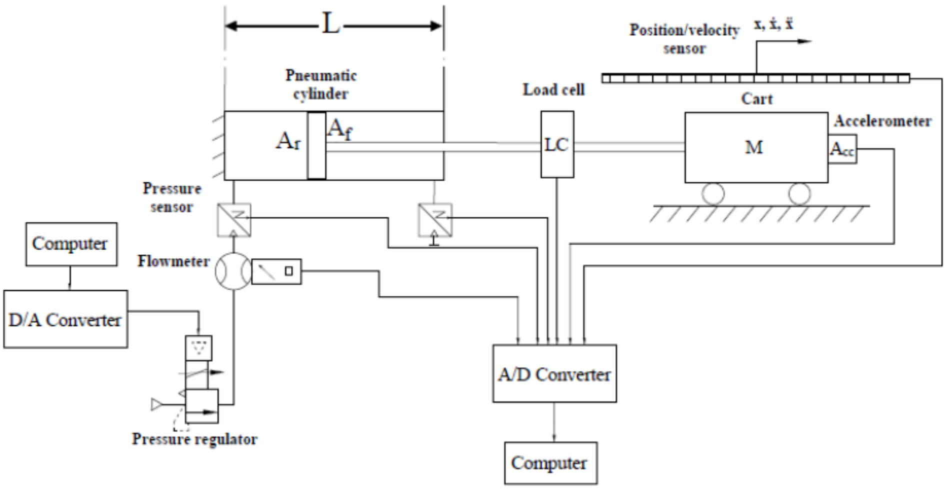

Figure 2.11b Modification of the test bench [20].

While the forces acting on the carriage can be represented as:

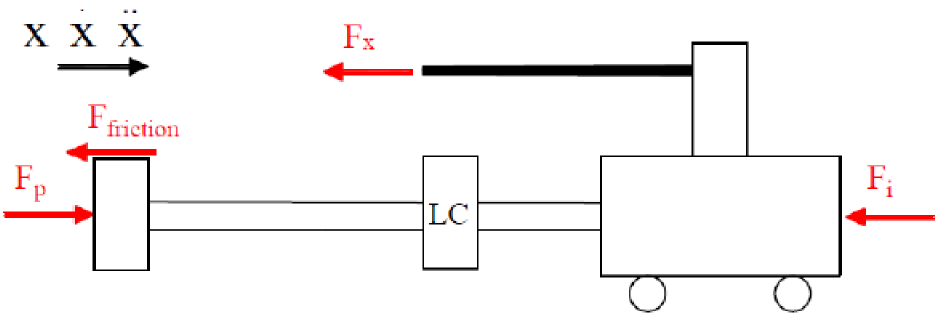

Figure 2.12 Schematization of the forces acting on the cart [20].

The forces here sketched are: $F_{friction}$ the friction force, F_i the inertia force, F_p the driven force and F_x the force due to the presence of the LVDT sensor. The sum of the friction force between the seal of the piston-rod contacts and the frontal seal on the exit hole of the piston constitutes the total $F_{friction}$. The friction due to the carriage is neglected because it is very poor.

The carriage consists of a recirculating ball prism guide provided by Misumi, with product code SEBL 20-510. The movable part includes a plate for potential accommodation of a inverted pendulum, while the fixed part of the guide has been attached to a wooden platform serving as the foundation for installing all the components making up the bench. The pneumatic cylinder is connected to the carriage via a spherical joint supplied by Camozzi (GY-12-16).

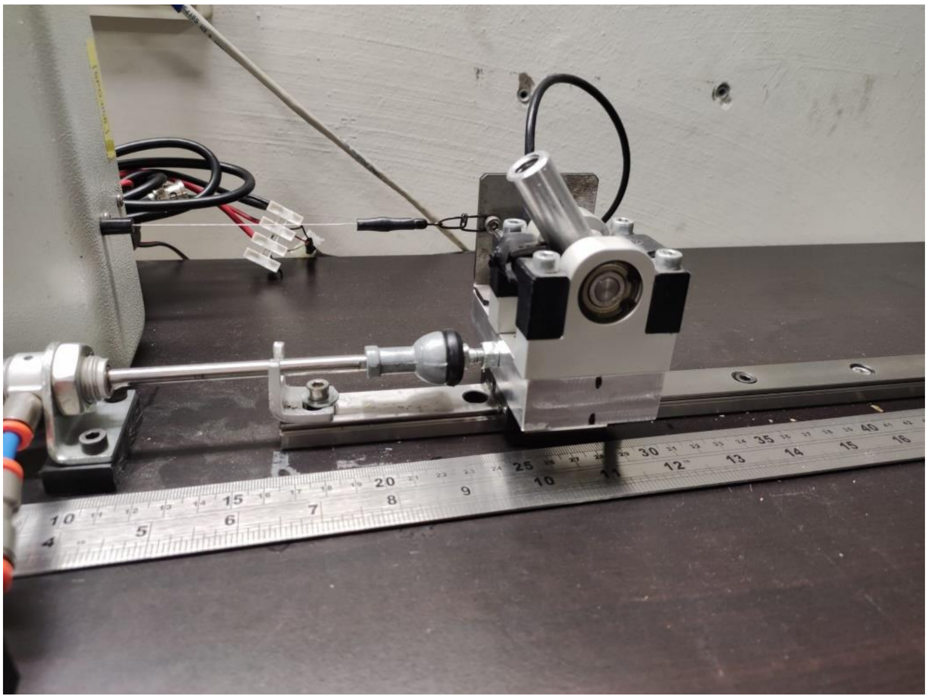

Figure 2.13 The cart used in the test.

The pneumatic cylinder utilized is manufactured by Camozzi, with product code 24N2A16A500.

Figure 2.14 The double acting cylinder [20].

The cylinder characteristics are listed below:

Stroke	500 mm
Bore	16 mm
Rod diameter	6 mm
Operating temperature	1\10 bar
Speed	10\100 mm/s
Fluid	Filtered air 7.8.4
Joint	M5

The flow valve is a closed-center 5/3 proportional valve manufactured by Festo: model MPYE-5-M5-010-B.

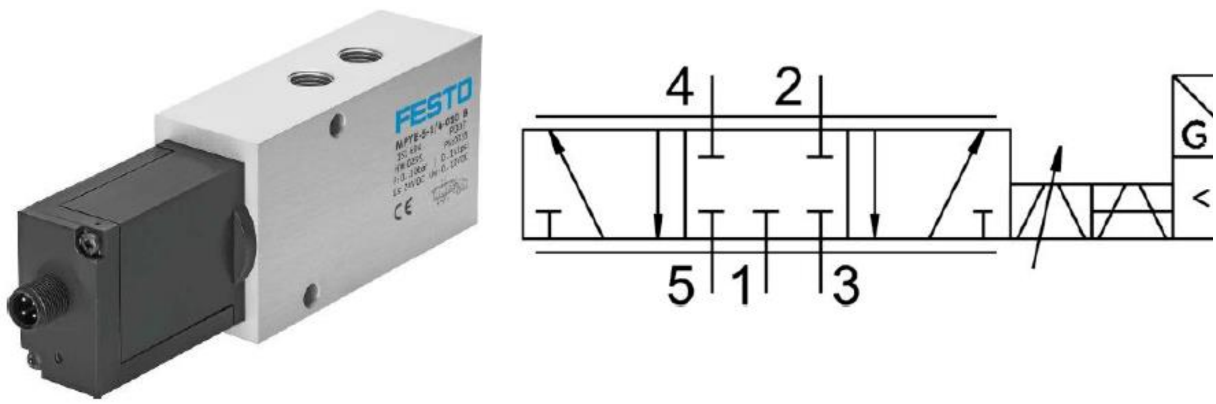

Figure 2.15 The pneumatic valve [20].

The valve characteristics are:

Operating pressure	0\10 bar
Standard nominal flow rate	100 l/min
Max frequency	115 Hz

Max hysteresis	0,4 %
Operating voltage	17\30 V
Nominal values	0\10 V
Fluid	Filtered air
Fluid temperature	5\40 °C
Pneumatics joint	M5

The electronic pressure regulator is manufactured by Camozzi, with product code ER238-90AP, and it has been used to modulate the output pressure of the component according to a known law.

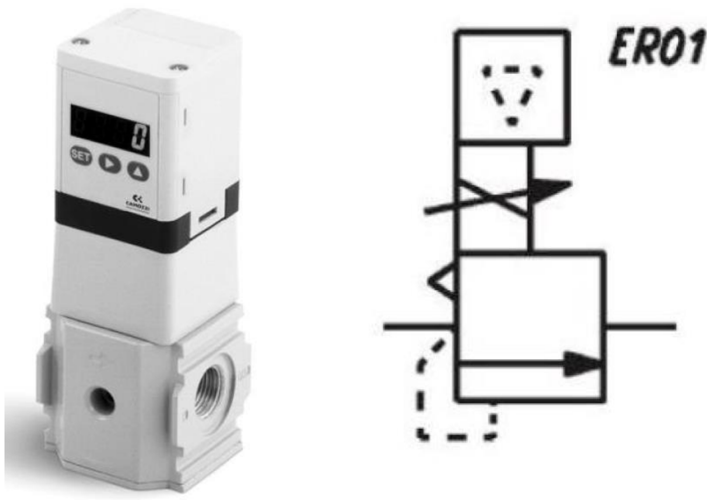

Figure 2.16 The pressure regulator [20].

Operating pressure range	0,5\9 bar
ANR flow rate	1500 Nl/min
Inlet Pressure	10 bar
Input Signal	0\10 V
Output Signal	0\5 V
Voltage supply	DC 24 V
Operating temperature	5\50 °C
Degree of protection	IP 40

A manual valve, manufactured by Metal Work, product code 7010001300, was used in series with another manual valve (Metal Work 7010000200) to pressurize a tank during required tests. By establishing this connection, it became feasible to control the pressure inside the tank using a second supply line.

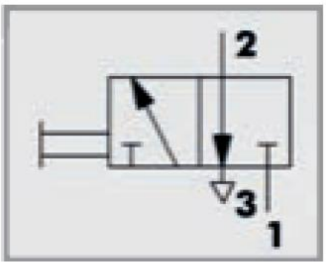

Figure 2.17 The manual valve 3/2 [20].

Operating range	-0,99\10 bar
ANR flow rate	1500 Nl/min
Inlet Pressure	10 bar
Input signal	0\10 V
Output signal	0\5 V
Voltage supply	DC 24 V
Operating temperature	5\50 °C
Degree of protection	IP 40

The series of valves is completed by a manual valve that is manufactured by Metal Work, product code 7010000200. It's a 3/2 manual control valve, and its main characteristics are outlined below.

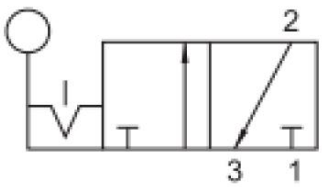

Figure 2.18 The manual valve 3/2 [20].

Operating range	-0,99\10 bar
ANR flow rate	550 Nl\min
Pipe diameter	1/8”
Operating temperature	-10/60 °C
Weight	164,28 g

Material	Aluminum

On the other hand, the flow rate sensors utilized are manufactured by FESTO with reference code SFAH-200B-Q65-PNLK-PNVBA-M8. These are bidirectional flow meters utilizing a thermal phenomenon, as the measurement is conducted through a micromechanical sensor element connected to an electronic control unit downstream. This unit monitors the heat transfer in relation to the flow passing through the sensor.

Figure 2.19 The flow rate sensor [20].

Operating range	-0,9\10 bar
Max measurable flow rate	200 l/min
Accuracy	± (2% of the measured value + 1%FS)
Analogic Output	0-10 V 4-20 mA 1-5 V
Operating voltage range	22\26 V
Max output current	100 mA
Fluid	Filtered air
Fluid temperature	0\50 °C
Nominal temperature	23 °C

The bench is equipped with two Honeywell pressure transducers, model 40PC-150G, to detect the pressures in the two chambers of the pneumatic cylinder.

Figure 2.20 The pressure transducer [20].

Measurement range	0\150 psi
Max pressure	300 psi
Supply tension	5 V
Max supply current	10 mA
Max output current	0.5 mA
Operating temperature	-45\125 °C
Hysteresis and repeatability	0,15 %
Output voltage	0,5\4 V
Sensibility	26,6 mV/psi

The carriage movement is detected through a non-extendable wire transducer, model DV301-0040-111-1110, from the company Celesco. This device is a combination of a hybrid trace potentiometric position transducer and a tachometric device that outputs an electrical signal proportional to the velocity of the body to which the wire end is attached. A wire transducer has the drawback of the return force required to retract the wire inside itself; in some applications, this action might not be tolerable as it can be comparable to the forces acting on the object being position-monitored.

Figure 2.21 The LVDT sensor [20].

Measure range	0\101,6 cm
Accuracy	0,1 % FS
Repeatability	± 0,02 % FS
Max supply voltage	30 V
Output voltage speed	65 mV/m/min
Output resistance	500 Ω
Operating temperature range	-40/90 °C

To enhance data accuracy during acquisition, the decision was made to install a Brüel & Kjær model 4507 B 004 accelerometer on the trolley. This device comes with various benefits, including the ability to connect directly to the power network, the option to use cost-effective long connecting cables, and a significantly extended bandwidth. The employed accelerometer is denoted by the manufacturer as CCLD, signifying its operation through direct connection to the power network, thereby generating a voltage-modulated output signal in alignment with the power network.

Figure 2.22 The accelerometer [20].

Weight	4,6 g
Sensibility	10 ± 5% mV/s^{-2}
Bandwidth	6 kHz
Voltage supply	24\30 V
Current	2\20 mA
Output resistance	30 Ω
Operating temperature	-54\121 °C

In order to measure the driven force a load cell was mounted between the top of the cylinder rod and the spherical joint to measure the intensity of both tensile and compressive forces transmitted by the pneumatic actuation. Specifically, the model used is the U9C 200N, manufactured by HBM. The measuring element is a deformable steel diaphragm on which strain gauges (SG) are installed. These strain gauges are positioned so that the applied force causes two of them to stretch under tension and two to compress. The strain gauges are interconnected to form a Wheatstone bridge with a four-wire configuration. They change their ohmic resistance proportionally to their length variation, thus unbalancing the Wheatstone bridge. When the bridge is supplied with an excitation voltage, the circuit produces an output signal proportional to the resistance variation and, consequently, to the introduced force. The arrangement of the strain gauges is chosen in a way that significantly compensates for parasitic forces and moments (such as lateral forces and the influence of eccentricity), as well as temperature effects. The utilized transducer emits a signal in mV/V, and for signal processing, a measuring amplifier is required. The main technical data of the U9C force transducer are summarized in the table.

Figure 2.23 The load cell [20].

Accuracy class	0,2
Relative hysteresis	<0,2% $v_{0,5}$
Nonlinearity error	<0,2% d_{lin}
Nominal sensibility	1 mV/V
Voltage supply	0,5\12 V
Operating temperature	-30\85 °C
Max force	200 N
Rupture force	>400 N
Max torque	2,5\3,7 Nm
Resonance frequency	12, kHz

The amplifier utilized is the HBM Clip AE101, designed to amplify measurement signals originating from the load cell. The technical specifications are detailed in the provided table.

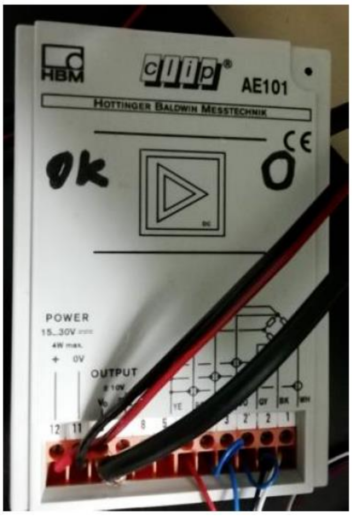

Figure 2.24 The signal amplifier [20].

Accuracy class	0,1
Bridge supply voltage	2,5 V, 5 V, 10 V
Measurement range	0,1\2 mV/V 0,2\4 mV/V 0,4\8 mV/V
Nonlinearity error	<0,05% FS
Output voltage	± 10 V
Load resistance	≥ 4 k Ω
Internal resistance	< 2 Ω
Operating temperature	-20\60 °C
Temperature influence	< 0,1 % FS
CC supply voltage	15\30 V
Protection grade	IP10

To acquire the data, the National Instruments USB-6212 multifunction I/O device was employed. The key characteristics of this device are presented in the following table.

	Supply	5 V
	Number of channels	8
	ADC resolution	16 bit
Analogic input	Acquisition frequency	400 kS/s
	Timing resolution	50 ns
	Bandwidth	1,5 MHz
	Number of channels	2
	DAC resolution	16 bit
Analogic output	Max frequency	250 kS/s
	Timing resolution	50 ns

	Output range	± 10 V

CHAPTER 3

This chapter shows and describes the results of the performed experimental tests. Each test has been made for a different type of regime: pre-sliding, transition and gross sliding. Experimental test related to the pre-sliding regime highlighted the phenomenon of hysteresis with non-local memory. Transition regime tests exhibit the stick-slip phenomenon. Gross-sliding tests manifest the Stribeck effect is emphasized.

3.1 Pre-sliding regime test

Pre-sliding regime tests are necessary to identify the parameters related to bristle state equation. Since the execution of this test requires a force control actuator (that is not present in adopted experimental set-up, see Sec. 2.2), the considered experimental data was taken from the literature [15]. The mechatronic system under consideration in is a pneumatic servo positioning system. The testing arrangement comprises a 5/3-way proportional directional control valve and a rod-less pneumatic cylinder. To determine the driving force, two pressure sensors are employed to measure the pressure difference between the cylinder's chambers, which is directly proportional to the force being applied. The position sensor gauges the initial displacement before sliding begins. Acceleration is measured using an accelerometer. Velocity is then calculated by integrating the measured acceleration data. A computer equipped with a digital signal processor (DSP card) is utilized to transmit the control signal to the proportional valve via a D/A converter and to collect data from all sensors through A/D converters. The procedure for assessing friction involves measuring acceleration and subtracting the computed inertial forces from the applied forces, which are inferred from the pressure difference detected in the cylinder's chambers.

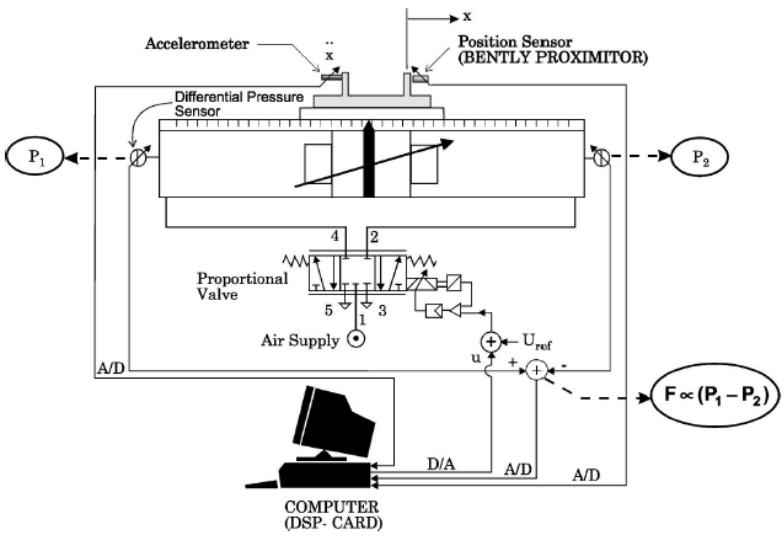

Figure 3.1 Experimental set-up in [15].

In this context, an input is given to the valve that let the air flow goes through one of the chambers imposing a difference in pressure and consequently a driving force. The piston is subjecting to a periodic motion featuring multiple velocity reversal per period within the pre-sliding regime. The force applied has not to be greater than the first detach force and the piston must not move. Despite the velocity of the piston is null, micro-displacements occur and, in this case, displacement itself can be considered equivalent to the asperities deformation: measuring the displacement means measure the deformation of the roughness. Friction is only function of the displacement and not depends on time or velocity. The experimental hysteresis curve is shown below:

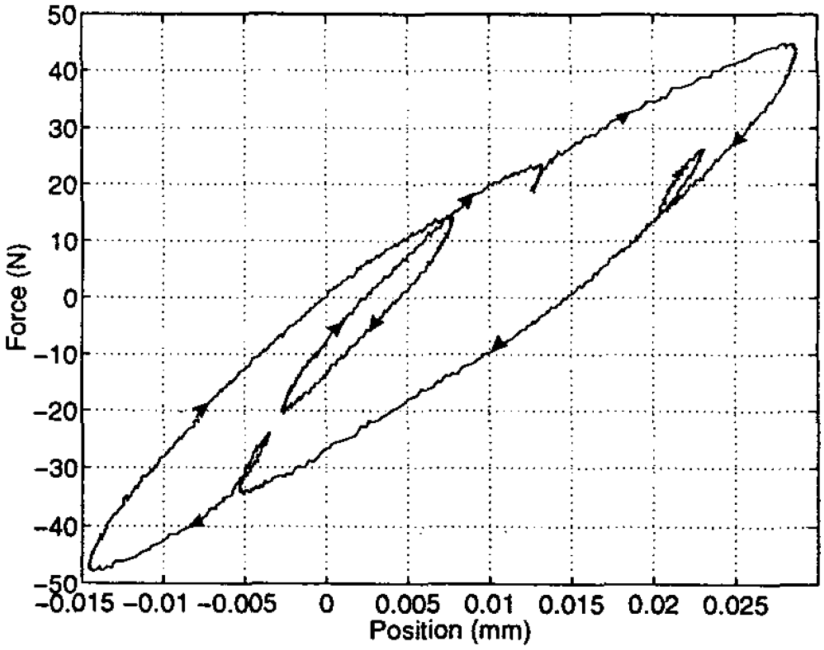

Figure 3.2 Experimental hysteresis curve found in [15].

The nonlocal memory aspect of pre-sliding hysteresis friction has been emphasized. At each velocity reversal a loop starts. If the module of the displacement at the reversal point is larger than the extremes recorded in the stacks, an external loop stars while if at the reversal, the displacement is smaller than these extremes, an internal loop take place. It is also possible to spot the virgin curve following the curve that start from zero of the coordinate planes and continues until the upper left reversal point.

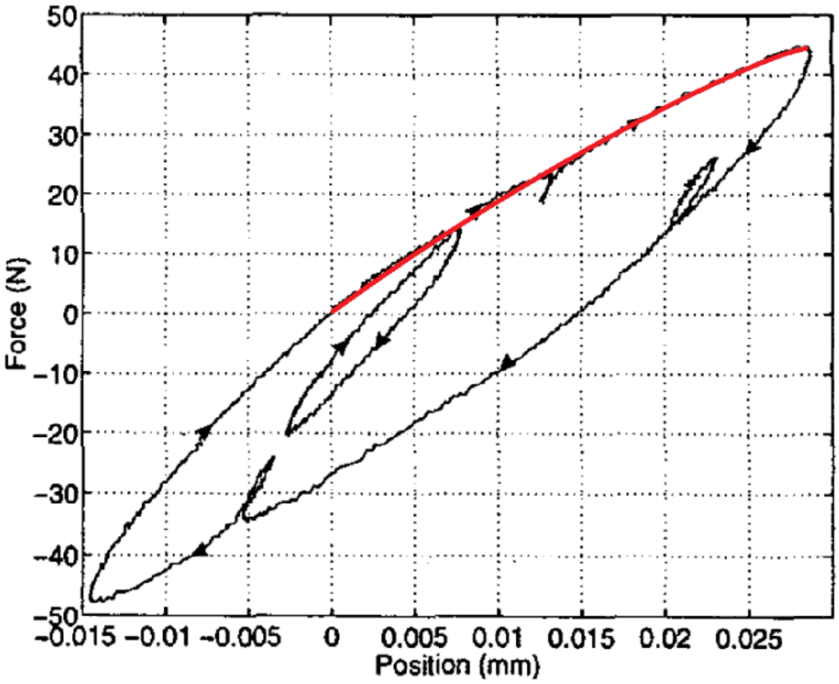

Figure 3.3 Experimental virgin curve in [15].

3.2 Transition regime test

The tests carried out for the transition regime are made on the test bench described in the Sec. 2.2. Transition tests are necessary to identify the stick-slip phenomenon. They require low velocity regime where the changeover between static and dynamic friction happens. They are performed at different supply pressure of the control valve pressure (starting from 1.5 bar up to 6 bar with 0.5 bar of step). At each supply pressure value, it is necessary to find out the lowest tension level at which the valve triggers the piston's motion. Four tests are considered based on their effectiveness. The various tests are listed below:

	Pressure [bar]	**Output piston tension [V]**	**Input piston tension [V]**
Test 1 (Stick_Slip_Ps40_Vi56_Vf49_3)	4.0	5.6	4.9
Test 2 (Stick_Slip_Ps60_Vi542_Vf5_1)	6.0	5.4	5.0
Test 3 (Stick_Slip_Ps50_Vi545_Vf48_2)	5.0	5.5	4.8
Test 4 (Stick_Slip_Ps15_Vi59_Vf5_1)	1.5	5.9	5.0

The valve is an electro valve in which the offset is set to 5V. This means that at 5V the corresponding position of the valve plug is exactly at the centre and the air doesn't flow inside the chambers. For voltage values (input piston tension) between 0 and 5 the left chamber is supplied and, on the opposite, for values between 5 and 10 (output piston tension), the right chamber is filled up. This means that if a value in between 0 and 5 is given to the electro valve, the piston will move on the left. The value of voltages highlighted in the previous table is the minimum voltage at which the piston breaks the "first detach force". It is possible to notice that in two test (test 2 and test 3), the voltage at which the valve would let the piston go back, is 5.0 V. At this value of tension, air would not flow through the valve and piston would remain still, but this does not happen, and the piston moves back in the initial position. This is caused by the LVDT rod that pull the cart even if there is not a driving force moving it. This LVDT sensor measures the displacement while velocity and acceleration are obtained deriving numerically the position. The friction force comes from the equilibrium of the forces by difference of the inertial term and the driving force. The driving force is computed knowing the pressure in the chambers (through the pressure gauge) and the areas of the two surfaces of the piston. This procedure is implemented for all the tests.

3.2.1 Overall Results

At the beginning of each test, the valve is in its rest position, i.e., there is no output or discharge flow from the valve (the driving voltage is approximately 5V). Subsequently, the driving voltage of the valve is set to the minimum constant value that guarantees the outstroke of the cylinder. In these instances, after a time interval that depends on the testing conditions (supply pressure and driving voltage of the valve) the cylinder moves generating the motion of the cart. In this way, it was possible to experience the presence of the stick-slip phenomenon. Similarly, to induce stick-slip during the instroke of the cylinder, once the cart reaches its end stroke, the input voltage is manually changed to the minimum and constant value that generates the instroke of the cylinder. During the stick-slip process, the cart displacement resembles a stepped trend in both directions. The velocity results reflect the displacement behaviour: when the piston stops its motion due to the stiction force, velocity is null. During motion, the velocity reports some peaks whose values depends on the supplied pressure. When air is introduced into the front chamber, it undergoes compression, resulting in an increase in pressure denoted as P_f, while the pressure in the rear chamber, P_r, decreases. Initially, the driving force due to the difference in pressure between the chambers, is not enough to overcome the static frictional force, causing the piston stiction. Once the pressure force exceeds the breakaway force, the piston initiates its movement. Nevertheless, as the piston advances, the volume of the front chamber expands, causing a reduction in pressure, and consequently stopping the piston motion. As the continuous supply of air into the front chamber and discharge from the rear chamber persists, the pressure in the front chamber, increases again, ultimately overcoming the breakaway force and generating the cart motion.

The friction force shows a trend as a saw tooth in which it ranges between peaks. The amplitude of this peaks changes both depending on the position of the piston during its motion and on the supplied pressure. Same as the semi-period: the period is not unique and depends on the same factors as the velocity and displacement. Each peak corresponds to the start of the motion for the piston. This value corresponds to the peaks and if the peaks value changes at each semi-period, it is impossible to find a unique for the first detach force. Initially, this value increases when the piston is close to the initial position while decreases and maintains almost constant when get closer to the end of the stroke. This probably due to a greater wear in a certain area of the piston stroke: the cylinder worked much more in those areas during his work life.

Moreover, it is possible to notice that when the supply pressure of the valve is increased, stick-slip is more evident. The seals adhere much more in high pressure conditions because they are pushed against the cylinder liner. These effects the first detach force: higher the pressure, higher the stiction force. It is possible to notice that in test 4, at 1.5 bar, stick-slip does not appear in the first half of the trial because of the too low pressure.

3.2.2 Test 1

Figure 3.4 shows the experimental test related to test 1. Figures 3.4a, 3.4b, 3.4c, 3.4d, 3.4e and 3.4f show the trend of the valve driving voltage, the displacement and velocity of the cart, the pressures and air flow of the cylinder chambers, and friction force recorded during the test 1.

It can be seen (see Figure 3.4a) that, after the application of a constant driving voltage of 5.35 V, the cylinder remains in its initial position (see Figure 3.4 b and 3.4c) and it moves only after a resting time of about 3.5 s. Here, the system is in presliding regime and there are only microscopic deformations of the surfaces asperities. Unfortunately, as said in Section 3.1, the position sensor integrated in the experimental set-up does not make it possible to asse the values of these micro-displacements. This was the time required to regulate the pressure in cylinder chambers till reaching the value of the breakaway force. During this first time interval (see Figure 3.4d and 3.4e), the pressure in the front chamber increases thanks to the constant inflow provided by the control valve. On the contrary, the pressure in the rear chamber decreases since it relates to the discharge port of the valve. Accordingly with these pressures trends, the computed friction force (from the equilibrium equation of the cart-piston-rod system) gradually increases till the breakaway value.

As the cylinder moves, it motion stops after few seconds (at about 5,65 s) and this kind of movement process continues till the cart reaches its end stroke position (at about 13 s). This is a characteristic behaviour of the stick-slip process observed in pneumatic cylinders. The occurrence of this phenomenon can be explained by considering the time evolution of the pressures in the cylinder chambers. When air is supplied to the front chamber, it is compressed and the pressure P_f increases (in Figure 3.4d), while the pressure P_r in the rear chamber decreases. In the first 3.5 s, the difference between $P_f A_f$ and $P_r A_r$ is not large enough to overcome the stiction friction force so that the piston remains stationary (stick). As the difference between $P_f A_f$ and $P_r A_r$ overcome a value of 73.72 N, then the piston starts moving (slip). However, as the piston moves, the volume of the front chamber expands and the pressure P_f decreases and thus the piston stops moving (stick). As air continues to be fed into the front chamber and discharged from the rear one, the pressure P_f is increased again and then overcomes the breakaway force generating the cart motion again. The process is then repeated.

It is worth noting that (see Figure 3.4e) that the value of the breakaway force varies during the test, but globally exhibit a periodic trend. Initially, the value of the breakaway force increases up to a maximum value, then gradually reduces to an almost constant value that manifests for some stick-slip steps. This periodic trend is evidenced both during the outstroke and instroke of the cylinder (see Figure 3.4 f).

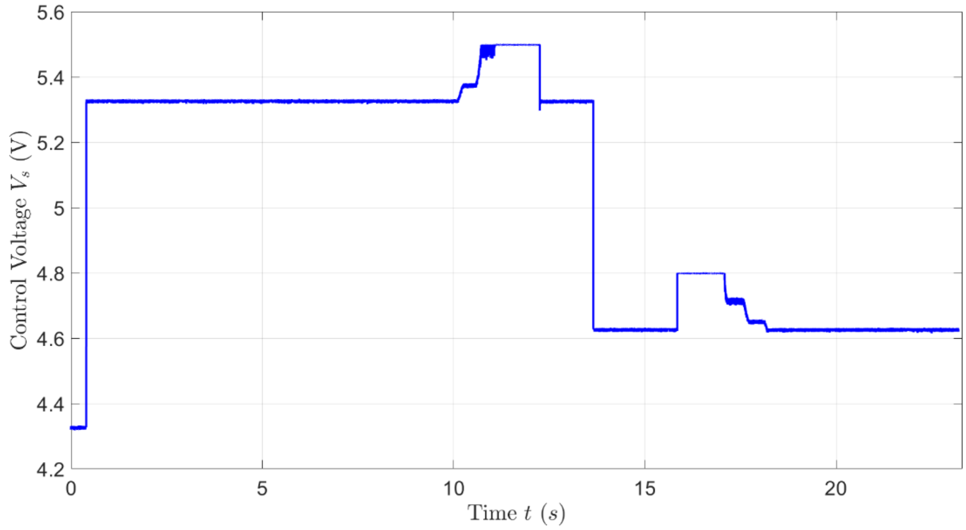

Figure 3.4a: Driving voltage.

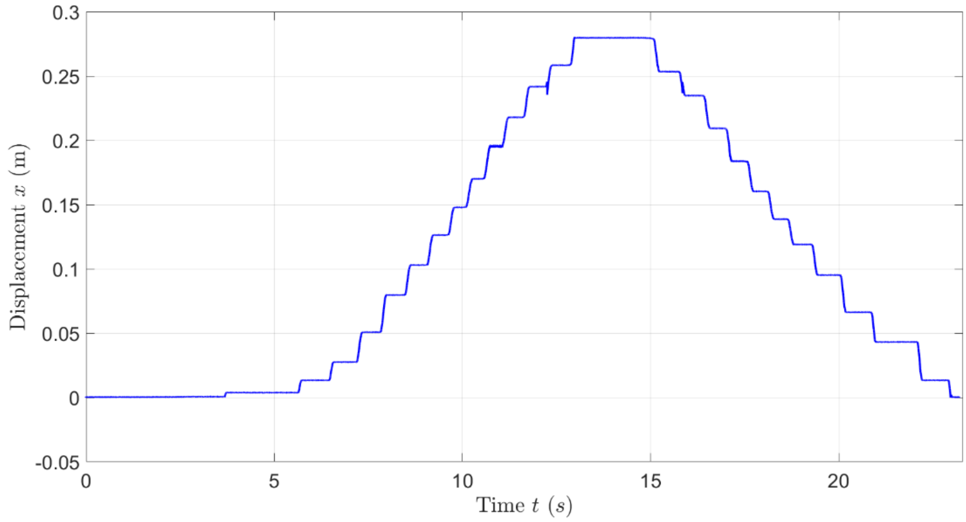

Figure 3.4b: Cart displacement.

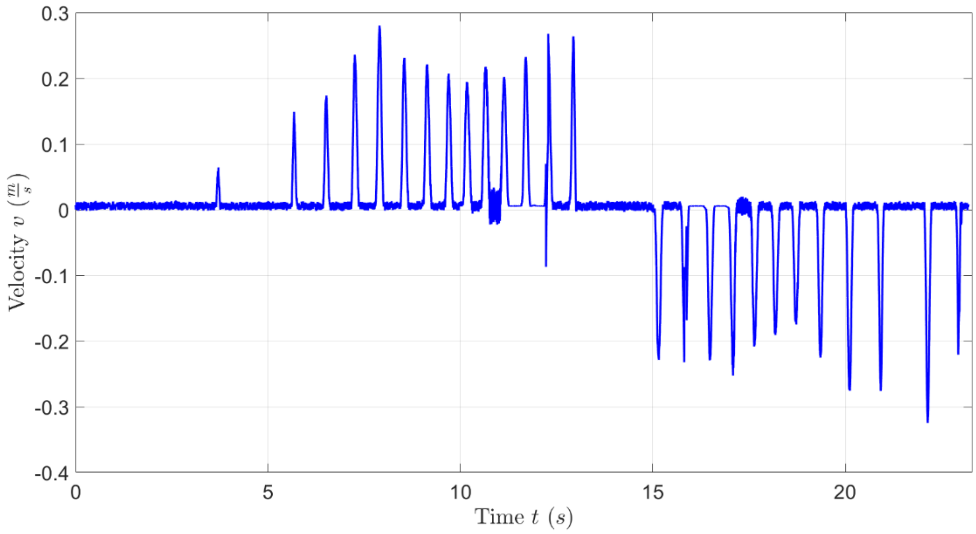

Figure 3.4c: Cart velocity.

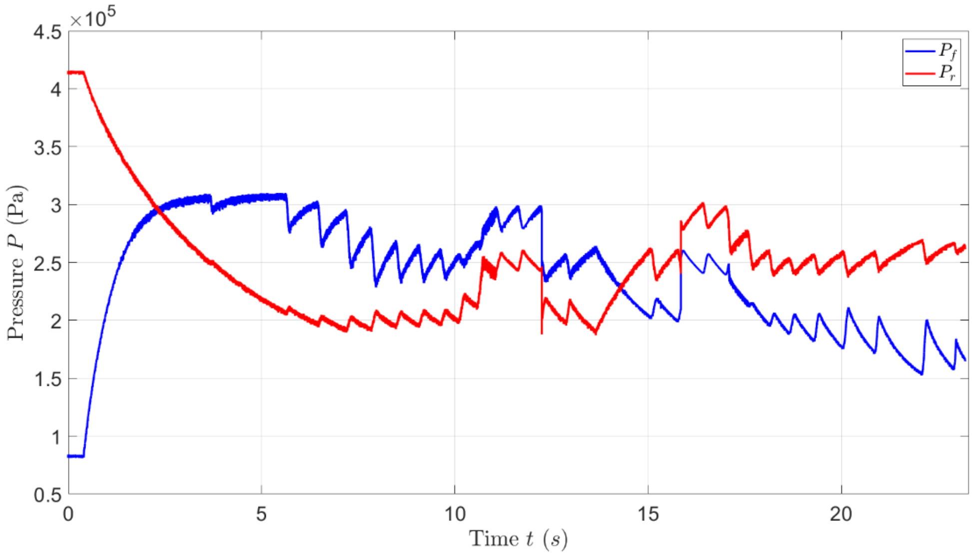

Figure 3.4d: Chamber pressures.

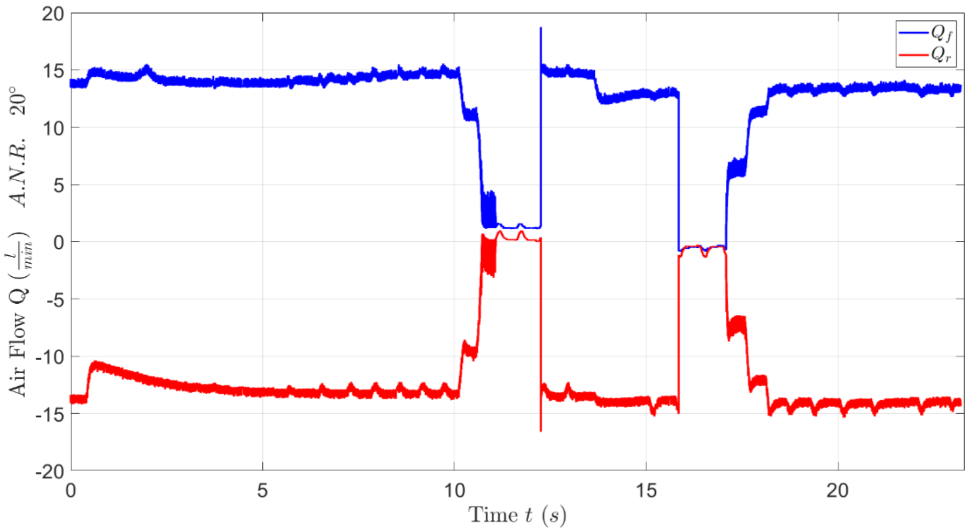

Figure 3.4e: Air flow.

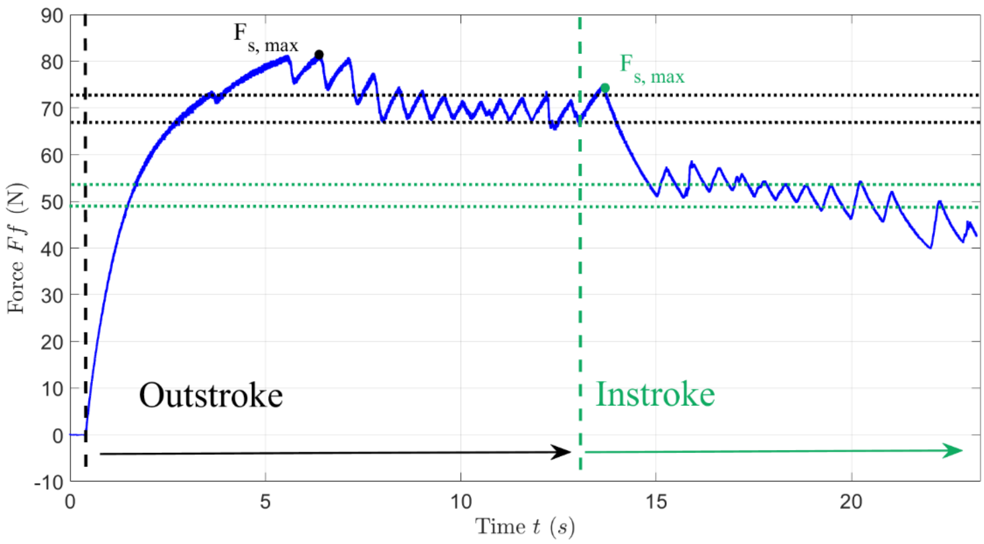

Figure 3.4f: Friction force.

3.2.3 Other Tests

Since the behaviour experienced in the other tests is quite like that of test 1, the other experimental results are reported without any additional comments.

Test 2

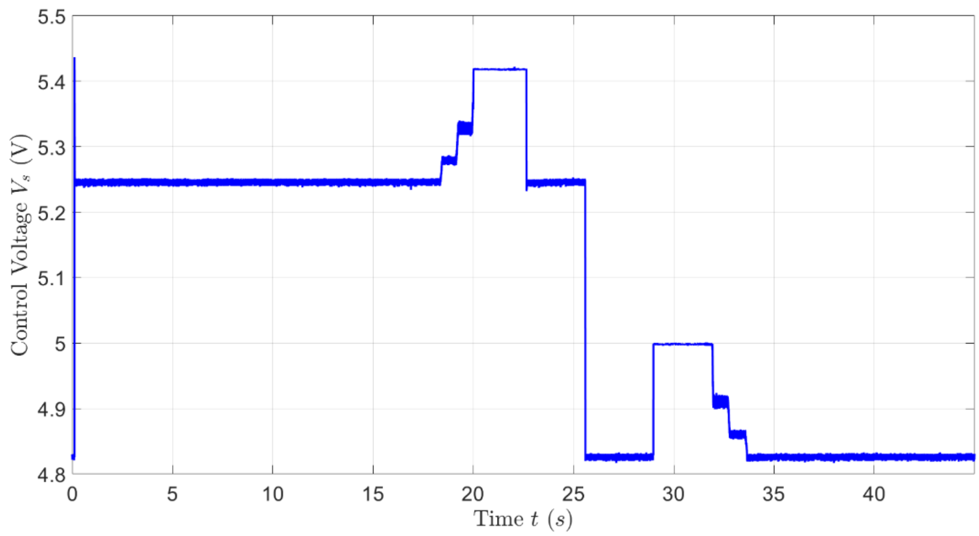

Figure 3.5a: Driving voltage.

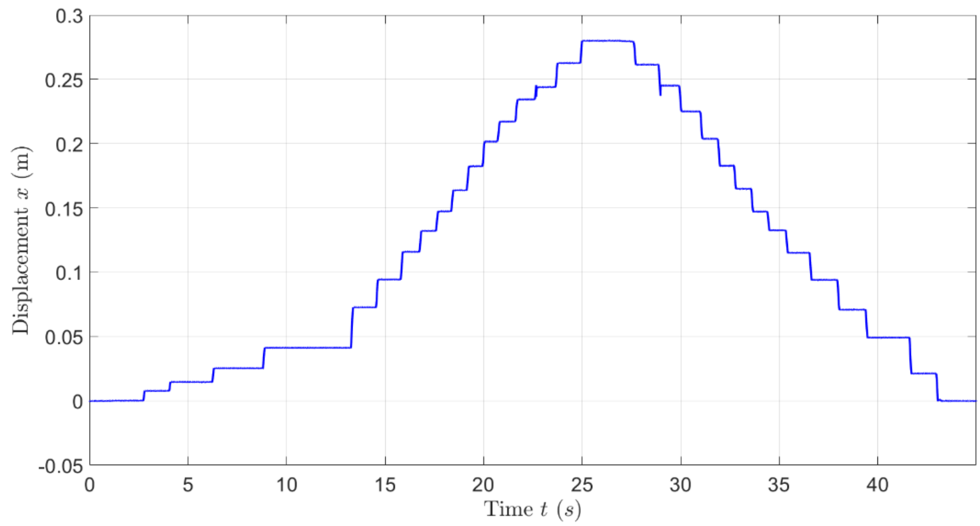

Figure 3.5b: Cart displacement.

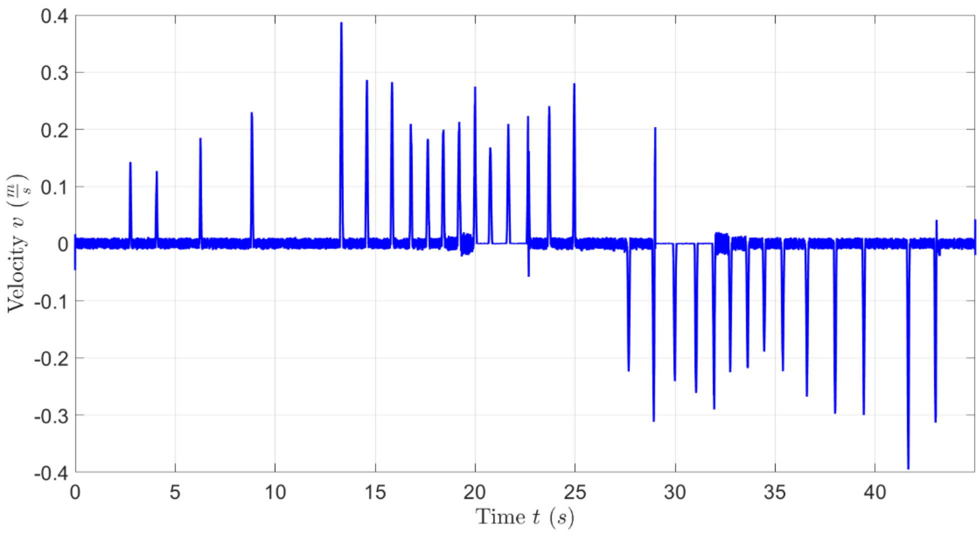

Figure 3.5c: Cart velocity.

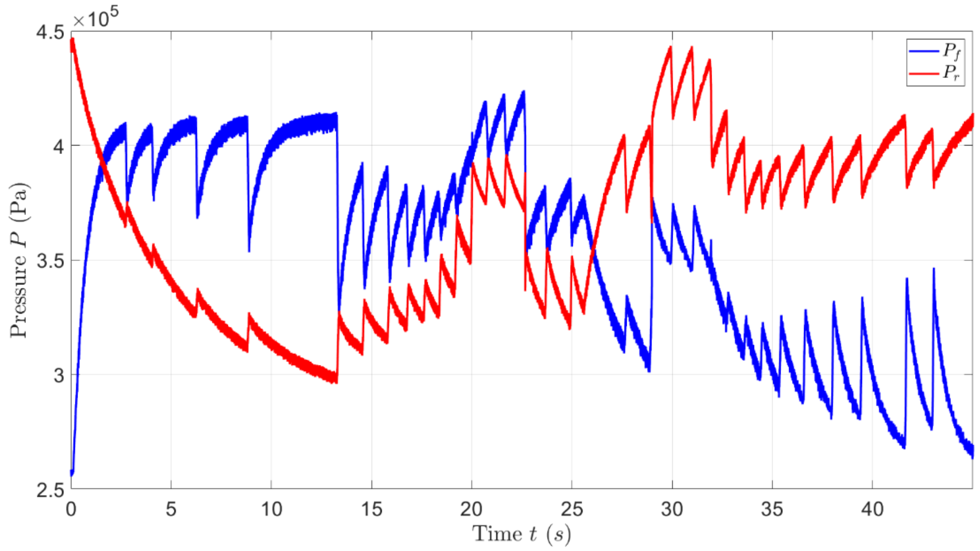

Figure 3.5d: Chamber pressures.

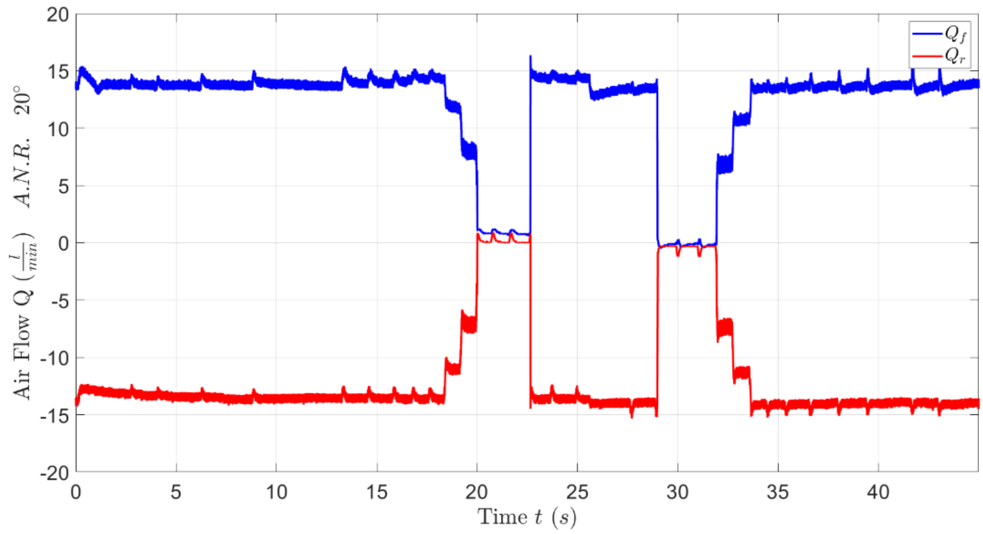

Figure 3.5e: Air flow.

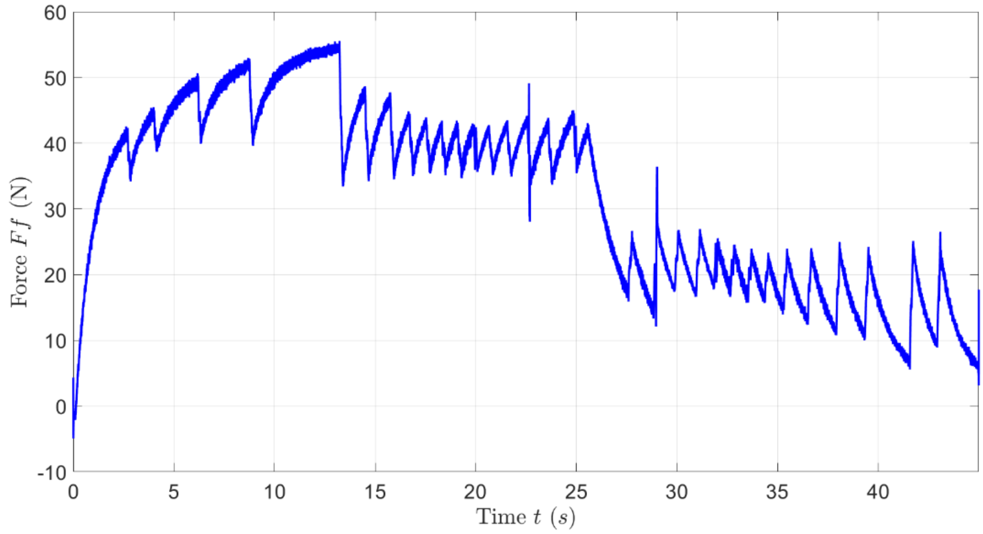

Figure 3.5f: Friction force.

Test 3

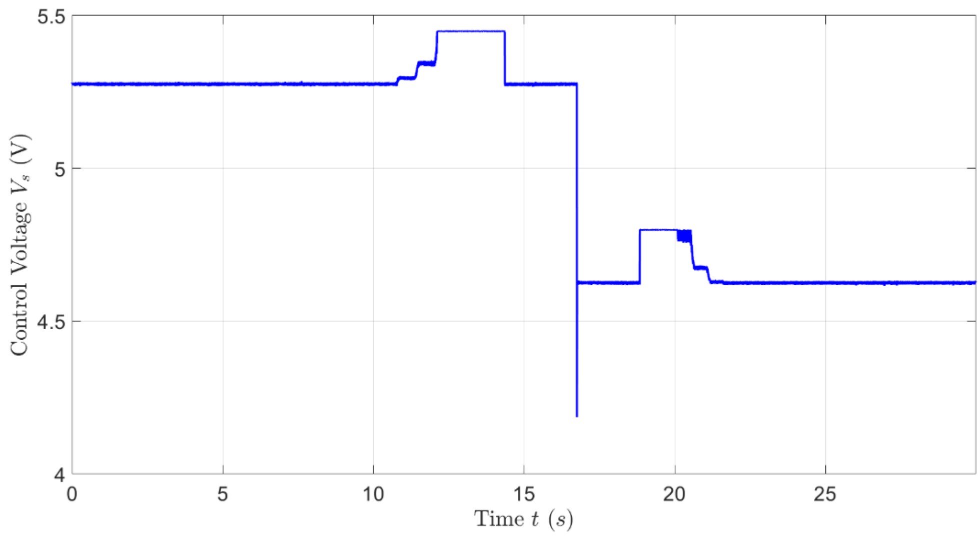

Figure 3.6a: Driving voltage.

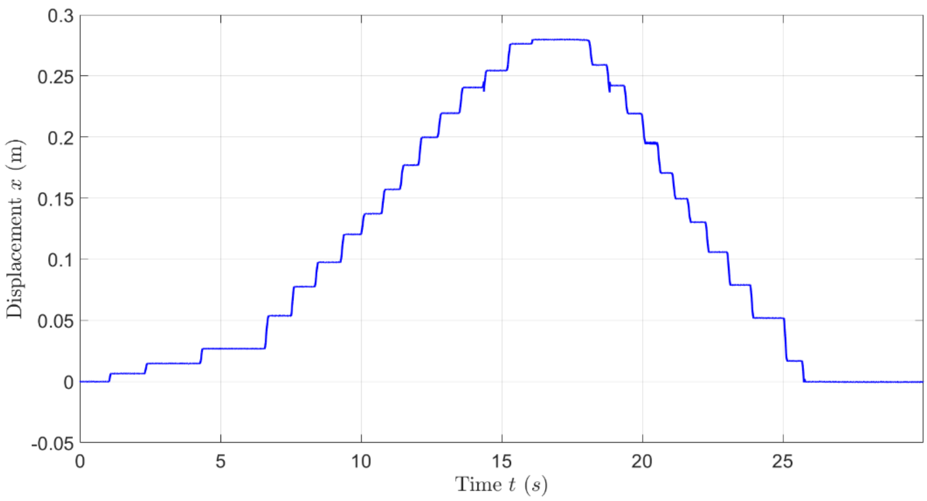

Figure 3.6b: Cart displacement.

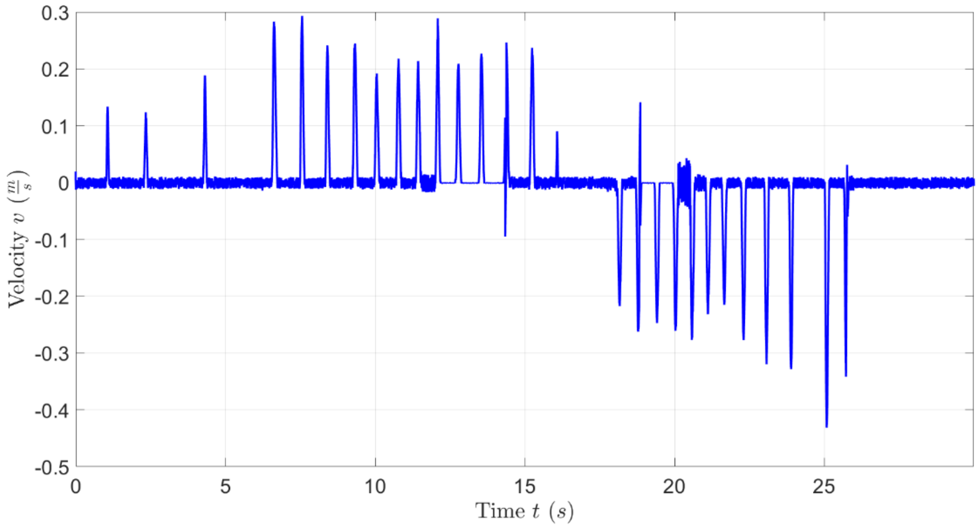

Figure 3.6c: Cart velocity.

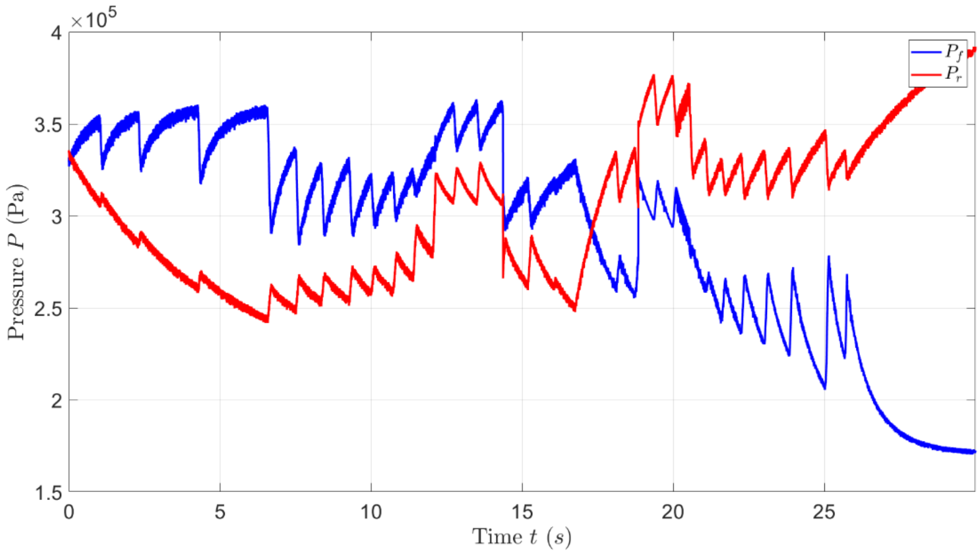

Figure 3.6d: Chamber pressures.

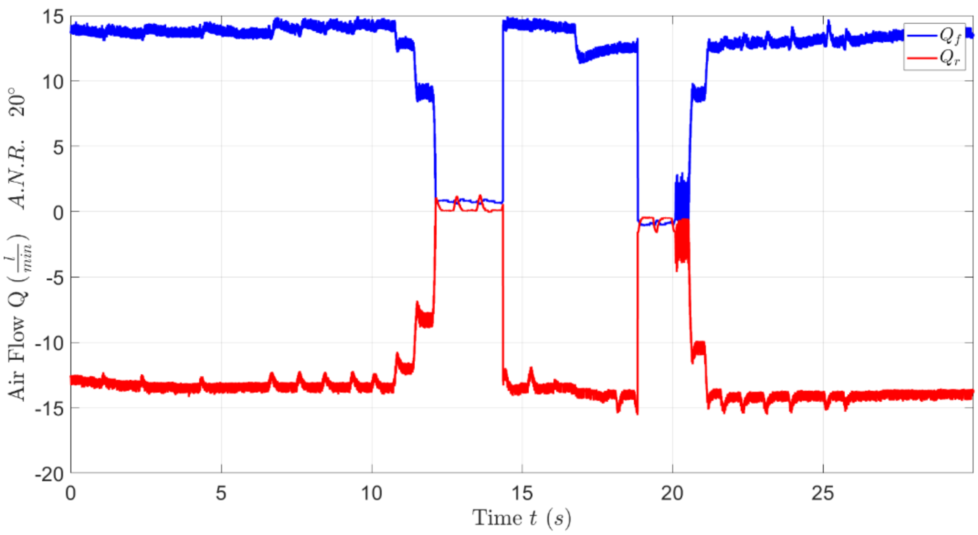

Figure 3.6e: Air flow.

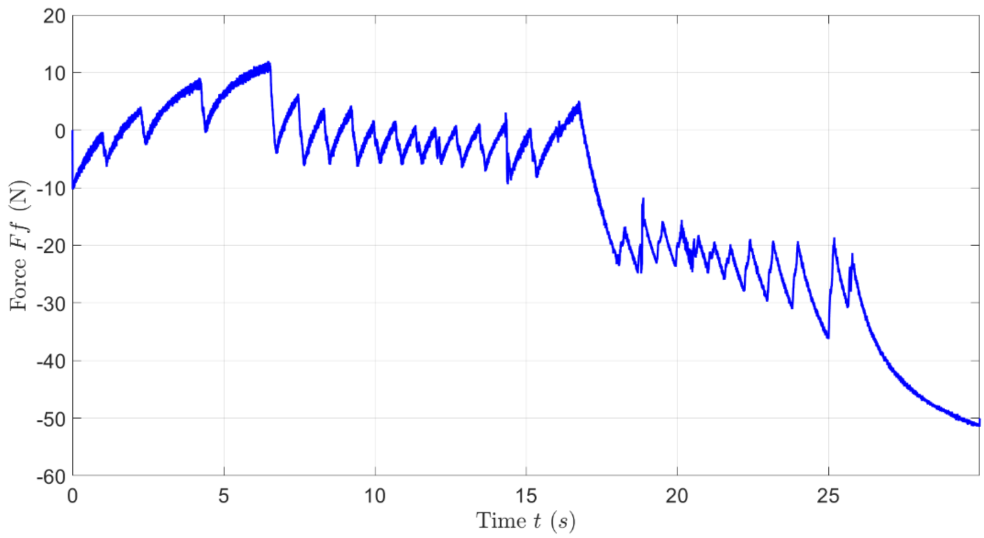

Figure 3.6f: Friction force.

Test 4

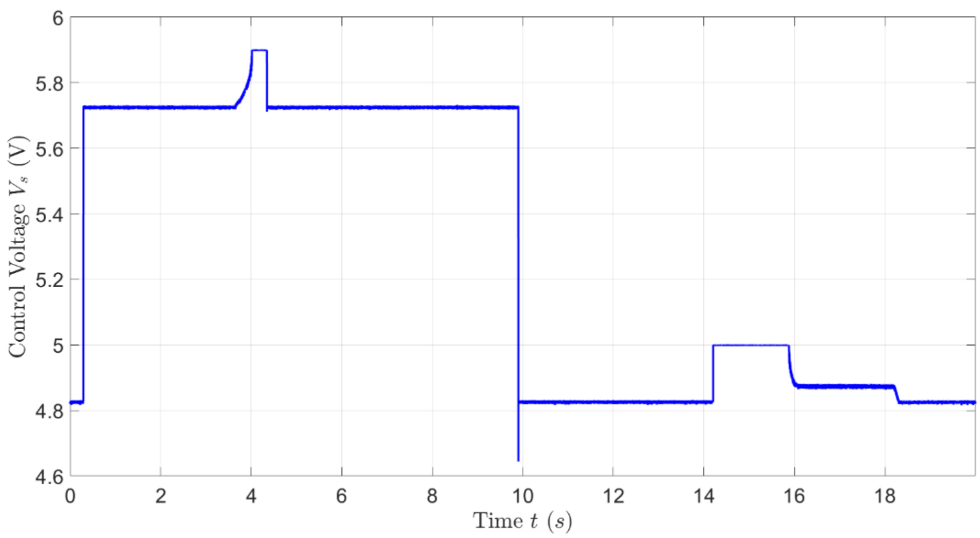

Figure 3.7a: Driving voltage.

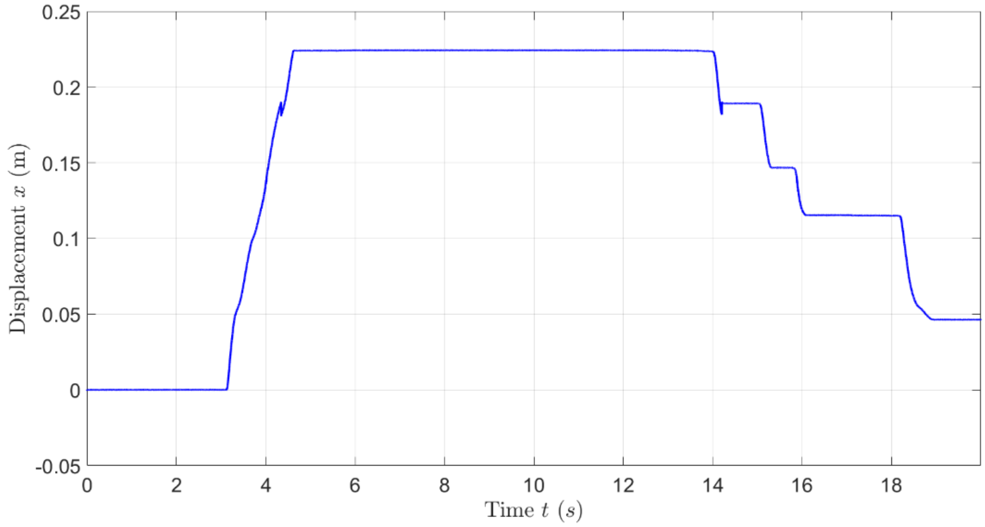

Figure 3.7b: Cart displacement.

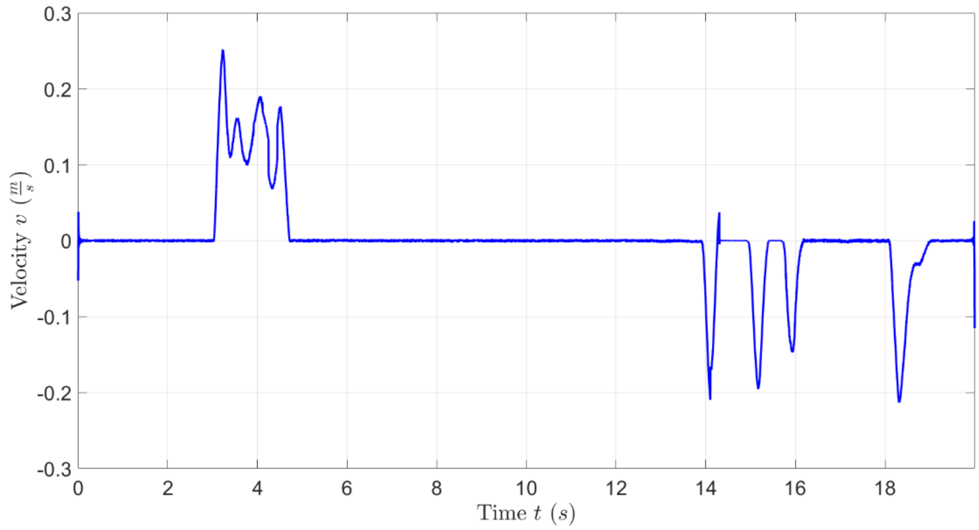

Figure 3.7c: Cart velocity.

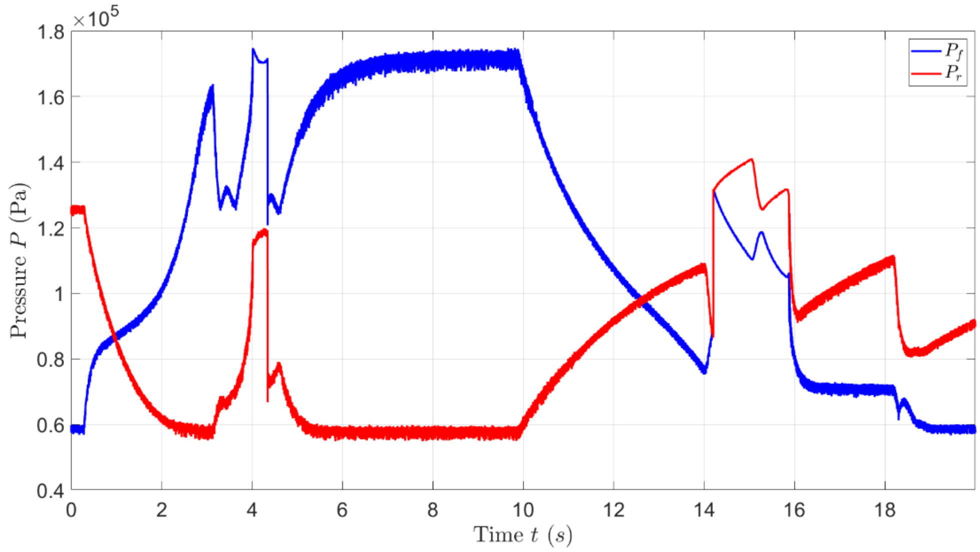

Figure 3.7d: Chamber pressures.

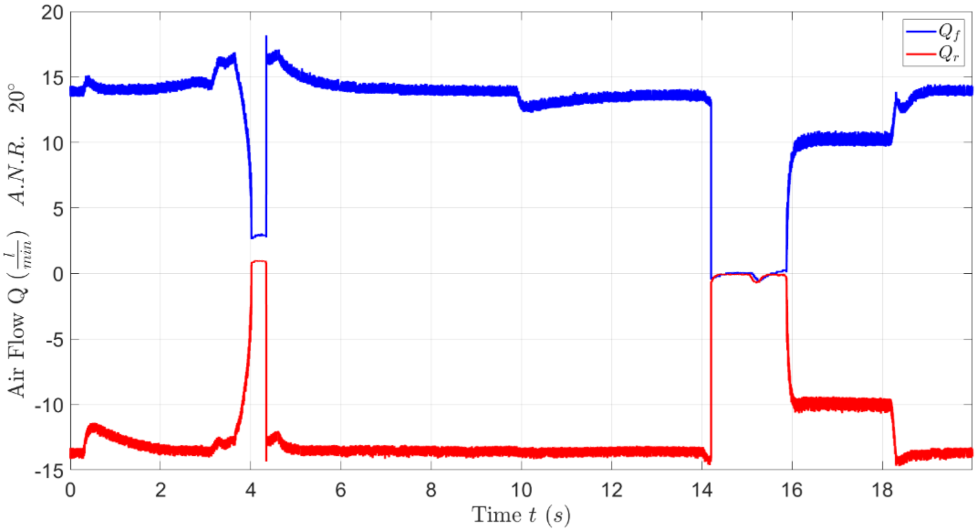

Figure 3.7e: Air flow.

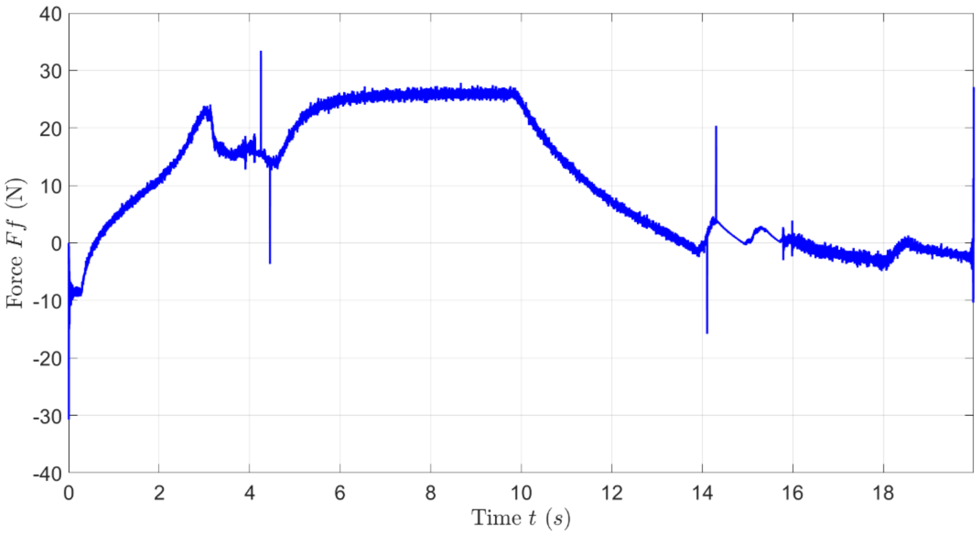

Figure 3.7f: Friction force.

3.3 Gross-sliding regime

On the same test bench, but in two different configurations (see Figure 2.11a and 2.11b), gross-sliding regime tests were performed. This kind of test was performed in order to study the positioning system behaviour under different working conditions: valve supply pressure, driving voltage and frequency. These tests were used to draw Stribeck curves and identify the gross sliding parameters that have to employed in the numerical models.

3.3.1 First configuration

The test in the first configuration consists in the application of a sinusoidal control voltage to the control valve $V_s(t) = V_{s_0} + \Delta V_s \sin(2\pi f t)$. Different operating conditions were considered: supply voltage amplitudes ΔV_s and oscillation frequencies f. The mean driving voltage and supply pressure of the valve were taken constant and equal to 5 V and 0.49 absolute MPa. The supply voltage amplitudes ΔV_s was varied from 1 to 4 V, whereas the excitation frequency ranged from 0.4 to 7 Hz.

The duration of each the test was about 15 s. The physical quantity that are measured and acquired were: the position (x) and cart velocity ($\dot{x}$), the pressures (P_f and P_r) and the in and out flow (G_f and G_r) related to the cylinder chambers along with the driving voltage (V_s) applied to the valve terminals.

3.3.1.1 Overall Results

At the beginning of each test, the valve is in its neutral position, where there is no output or discharge flow from the valve, and the driving voltage is approximately 5V. Starting from this value, the control valve, receive a sinusoidal voltage signal produced via LabView. The valve shutter starts to move periodically with at the same frequency. Consequently, the cart starts its motion with a certain time delay depending on the cylinder dynamics. The cart motion is also periodical, but it is sinusoidal only when the excitation frequency is higher than 2 Hz. At low excitation frequencies, the cart displacement does not follow a sinusoidal trend, since, at motion reversal, there is a time interval in which the piston-cart-rod system sticks. Subsequently, the system starts moving again when the pressure force overcomes the breakaway one.

The velocity reflects the displacement trend: it has a periodic behaviour but, at frequencies lower than 2 Hz, it does not exhibit a sinusoidal trend due to the system stiction.

The behaviour of the two pressures P_f (front chamber) and P_r (rear chamber) is complementary: when the valve is supplied with a control voltage lower than 5V, it provides compressed air to the front chamber and connect the rear one to the vent. The opposite occurs when the supply voltage is higher than 5 V. When the difference between the pressure in the chambers generates a force that overcome the breakaway one, the cart moves.

Generally, the friction force follows a periodic behaviour, but it is not perfectly sinusoidal. In each period, the maximum value of the friction force presents almost the same value since the system moves between the same extremes and the interaction between the asperities of the mating surfaces reproduce almost identically.

Regarding Stribeck curves (see Figure 3.11), they modify their shape depending on the excitation frequency applied at the valve terminals. At frequency lower than 2 Hz, the Stribeck curves exhibit the classical shape that characterize dry and lubricated contact. When the driving force applied to the system is lower than the breakaway one, the system sticks. As the driving force exceeds the breakaway one, the system exhibits the characteristic Stribeck and viscous effects. Conversely, at excitation frequencies higher than 2 Hz, the shapes of the Stribeck curves resembles that of an ellipse since the system does not sticks at motion reversal.

3.3.1.2 Test 1
$\boldsymbol{f = 1Hz, V_{s_0} = 5V, \Delta V = 2V, P_s = 4\ bar}$

Figure 3.8 shows the experimental test related to test 1. Figures 3.8a, 3.8b, 3.8c, 3.8d, 3.8e, 3.8f and 3.8g show the trend of the valve driving voltage, the displacement and velocity of the cart, the pressures and air flow of the cylinder chambers, friction force and Stribeck curve recorded during the test 1.

In Figure 3.8a it is possible to notice that at the beginning of the trial, the input voltage starts its sinusoidal shape starting from a value of about 5 V. The piston does not move immediately (see Figure 3.8b and 3.8c) and stays in the pre-sliding regime until 0.17 s. In this regime, micro-displacements occur but they cannot be spotted in the Figures because of the sensor that is not able to see such as small movements. During this first time interval (see Figure 3.8d and 3.8e), the pressure in the front chamber increases thanks to the constant inflow provided by the control valve. On the contrary, the pressure in the rear chamber decreases since it relates to the discharge port of the valve. Accordingly with these pressure trends, the computed friction force (Figure 3.8f) gradually increases till the breakaway value.

The cylinder starts its outstroke and instroke motion, when the driving voltage is lower than 4.2 V and higher than 5.75 V. Conversely, when the driving voltage ranges from 4.2 to 5.75 V, the system sticks since the air flow provided by the valve is not enough to reach a pressure force to overcome the breakaway force. At velocity reversal, the system stops for a time interval of about 0.18s. At about 0.62 s, the driving voltage signal is big enough to increase the force given by the pressure difference let the piston starts the motion and the cart starts to move in the opposite direction. This behaviour repeats until the end of the data acquisition.

Figure 3.8g shows the Stribeck curve of test 1.

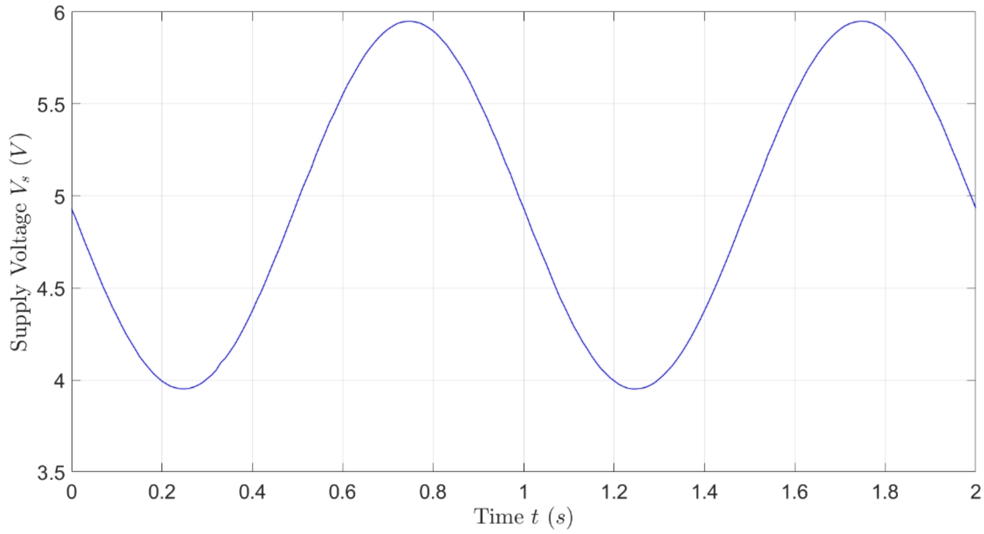

Figure 3.8a: Driving voltage.

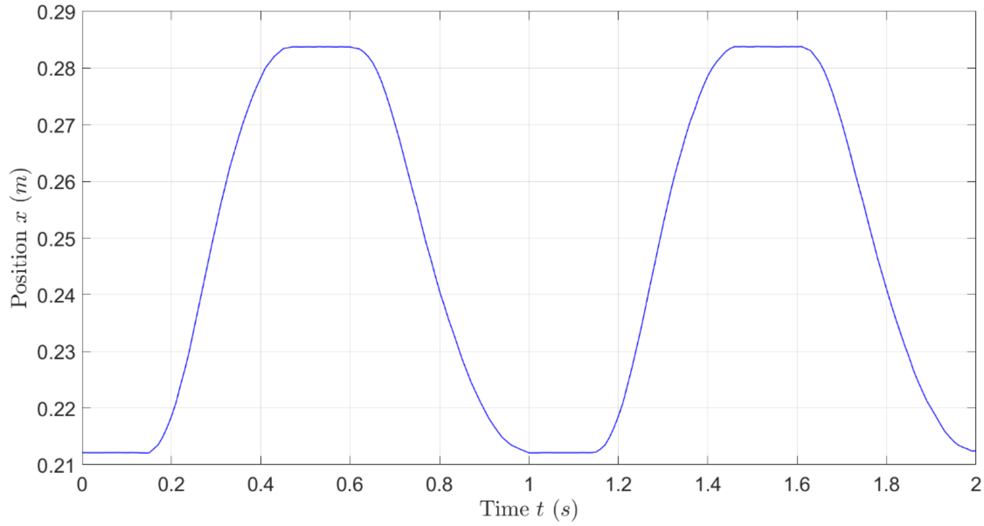

Figure 3.8b: Cart displacement.

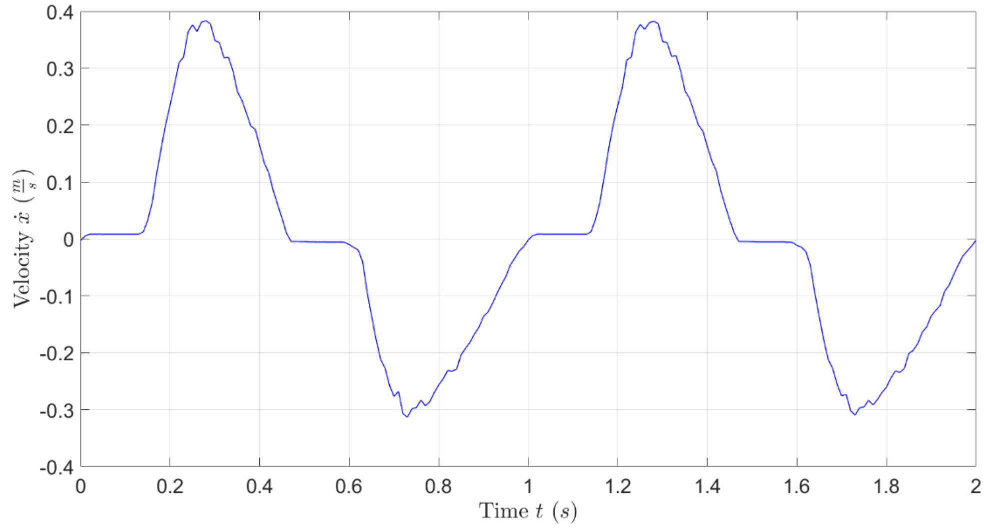

Figure 3.8c: Cart velocity.

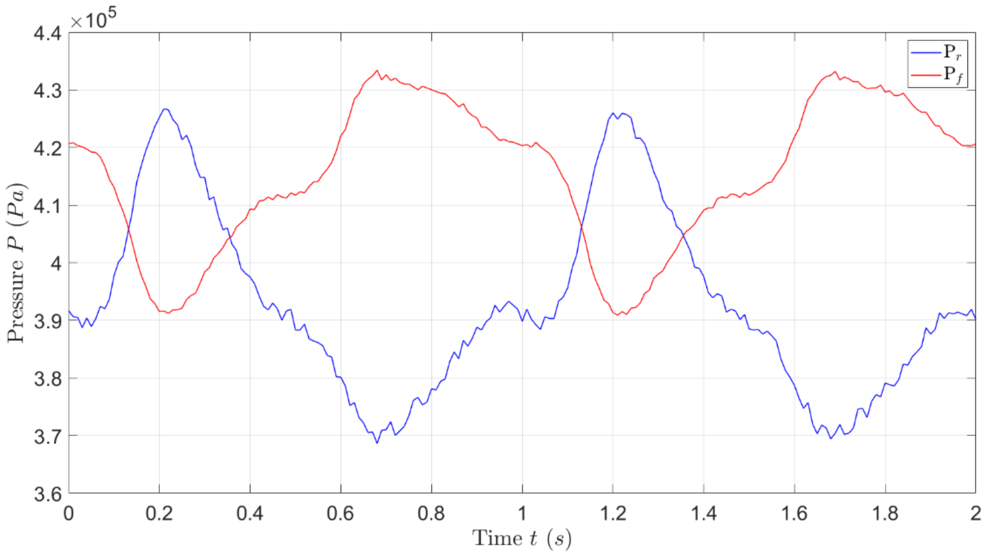

Figure 3.8d: Chamber pressures.

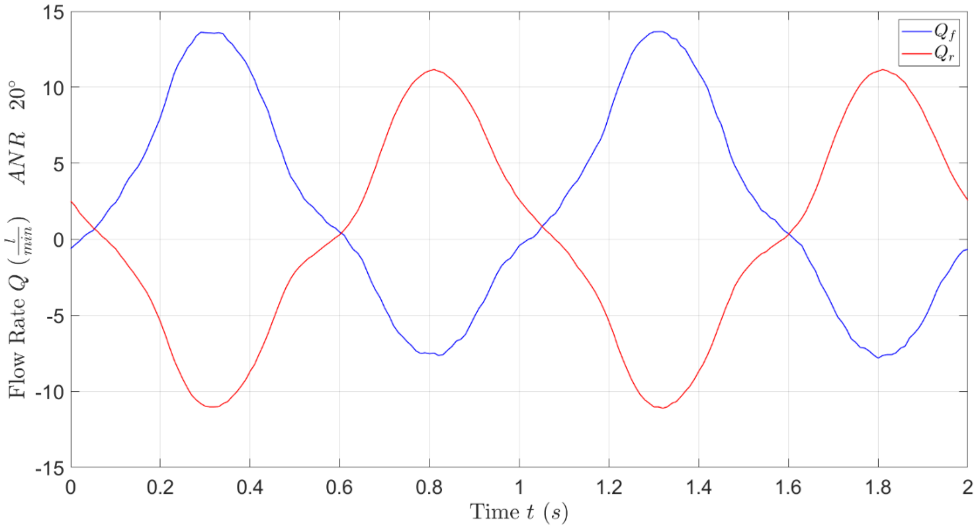

Figure 3.8e: Air flow.

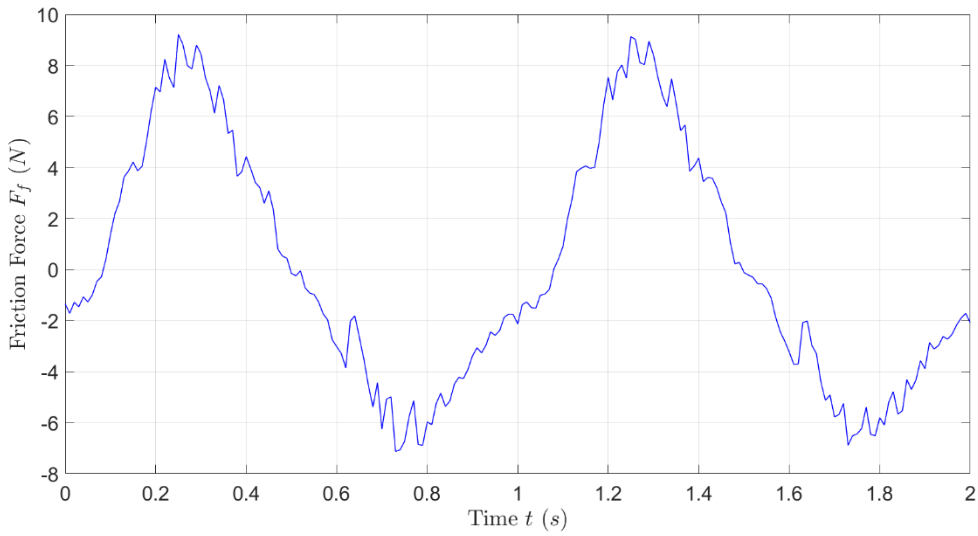

Figure 3.8f: Friction force.

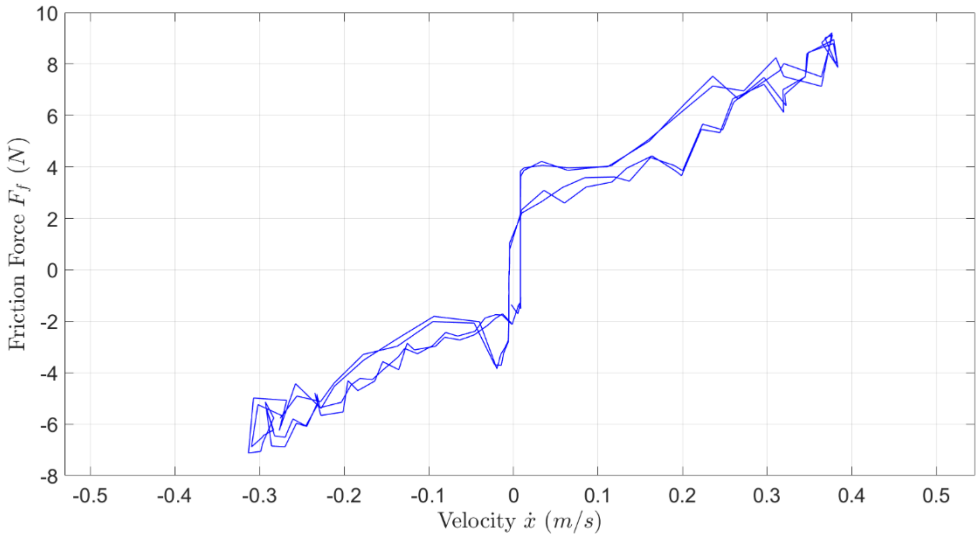

Figure 3.8g: Stribeck curve.

3.3.1.3 Test 2

$\boldsymbol{f = 4Hz, V_{s_0} = 5V, \Delta V = 2V, P_s = 4bar}$

In test 2, the motion frequency is higher than that in test 1. This produces a different behaviour of the system during its motion. In this case, the stiction time are so small that are not visible, and the displacement, the velocity, the air flow and pressures follow an almost ideal sinusoidal trend.

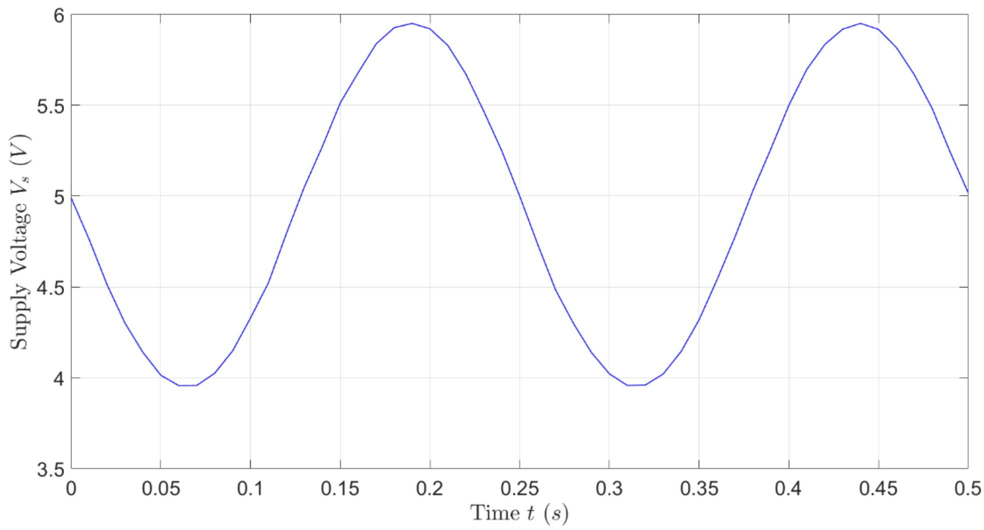

Figure 3.9a: Driving voltage.

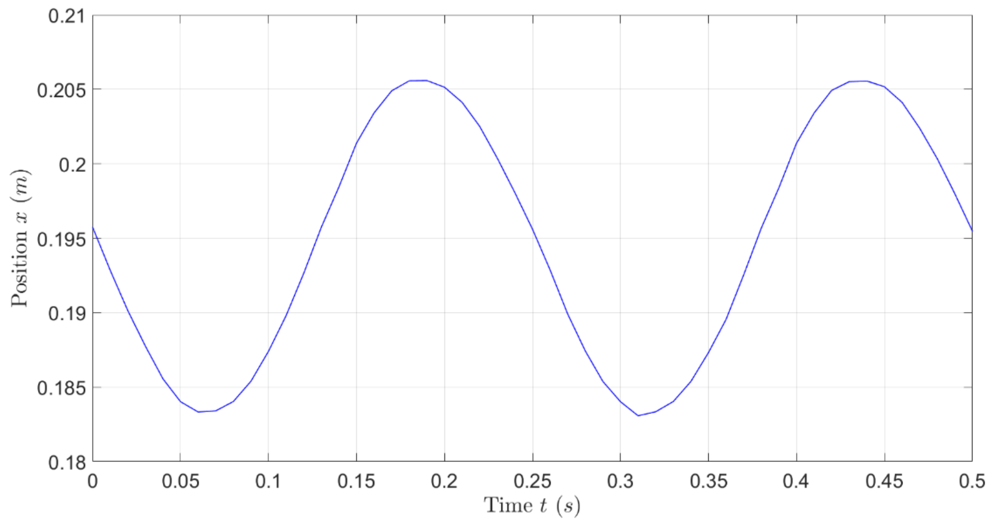

Figure 3.9b: Cart displacement.

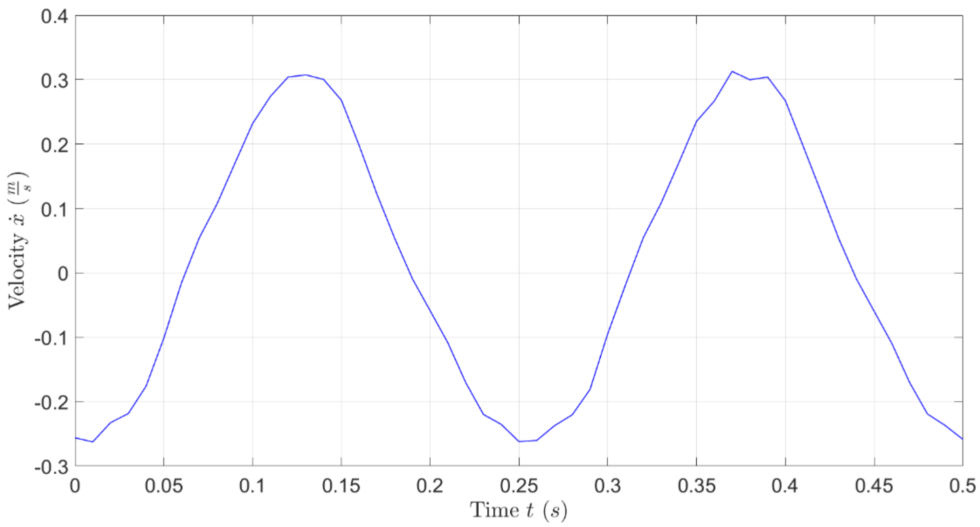

Figure 3.9c: Cart velocity.

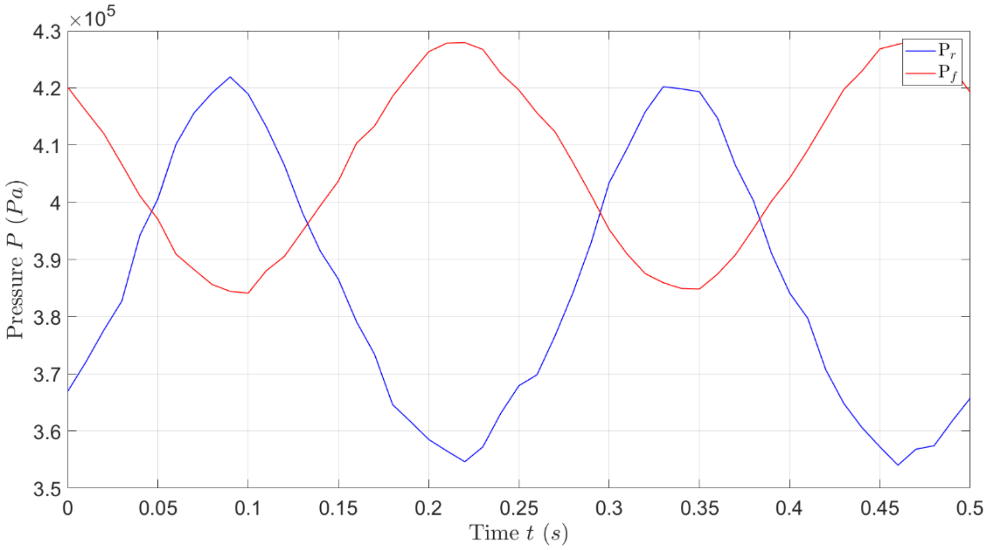

Figure 3.9d: Chamber pressures.

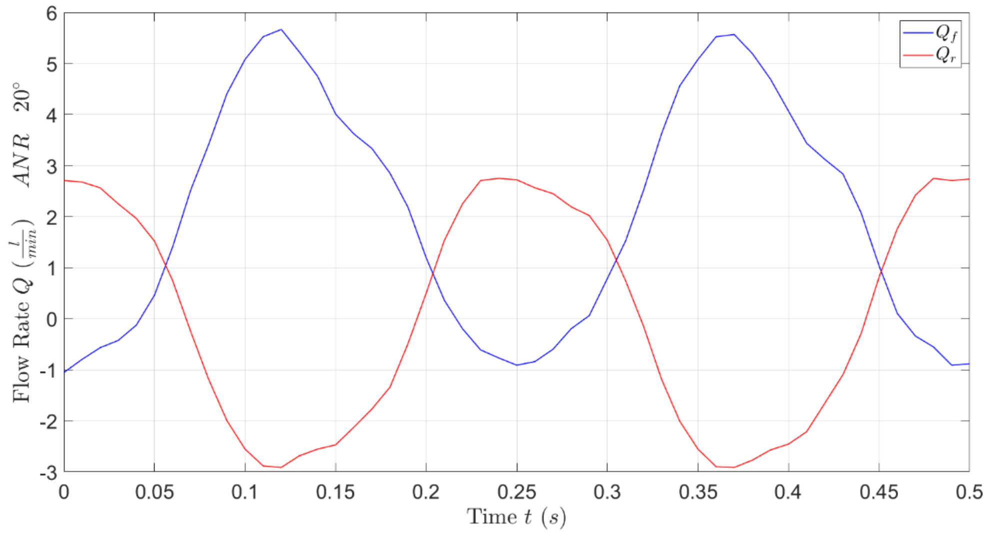

Figure 3.9e: Air flow.

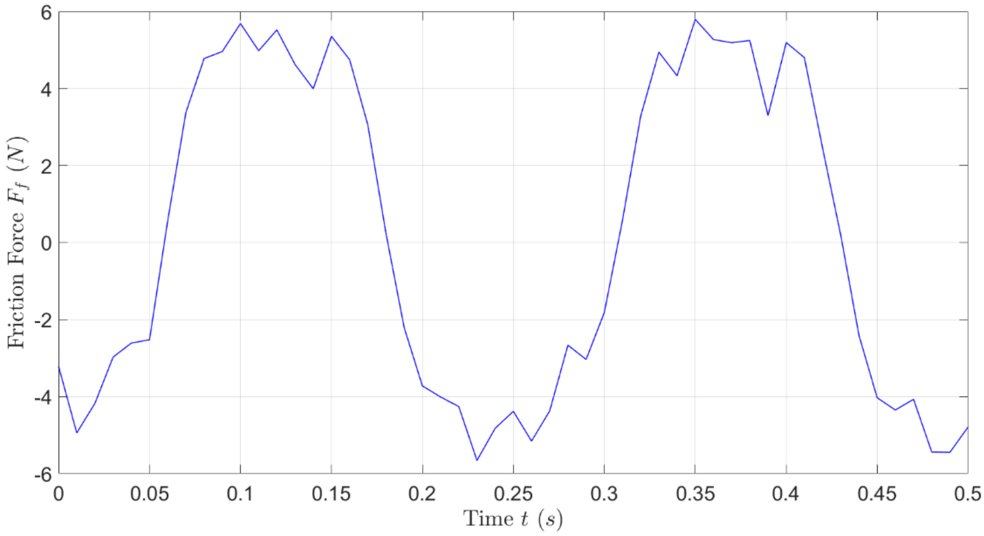

Figure 3.9f: Friction force.

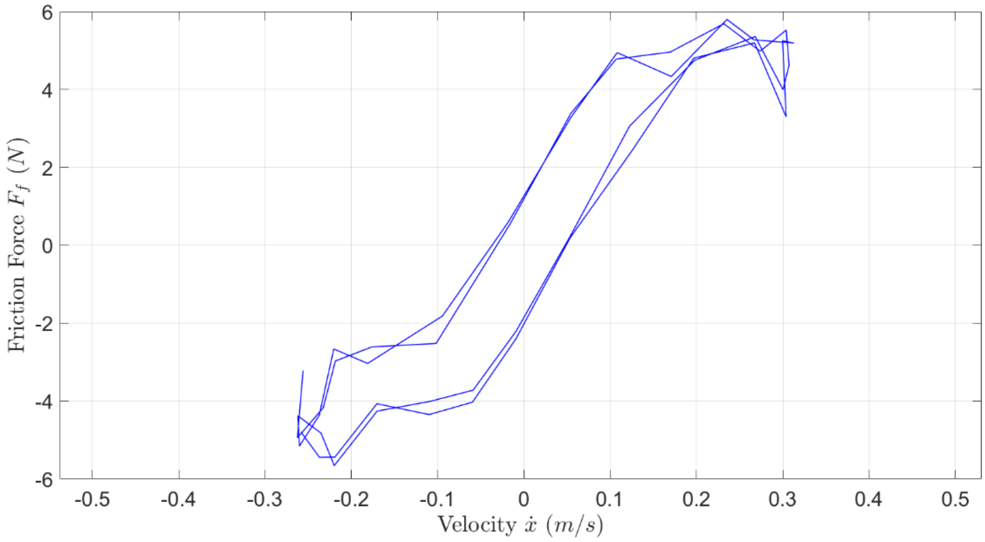

Figure 3.9g: Stribeck curve.

3.3.1.4 Test 3

$\boldsymbol{f = 6Hz, V_{s_0} = 5V, \Delta V = 2V, P_s = 4bar}$

Since the behaviour experienced in the test 3 is quite similar that of test 2, the other experimental results are reported without any additional comments.

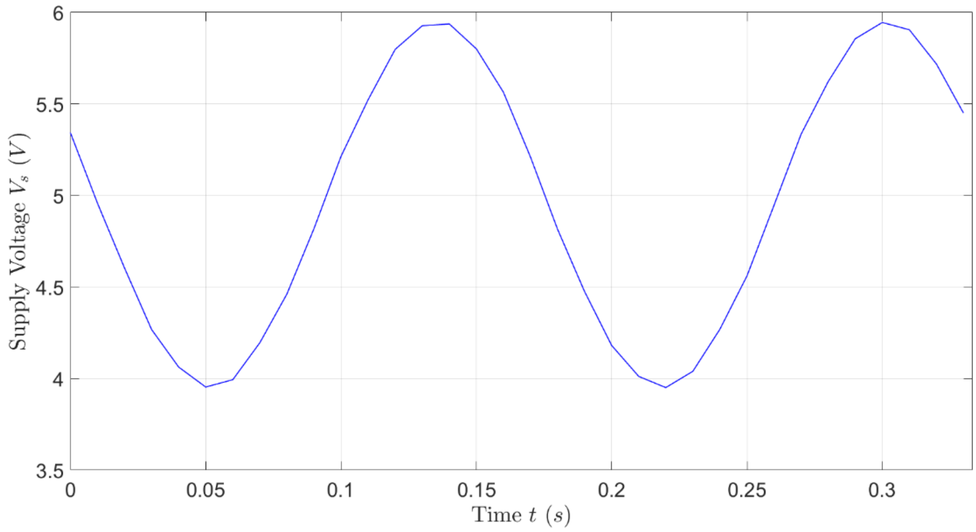

Figure 3.10a: Driving voltage.

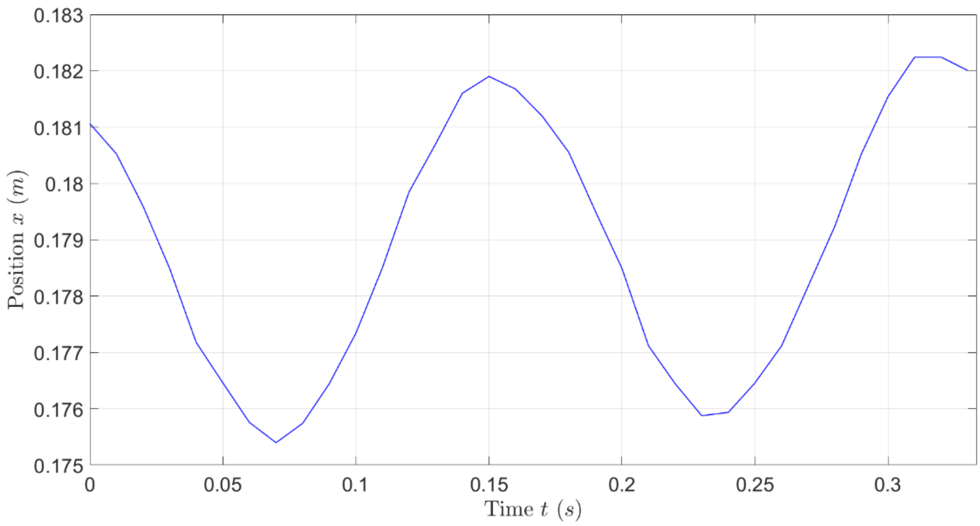

Figure 3.10b: Cart displacement.

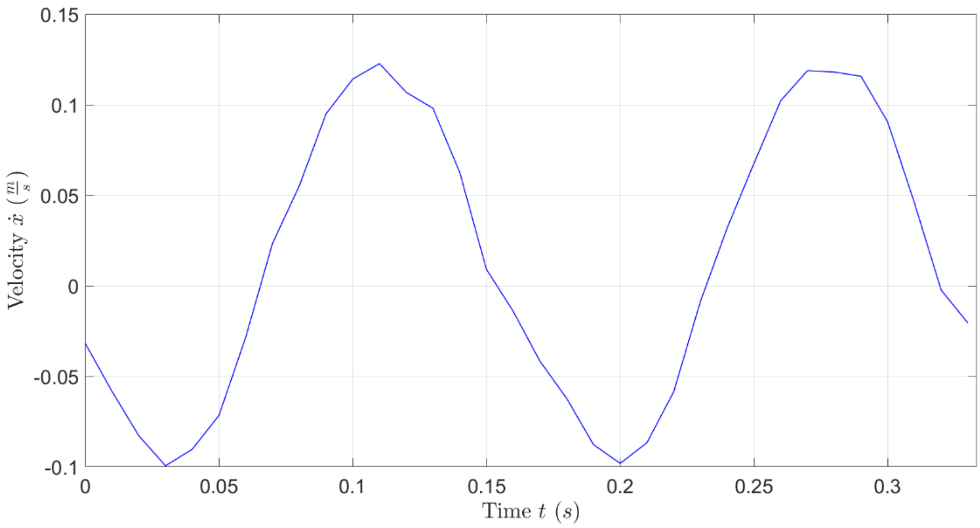

Figure 3.10c: Cart velocity.

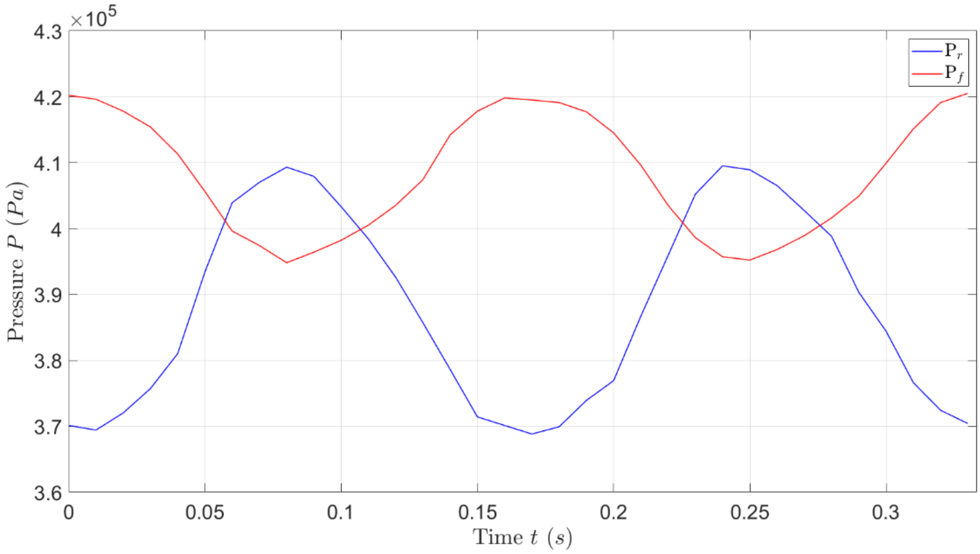

Figure 3.10d: Chamber pressures.

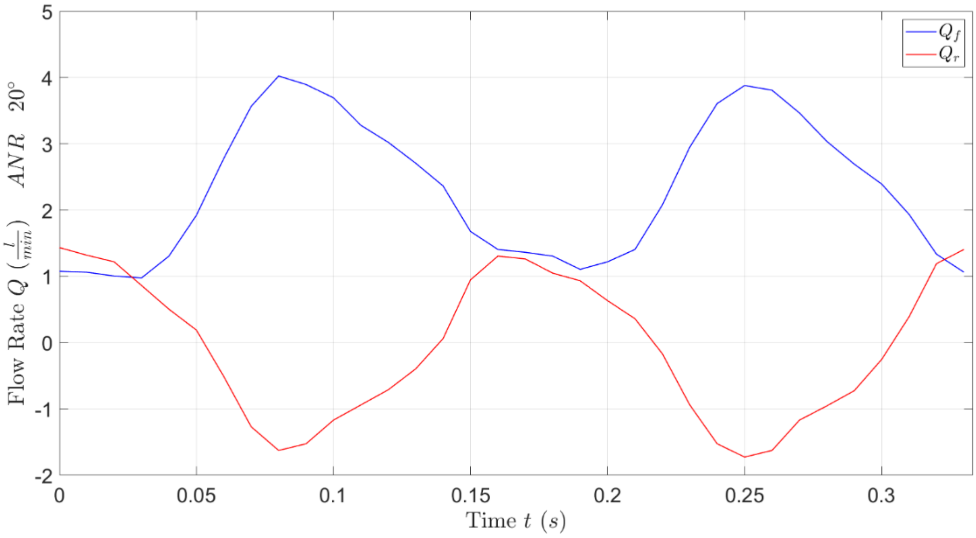

Figure 3.10e: Air flow.

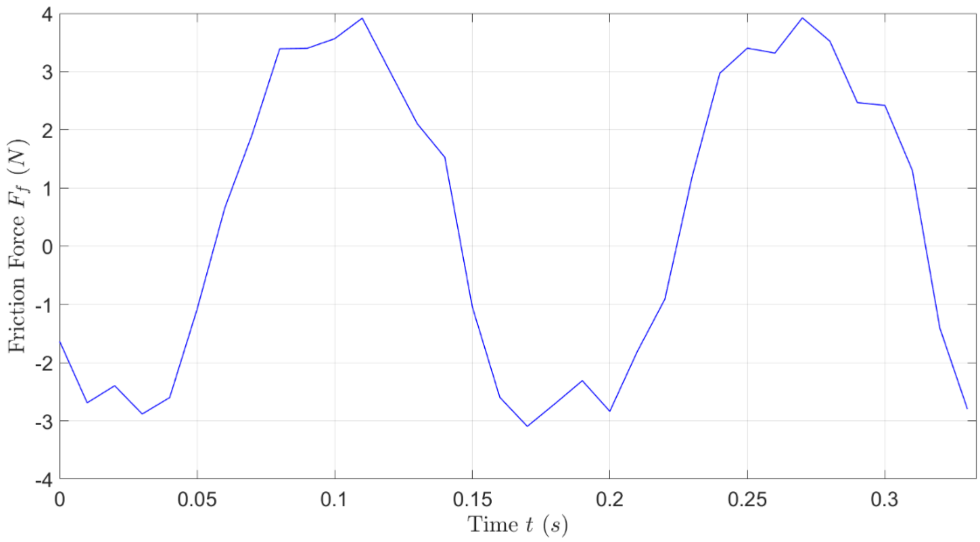

Figure 3.10f: Friction force.

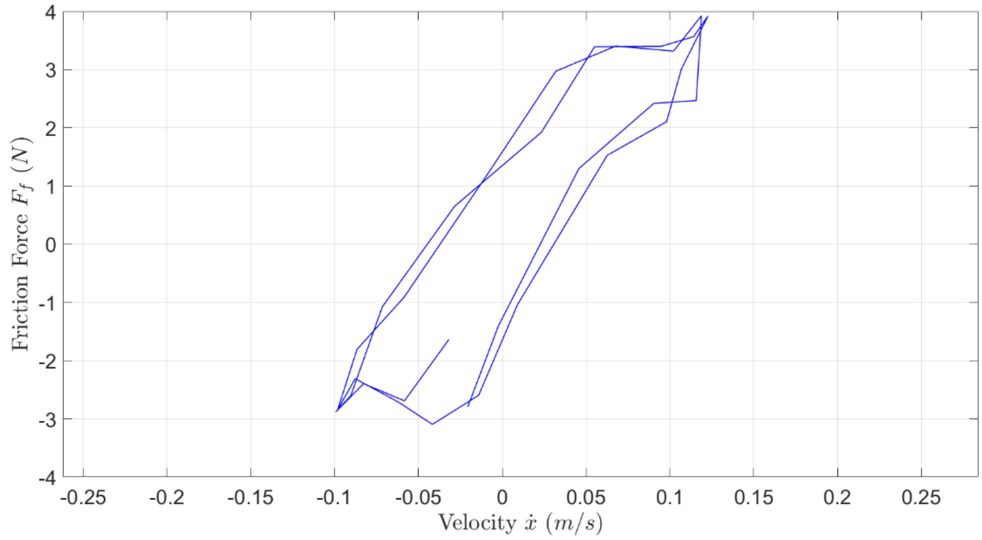

Figure 3.10g: Stribeck curve.

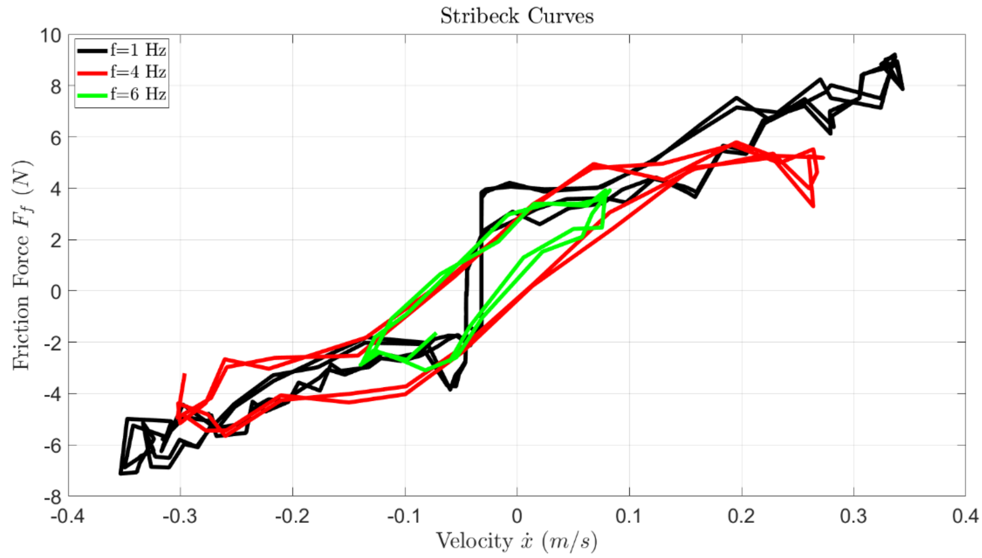

Figure 3.11: Stribeck curves comparison.

3.3.2 Second configuration

In the second configuration, one of the cylinder chambers was supplied by a Camozzi pressure regulator, whereas the other one was kept plugged. The pressure regulator was controlled with a sinusoidal voltage signal $V(t)$ following the equation $V(t) = V_0 + \Delta V sin(2\pi f t)$ with V_0 = 1.10 ÷ 4.40 V (Offset), f = 1 ÷ 3 Hz (frequency), and ΔV = 0.4 V (amplitude). The plugged chamber was initially set to a constant pressure value ranging from 0.2 to 0.5 MPa. To investigate the impact of the plugged chamber volume, a 1-liter tank was connected to it in some experiments. The physical quantity that are measured and acquired were: the position (x) and cart velocity ($\dot{x}$), the pressures (P_f

and P_r) and the in and out flow (Q_f and Q_r) related to the cylinder chambers along with the driving voltage (V_s) applied to the valve terminals.

3.3.2.1 Overall results

The most relevant aspects experienced during the tests performed in this configuration are that:

- Give the excitation frequency and the amplitude of oscillation of the cart, the friction force is lower in the test performed with the aid of the pressure regulator.
- The pressure in the plugged chamber oscillates between two values of pressure behaving as it was a spring.
- Stribeck curves exhibit a smaller extension and cycle size a frequency increasing. The curves are also influenced by the presence of the tank that modify the curve slope.

Test Regolatore_PID_PB2_f1Hz_dV04_1

Figures 3.12 shows the results of a test performed imposing an initial pressure of 0.3 absolute MPa in the plugged chamber. Here, the volume of the chamber was increase by connecting a 1-liter tank to the plugged chamber.

Figure 3.12a shows the periodical movement of the cart like a sinusoid. Each peak, corresponds to a stiction process in which the driving force due to the difference in pressure between the chamber, is not enough to overcome the breakaway force. Figure 3.12b shows the time evolution of the cart velocity. It can be seen that some steps when velocity reach zero and those correspond to the stiction periods. As already mentioned, the driving force is due to the difference in pressure shown in Figure 3.12c: at the beginning of the trial the difference is not enough, and the cart does not move but after about 0.15s this difference increases causing the cart motion. At about 0.5s this difference decreases again, and the cart stops. Air flows trends reflect the chamber pressure behaviour as shown in Figure 3.12d: when one flow increases, the other must decrease. Generally, the friction force (Figure 3.12e) follows a periodic behaviour, but it is not perfectly sinusoidal. In each period, the maximum value of the friction force presents almost the same value since the system moves between the same extremes and the interaction between the asperities of the mating surfaces reproduce almost identically. In Figure 3.12e the Stribeck curve is plotted.

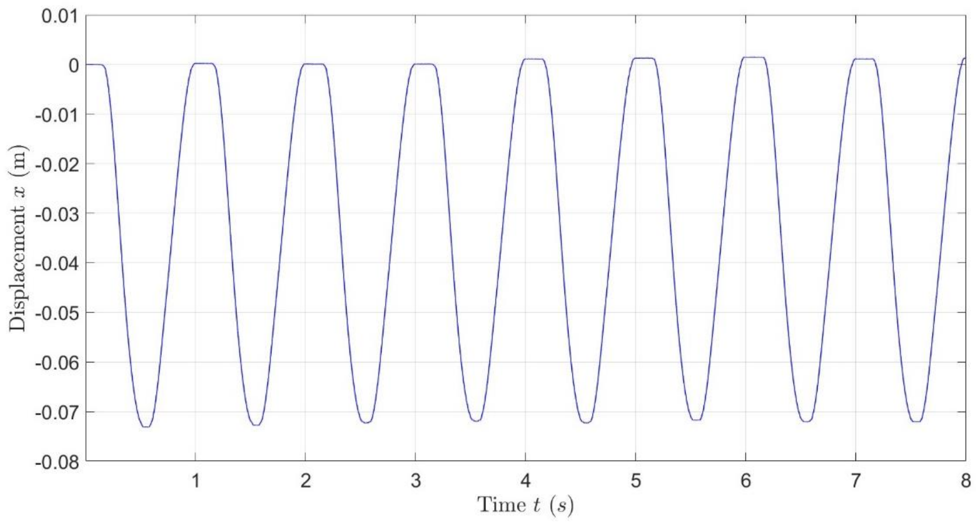

Figure 3.12a Cart displacement.

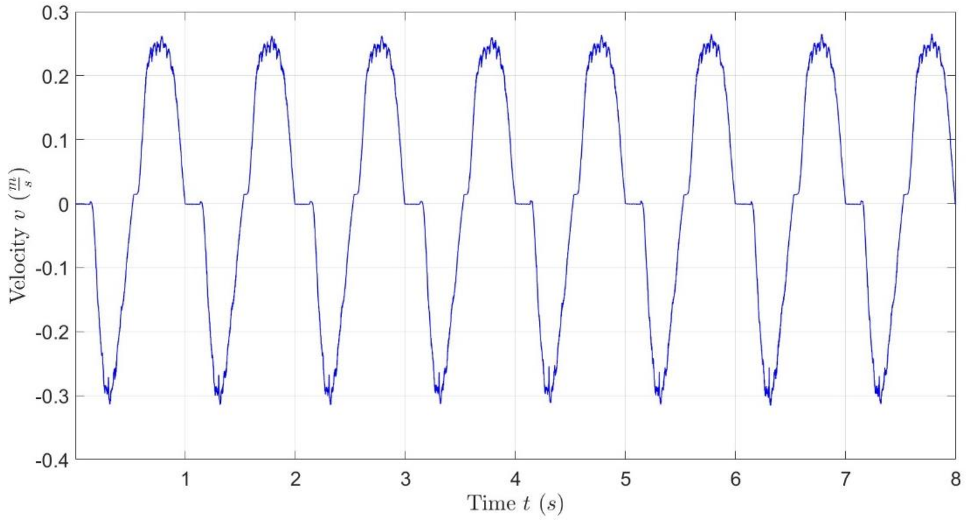

Figure 3.12b Cart velocity.

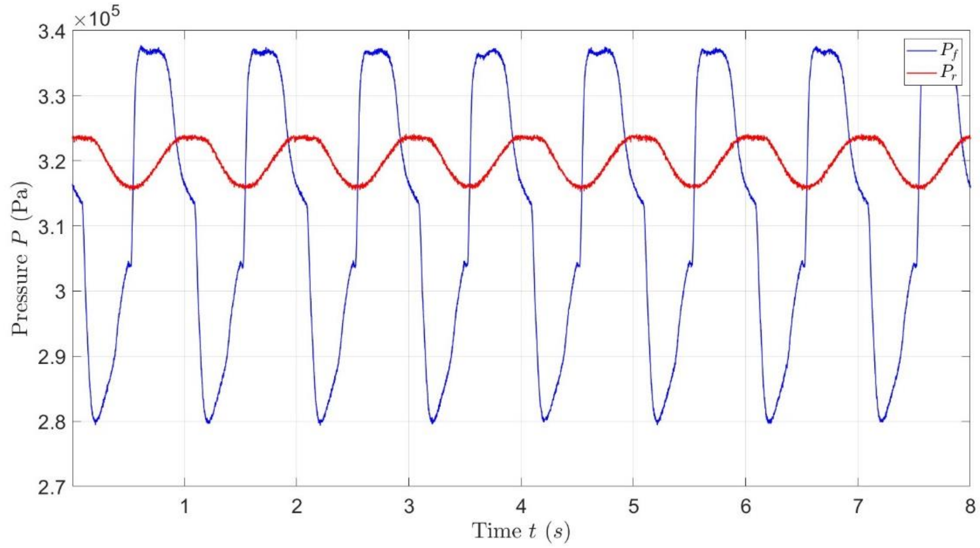

Figure 3.12c Chambers pressure.

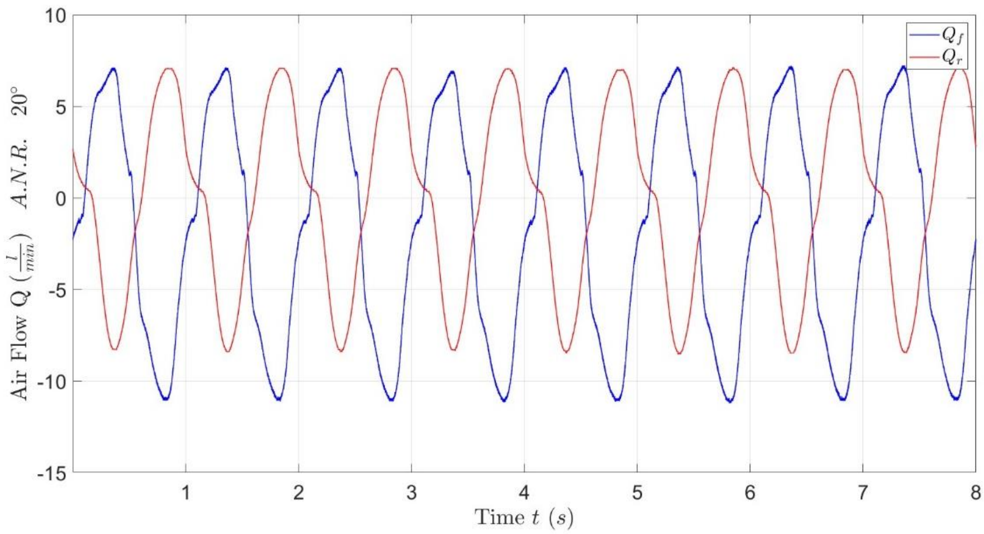

Figure 3.12d Air flow through the chamber.

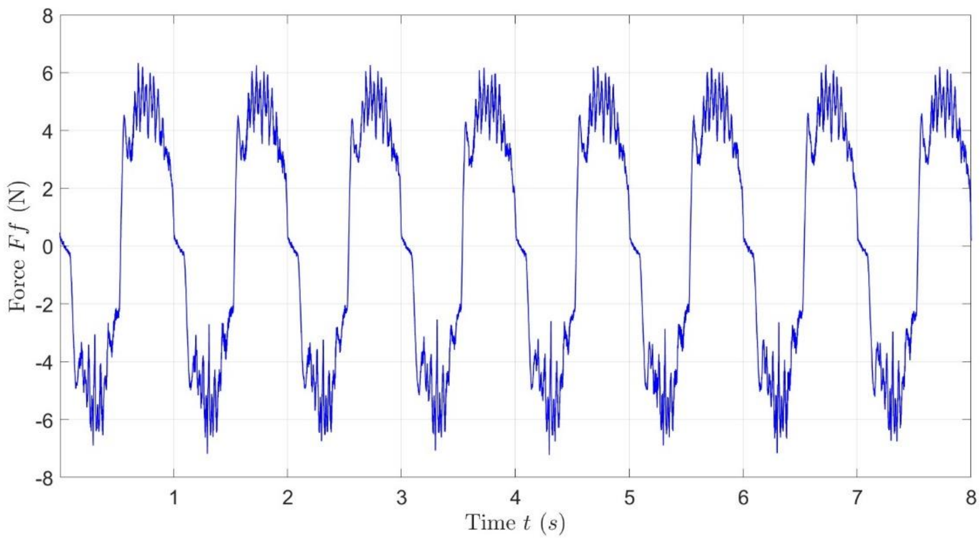

Figure 3.12e Friction force.

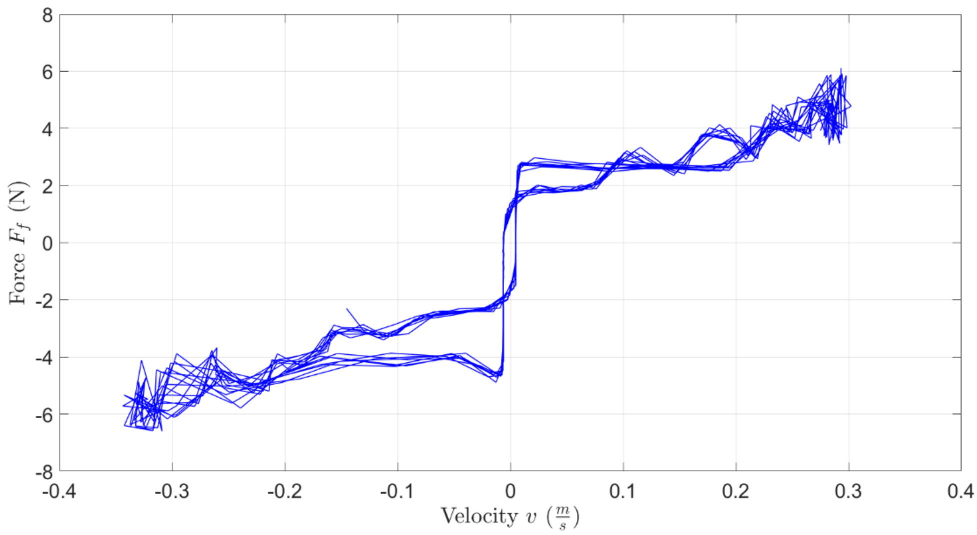

Figure 3.12f Stribeck curve.

Figures 3.13a and 3.13b show the Stribeck curve trend at frequency increasing in the case with the tank and without it. Those examples are provided at a constant pressure of 0.1 MPa.

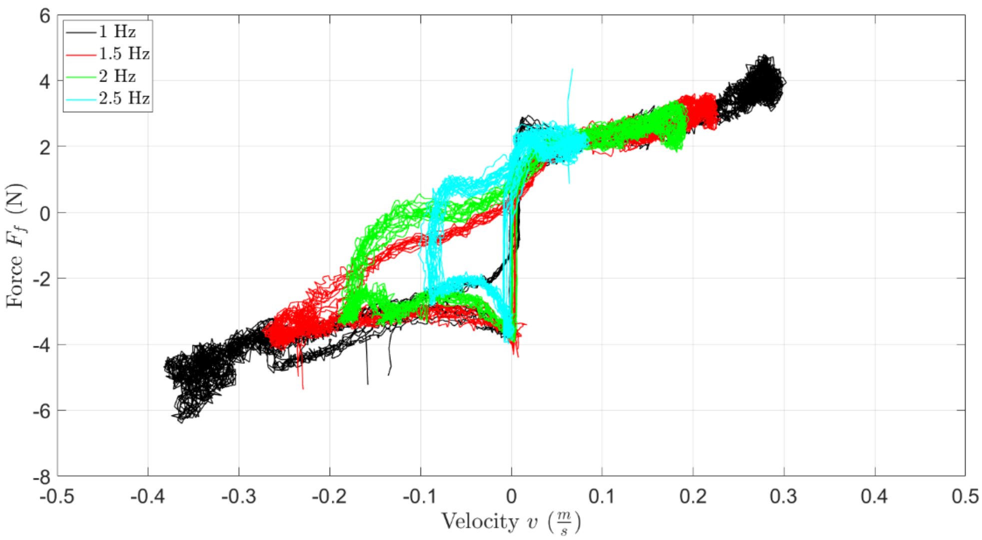

Figure 3.13a: Stribeck curves comparison with the tank.

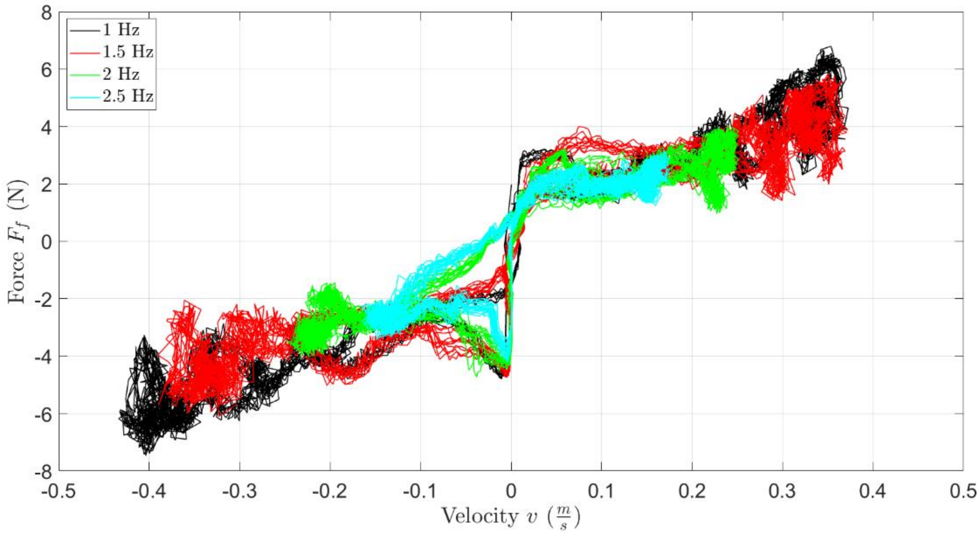

*Figure 3.13*b*: Stribeck curves comparison* without the tank.

CHAPTER 4

This chapter compares the numerical and experimental results of the investigated system. The comparison is aimed to validate the numerical models in presliding, transition and gross-sliding regimes. The numerical results come from the numerical model detailed in Sec.2.2.

4.1 Pre-sliding regime

The numerical simulation tries to find the friction force acting on a mechatronic system under pre-sliding regime. In this specific test, the system undergoes micro-displacements while velocity is almost null, and the phenomenon of hysteresis with non-local memory appears. In these cases, the friction force only depends on the deformation of the asperities of the mating surfaces. Among the implemented models, only the Leuven one is able to take into account hysteresis with non-local memory. For this reason, in this section, all the numerical results are related to Leuven model. On the other hand, the experimental test comes from [15].

The first step to identify the pre-sliding model parameter is the identification of the virgin curve. This curve relates the driving force applied to the movable part of the system and the related micro-displacement, i.e., the displacements that are measured when the driving force is lower than the breakaway one.

Also the experimental virgin curve was taken from [15]. As in [19], the mathematic formulation to fit experimental is :

$$f(x) = k_1 x - f_1\,(\exp(-f_2 \cdot x) - 1)$$

This experimental fitting was performed by Matlab Fitting Toolbox and the estimated coefficients are reported in the table below[1]:

Coefficient	Value
$\boldsymbol{k_1}\ (\boldsymbol{N/m})$	$1.483 \cdot 10^6$
$\boldsymbol{f_1}\ (\boldsymbol{N})$	5.595
$\boldsymbol{f_2}\ (\boldsymbol{1/m})$	$5.631 \cdot 10^5$

Figure 4.1 compares the experimental and fitted data.

[1] The values obtained through Matlab Fitting Toolbox were slightly modified by a trial-and-error procedure.

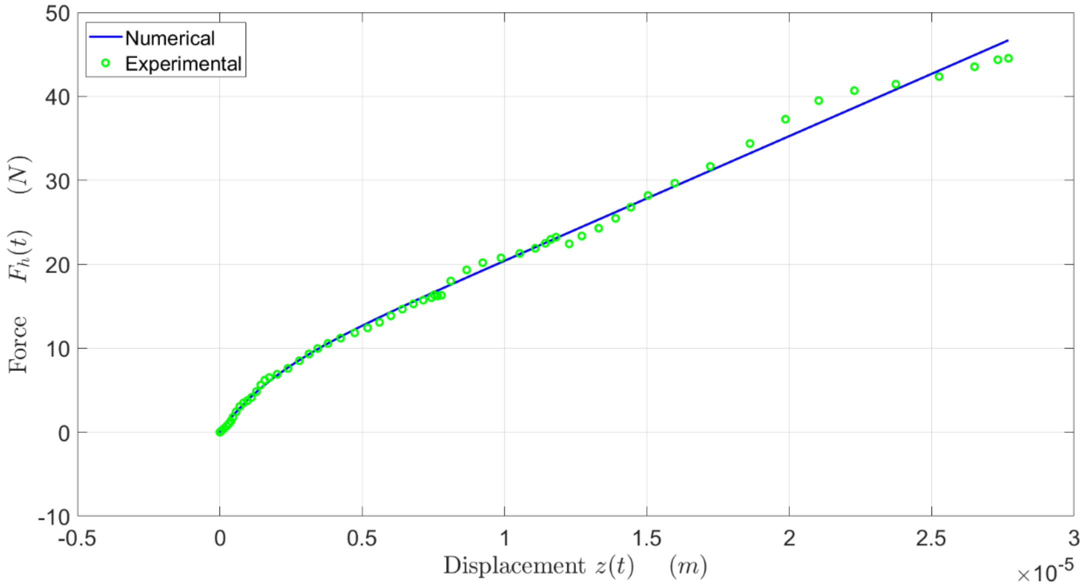

Figure 4.1 The fitted virgin curve.

Once the virgin curve has been found, the next step is to acquire the values of *z* from the experimental test and give them as input to the numerical model to find the friction force F_h .

$$F_f = F_h(z) + \sigma_1 \dot{z} + \sigma_0 z$$

$$F_h(z) = F_b + F_d(z)$$

The term $F_h(z)$ is introduced to take in account the hysteresis effects and substitutes the first term of the LuGre equation. This term is different from zero only when the velocity is null. It consists in an expression function of the bristle deformation *z*. Its value at the initiation of a transition curve (such as during a velocity reversal) is denoted as F_b. The transition curve that becomes active at a specific moment is symbolized as $F_d(z)$. $F_d(z)$ constitutes a symmetrical point-wise function of z that consistently increases. The implementation of $F_h(z)$, necessitates the utilization of two memory stacks: one to store the ascending-ordered minima of F_h (referred to as stack min), and another to house the descending-ordered maxima of F_h (referred to as stack max). These stacks expand during velocity reversals and contract when internal loops are closed. The numerical steps to compute F_b, $F_d(z)$ are reported in section 2.4. Figures 4.2 and 4.3 compares the experimental and numerical results.

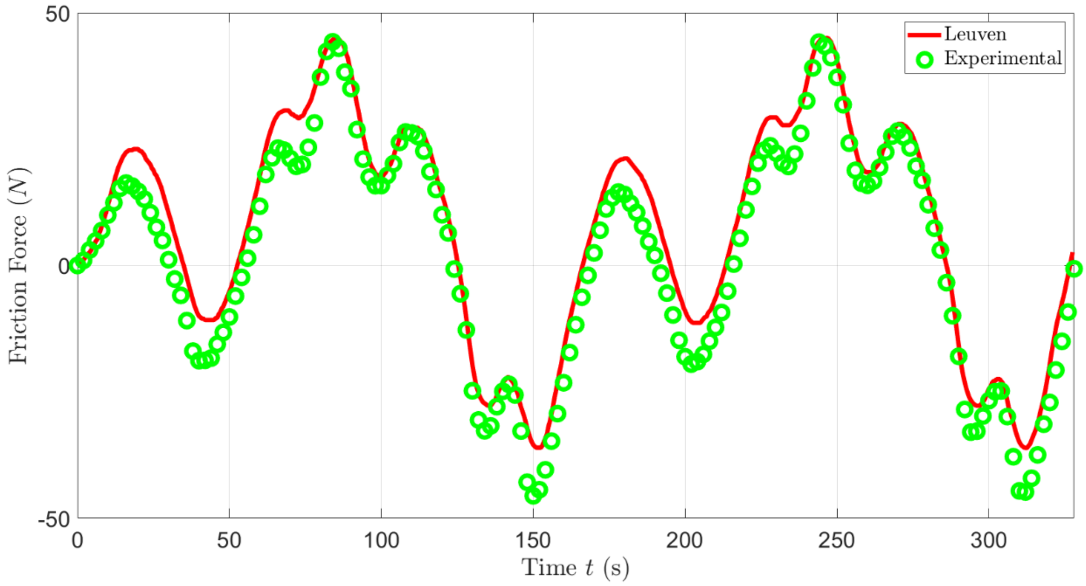

Figure 4.2 Friction force on time.

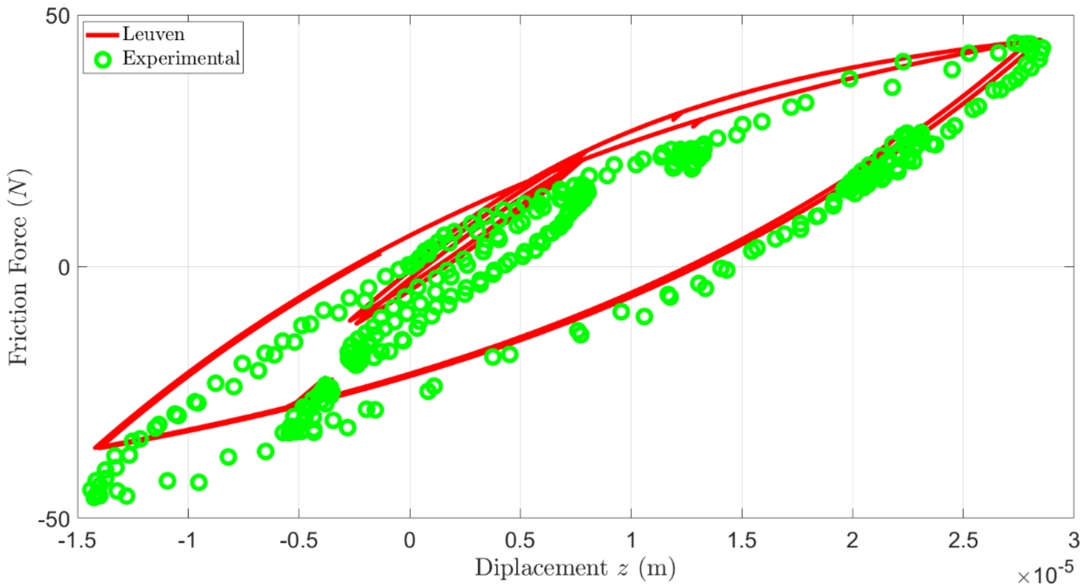

Figure 4.3 Friction force-displacement.

The friction force resulting from Leuven method follows the experimental one both on time and displacement. Figure 4.3 shows the hysteresis with non-local memory phenomenon emphasizing all the internal loops as shown in Figures 4.4a and 4.4b, but the two shapes are not coincident.

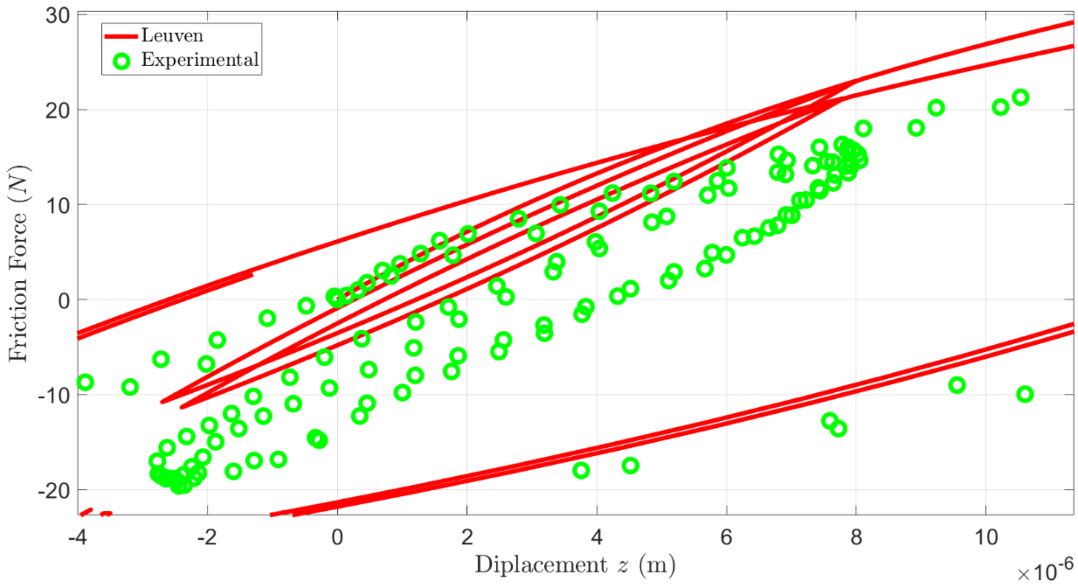

Figure 4.4a Internal loops.

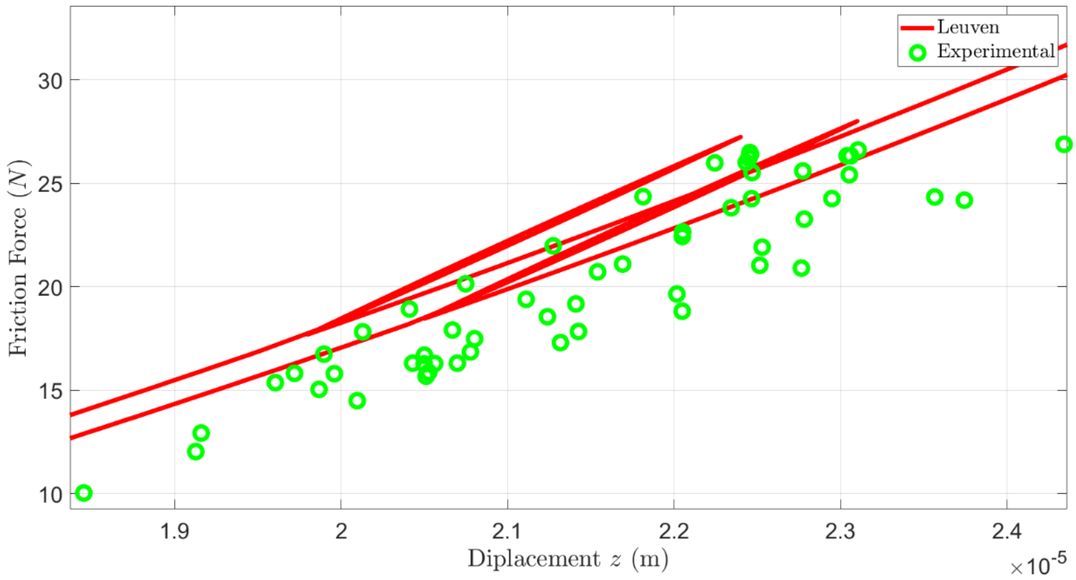

Figure 4.4b Internal loops.

4.2 Transition regime

This section compares the experimental and numerical related to a stick slip process. Here, the main goal is to evaluate the accuracy of the model prediction in the presence of stick-slip phenomena. The tests have been performed in the presence of different and constant supply pressures of the valve (from 0.1 to 0.6 relative MPa) and imposing the minimum driving voltage to generate the cart motion. The numerical results are obtained through some of the numerical model that have been discussed in the thesis: Polito, Dahl and LuGre model.

Since the absence of experimental data related to the presliding behaviour of the system, the initial identification of the presliding parameter were performed manually through a trial-and-error procedure.

As already mentioned in Sec. 3.2.2, the friction force presents a saw tooth trend but with different peaks. This difference in peaks is not optimal for a good simulation result, because different peaks mean different first detach forces. This involves a different value of the first detach force F_s at each peak. It depends on the fact that the frictional behaviour of mating surfaces is not constant during the motion of the cart. To simplify the identification of the model parameters only a portion of the test performed at 6 bar, Stick_Slip_Ps60_Vi542_Vf5_1 is considered (between 17.85s and 21.05 s). In this time interval, the friction force peaks are similar and comparable with a unique F_s.
Moreover, it is worth pointing out that the total weight of the cart-rod,-piston system is not the same as the gross-sliding regime test, because in this specific case there is not the load cell. So, the weight, goes from 0.88 kg to 0.78 kg only for this test.
The results of displacement, velocity and friction force are compared with the experimental one in Figure 4.5. Here below, the model parameters are listed:

- Polito:

Coefficient	Value
$\boldsymbol{F_s\ (N)}$	$\mathbf{10.8}$
$\boldsymbol{F_{C1}\ (N)}$	7.8
$\boldsymbol{F_{C2}\ (N)}$	7.8
$\boldsymbol{v_s\left(\frac{m}{s}\right)}$	0.01
$\boldsymbol{\varepsilon\left(\frac{m}{s}\right)}$	10^{-4}
$\boldsymbol{c_1\left(\frac{N}{\frac{m}{s}}\right)}$	33
$\boldsymbol{c_2\left(\frac{N}{\frac{m}{s}}\right)}$	25
$\boldsymbol{\delta}$	2
$\boldsymbol{mass\ (kg)}$	0.78

- Dahl model

Coefficient	Value
$\boldsymbol{F_C\ (N)}$	$\mathbf{10.6}$
$\boldsymbol{\sigma_0\left(\frac{N}{m}\right)}$	$8 \cdot 10^6$

- LuGre model

Coefficient	Value
$\boldsymbol{F_s\ (N)}$	$\mathbf{11}$
$\boldsymbol{F_C\ (N)}$	8.3
$\boldsymbol{v_s\left(\frac{m}{s}\right)}$	0.01
$\boldsymbol{\delta}$	2
$\boldsymbol{mass\ (kg)}$	0.78

$\boldsymbol{\sigma_0}\ \left(\frac{N}{m}\right)$	10^4
$\boldsymbol{\sigma_1}\ \left(\frac{N}{\frac{m}{s}}\right)$	2500
$\boldsymbol{\sigma_2}\ \left(\frac{N}{\frac{m}{s}}\right)$	30

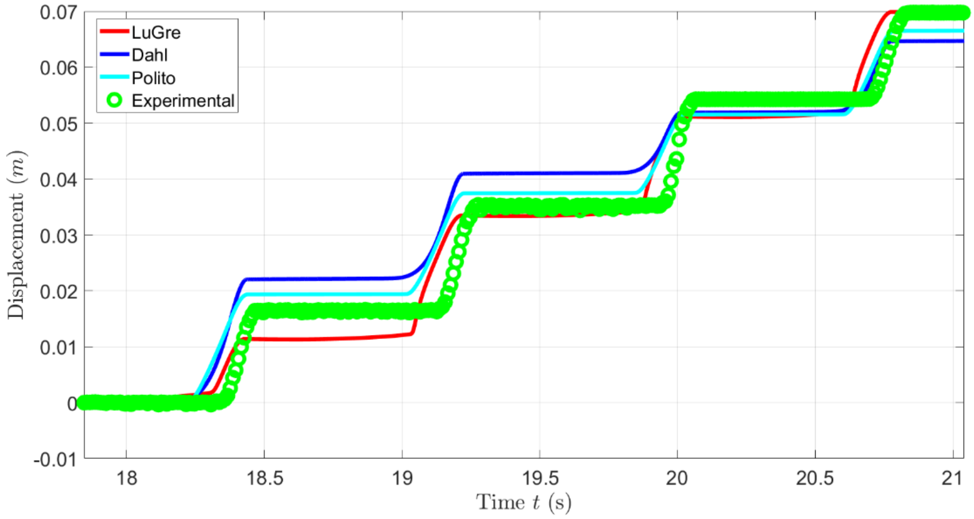

Figura 4.5a Displacement comparison.

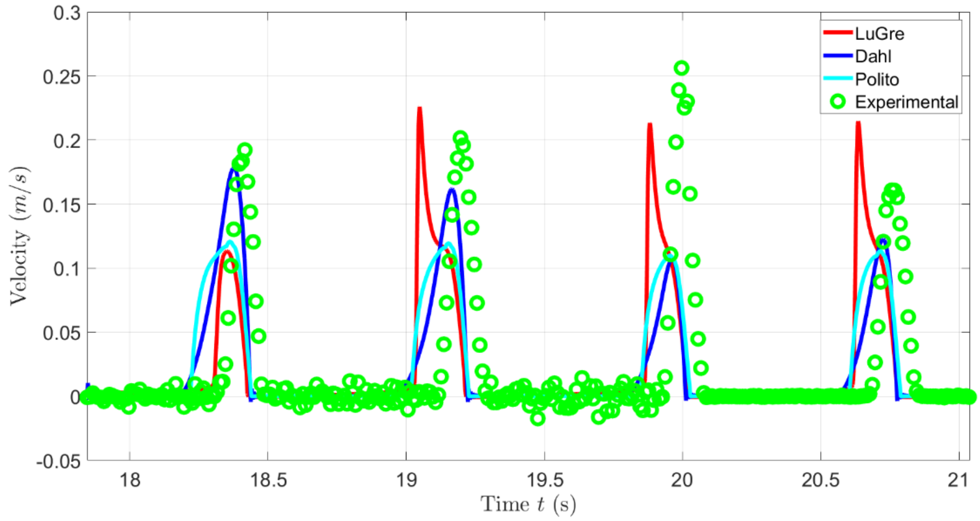

Figura 4.5b Velocity comparison.

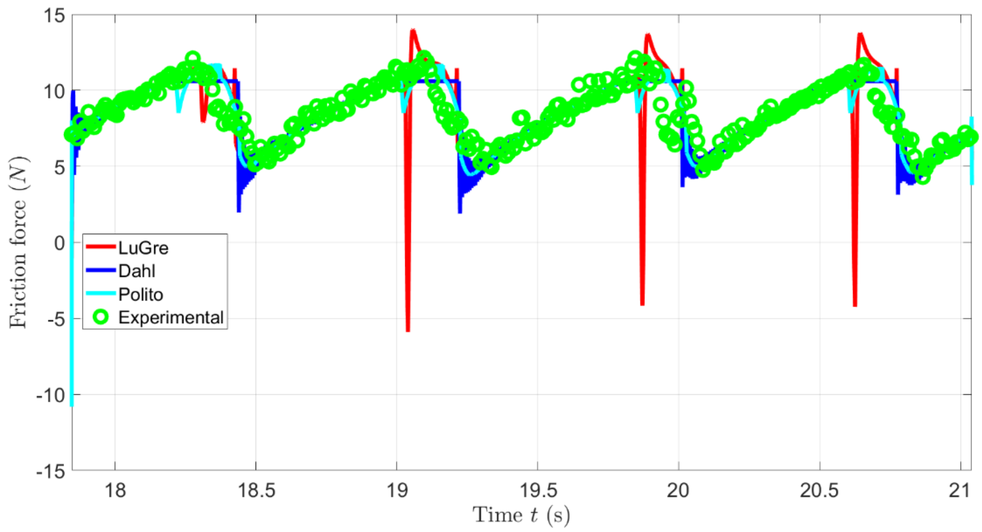

Figura 4.5c Friction force comparison.

The comparison between experimental and numerical displacements emphasizes that the numerical models anticipate the cart movements and they do not perfectly match the step sizes. This can be due to the fact that the breakaway force exhibits small variation between one step and another. Regarding velocities, it can be seen that the shape of numerical and experimental curves is quite similar but, in general, the duration of the experimental peaks is smaller, whereas the amplitude is higher. Polito model reproduces regular pulses and Dahl is the best between the three models at follow the experimental velocity. Regarding the friction force, Polito and LuGre follow the sawtooth trend but with some problems: Polito has numerical instabilities at each peak of the sawtooth, while LuGre presents some peaks when the cart starts to slip. Those LuGre peaks may be due to the high values of σ_0 and σ_1 that takes place only when the cart sticks and asperities deform. Dahl does not follow the sawtooth behaviour but follows a step behaviour with oscillations when F_f reach the minimum values.

4.3 Gross sliding regime

In this test, the numerical simulation tries to predict the friction force under gross sliding regime. In this regime, velocities are big enough to overcome the transition regime and macro-viscous forces come into play. The Stribeck curve can be draw and its parameter can be spotted. The numerical models that are considered for this numerical simulation are the Polito and LuGre model.

4.3.1 First configuration

Regarding the first set up (see Figure 2.11a), the considered test is the one performed at 1 Hz, 4.9 bar and ΔV equal to 1 V (Sine_10Hz_fs1kHz_49bar_A1_1). The numerical parameters have been found through the Stribeck curve (Figure 4.6) while the remaining once were undertaken manually through a trial-and-error procedure.

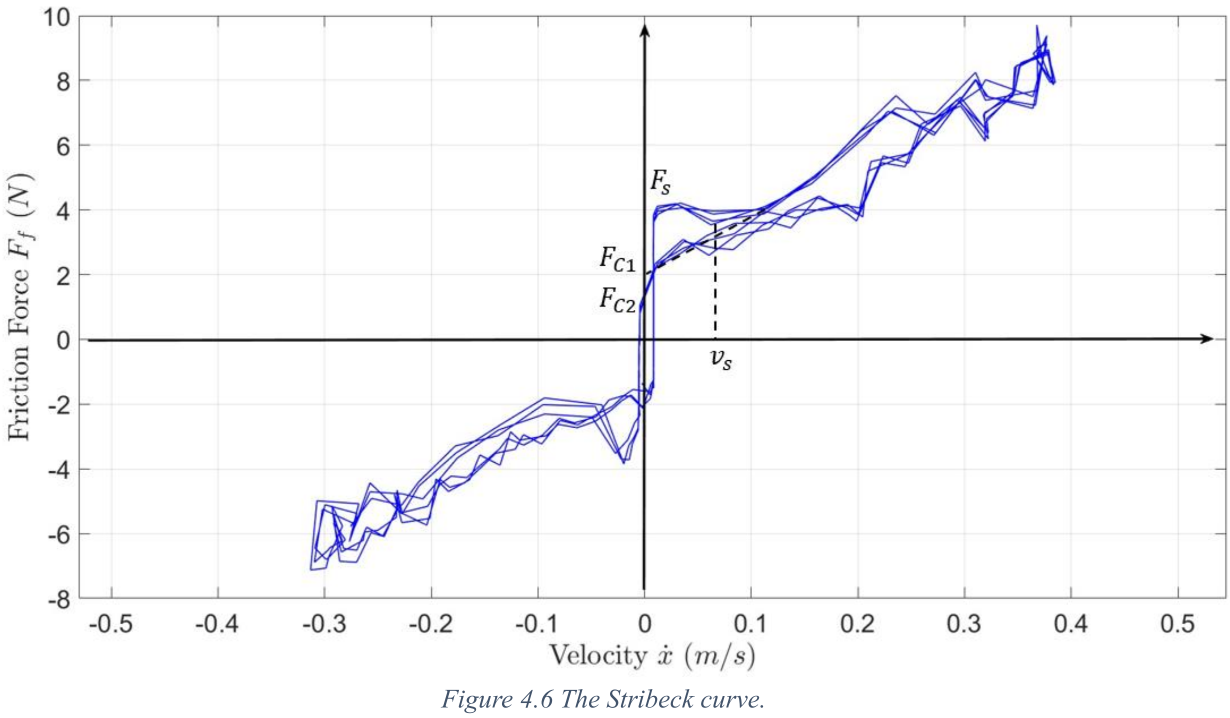

Figure 4.6 The Stribeck curve.

- Polito model

Coefficient	Value
$\boldsymbol{F_s}\ (\boldsymbol{N})$	$\mathbf{4.2}$
$\boldsymbol{F_{C1}}\ (\boldsymbol{N})$	2
$\boldsymbol{F_{C2}}\ (\boldsymbol{N})$	2
$\boldsymbol{v_s}\ \left(\frac{\boldsymbol{m}}{\boldsymbol{s}}\right)$	0.06
$\boldsymbol{\varepsilon}\ \left(\frac{\boldsymbol{m}}{\boldsymbol{s}}\right)$	10^{-4}
$\boldsymbol{c_1}\ \left(\frac{\boldsymbol{N}}{\frac{\boldsymbol{m}}{\boldsymbol{s}}}\right)$	23
$\boldsymbol{c_2}\ \left(\frac{\boldsymbol{N}}{\frac{\boldsymbol{m}}{\boldsymbol{s}}}\right)$	7
$\boldsymbol{\delta}$	0.5
$\boldsymbol{mass}\ (\boldsymbol{kg})$	0.88

- LuGre model

Coefficient	Value
$\boldsymbol{F_s}\ (\boldsymbol{N})$	$\mathbf{4.2}$
$\boldsymbol{F_C}\ (\boldsymbol{N})$	2
$\boldsymbol{v_s}\ \left(\frac{\boldsymbol{m}}{\boldsymbol{s}}\right)$	0.06
$\boldsymbol{\delta}$	1
$\boldsymbol{mass}\ (\boldsymbol{kg})$	0.88
$\boldsymbol{\sigma_0}\ \left(\frac{\boldsymbol{N}}{\boldsymbol{m}}\right)$	10
$\boldsymbol{\sigma_1}\ \left(\frac{\boldsymbol{N}}{\frac{\boldsymbol{m}}{\boldsymbol{s}}}\right)$	3
$\boldsymbol{\sigma_2}\ \left(\frac{\boldsymbol{N}}{\frac{\boldsymbol{m}}{\boldsymbol{s}}}\right)$	23

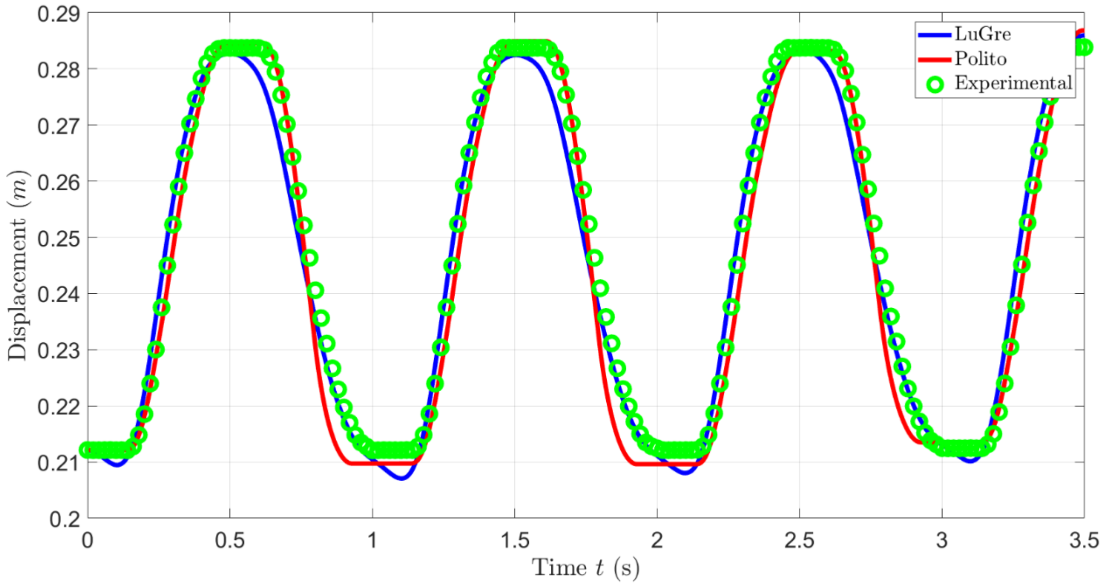

Figure 4.7a Displacement comparison.

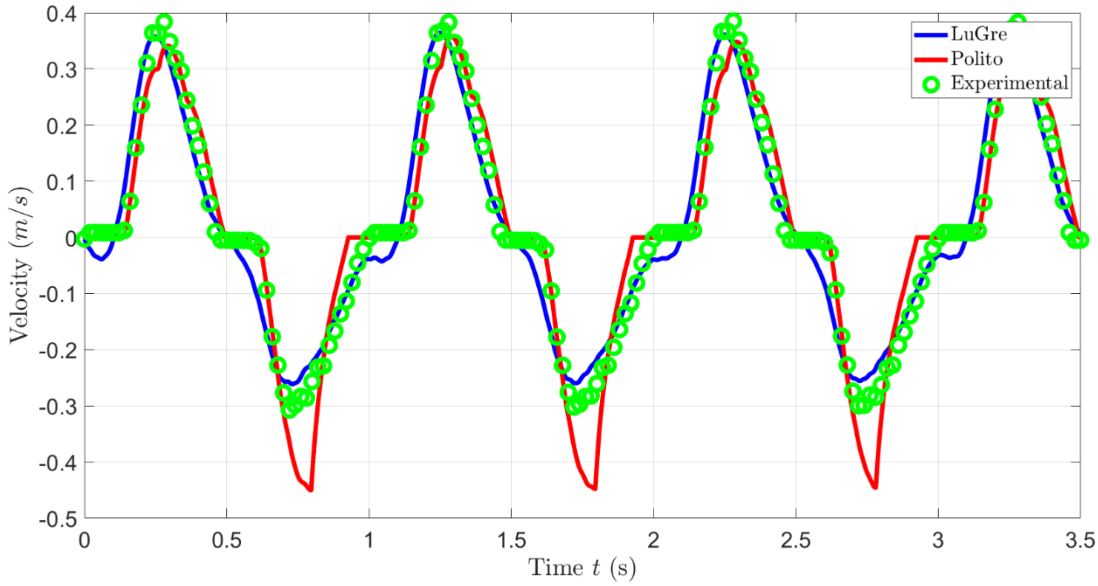

Figure 4.7b Velocity comparison.

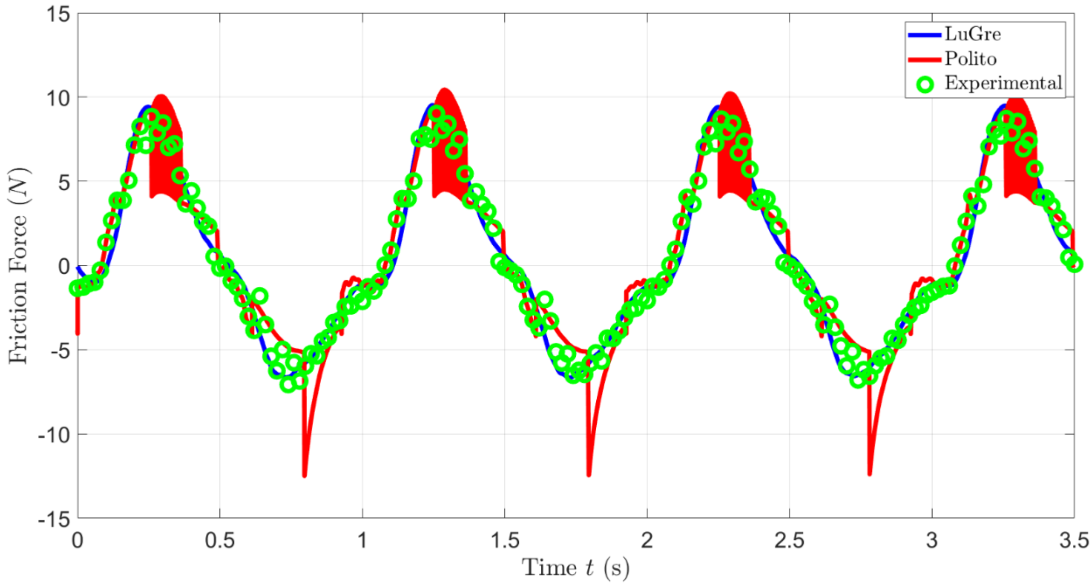

Figure 4.7c Friction force comparison.

Concerning the displacement, the experimental and numerical results are in good agreement. Polito model seems to be the most accurate, since LuGre does not stops at motion reversal. In view of this, LuGre model does not match very well experimental data when the experimental velocity is equal to zero. However, LuGre provides the best results as regard as the friction force trend. The friction force computed from Polito model is less accurate since the experimental Stribeck curve exhibit a non-symmetrical shape. Polito also presents numerical instabilities at motion reversal when the friction force reaches its maximum value.

4.3.2 Second sconfiguration

Regarding the second set-up (see Figure 2.11b), the experimental test (Regolatore_PID_PB2_f1Hz_dV04_1) is chosen in between many tests listed in [20]. It was conducted on the second configuration of the test bench detailed in Sec.2.1. The test is performed compressing the rear chamber at 2 bar with a frequency input voltage signal of 1 Hz. To perform the numerical simulation, Stribeck parameters are needed, and they can acquire from the Stribeck curve.

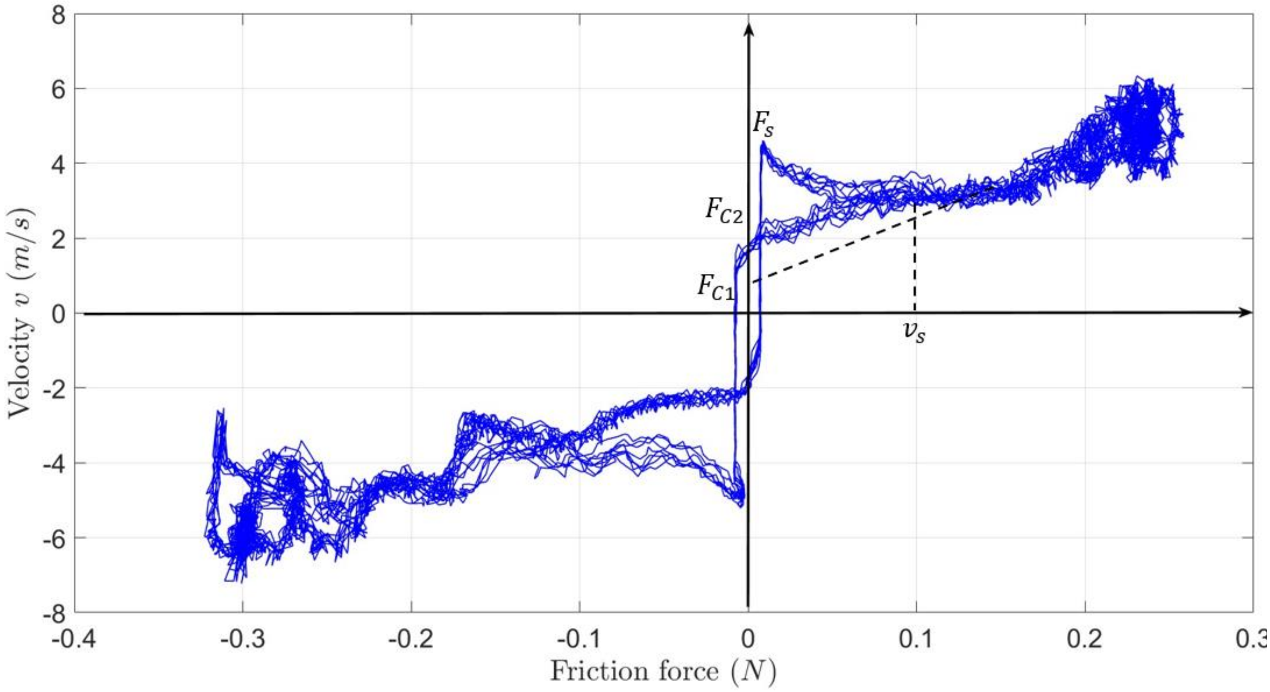

Figure 4.8 Stribeck curve.

Based on the Stribeck curve, the chosen parameters are:

- Polito model

Coefficient	Value
$\boldsymbol{F_s\ (N)}$	$\mathbf{4.2}$
$\boldsymbol{F_{C1}\ (N)}$	0.7
$\boldsymbol{F_{C2}\ (N)}$	2
$\boldsymbol{v_s\ \left(\frac{m}{s}\right)}$	0.1
$\boldsymbol{\varepsilon\ \left(\frac{m}{s}\right)}$	10^{-4}
$\boldsymbol{c_1\ \left(\frac{N}{\frac{m}{s}}\right)}$	16
$\boldsymbol{c_2\ \left(\frac{N}{\frac{m}{s}}\right)}$	13
$\boldsymbol{\delta}$	0.5
$\boldsymbol{mass\ (kg)}$	0.88

- LuGre model

Coefficient	Value
$\boldsymbol{F_s\ (N)}$	$\mathbf{4.2}$
$\boldsymbol{F_C\ (N)}$	0.7
$\boldsymbol{v_s\ \left(\frac{m}{s}\right)}$	0.1
$\boldsymbol{\delta}$	0.5
$\boldsymbol{mass\ (kg)}$	0.88
$\boldsymbol{\sigma_0\ \left(\frac{N}{m}\right)}$	3000

$\boldsymbol{\sigma_1}\ \left(\frac{\boldsymbol{N}}{\frac{\boldsymbol{m}}{\boldsymbol{s}}}\right)$	90
$\boldsymbol{\sigma_2}\ \left(\frac{\boldsymbol{N}}{\frac{\boldsymbol{m}}{\boldsymbol{s}}}\right)$	15

Regarding the Polito model parameters, the F_s,F_{C1},F_{C2} and v_s factors come directly from the Stribeck curve in Figure 4.4. The other parameters are arbitrarily chosen with a trial-and-error procedure. Similarly, the LuGre parameters comes both from the Stribeck curve and from an arbitrarily choice. Here are the results:

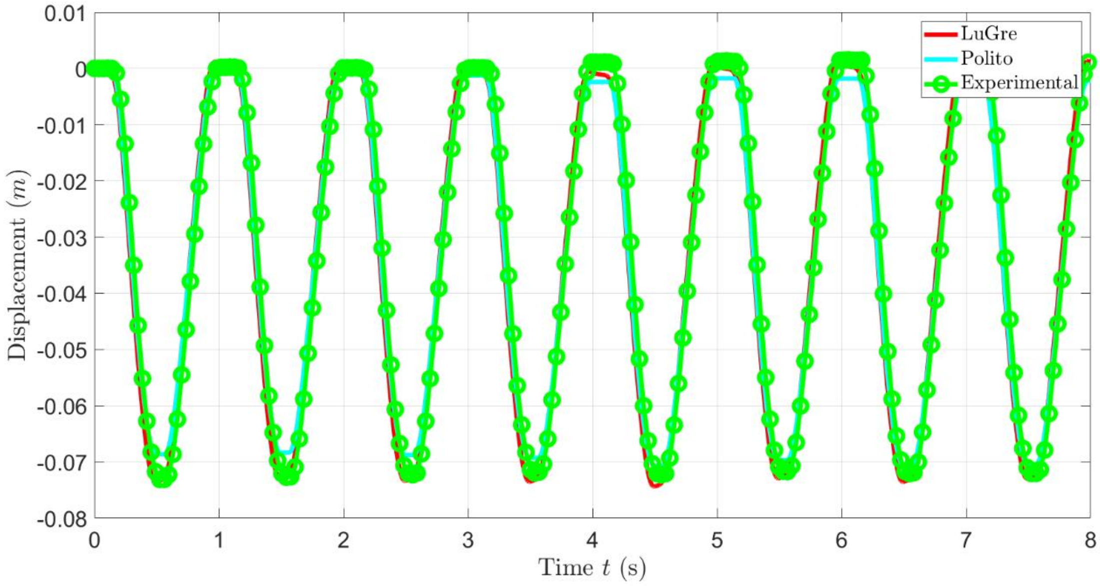

Figure 4.9a Displacement comparison.

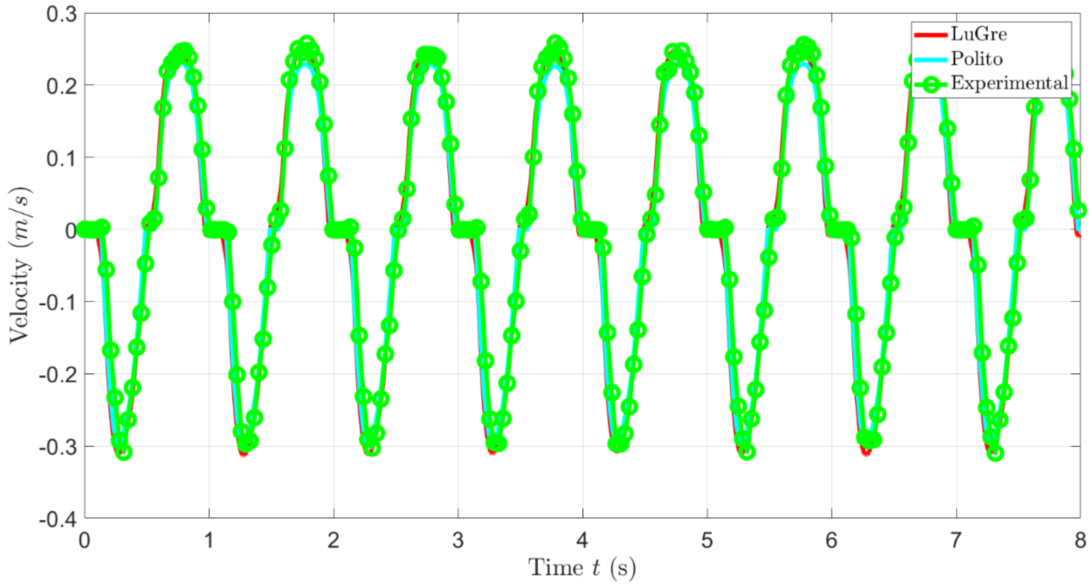

Figure 4.9b Velocity comparison.

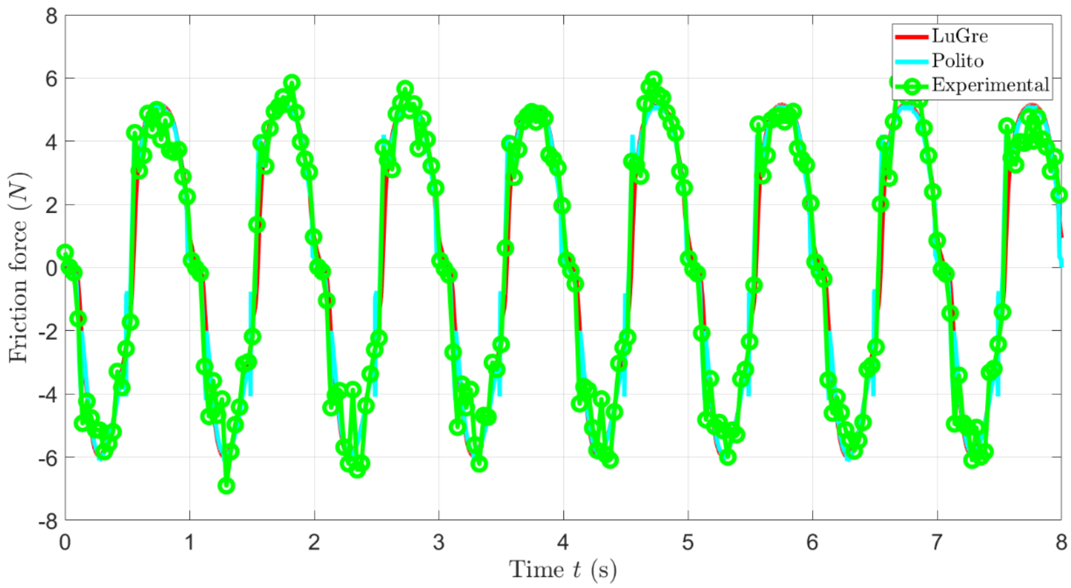

Figure 4.9c Friction force comparison.

In this case, experimental and numerical results are in good agreement both for Polito and LuGre models. Dahl model was not considered due its poor accuracy in providing results for this kind of test. It is worth pointing out that the parameter identified in this type of test are quite different from those employed in the other gross-sliding test configuration. Hence, the presence of a plugged chamber significantly affects the identification process.

CONCLUSIONS

Pneumatic actuators are extensively utilized in the industrial applications due to their cost-effectiveness, versatility, and mechanical simplicity in comparison to other types of actuators. Moreover, the utilization of compressed air provides increased flexibility in their application, even in potentially hazardous environments. Additionally, air, as the driving fluid, is considered a sustainable resource when contrasted with other fluids like oils.

The primary aim of this research is to investigate the frictional behaviour of pneumatic cylinders for servo positioning applications.

Experimental tests were performed by means of a system consisting of a cart guided by a linear guide with recirculating ball bearings, and it is actuated through a double-acting pneumatic cylinder and a 5/3-ways proportional flow valve. This experimental set-up was used to investigate the frictional behaviour of the system in the presence of transition and gross sliding regimes.

Transition tests was necessary to identify the stick-slip phenomenon. They were performed at different supply pressure of the control valve pressure (starting from 1.5 bar up to 6 bar with 0.5 bar of step). At each supply pressure value, it is necessary to find out the lowest tension level at which the valve triggers the piston motion.

Gross-sliding tests were performed by considering two different configurations of the test bench. This kind of test was performed to study the positioning system behaviour under different working conditions: valve supply pressure, driving voltage and frequency.

Regarding the transition regime test, starting from the rest the valve is set to the minimum constant value that guarantees the outstroke of the cylinder in the low velocity regime. In this way, it was possible to experience the presence of the stick-slip phenomenon. During the stick-slip process, the cart displacement resembles a stepped trend in both directions.

In the first configuration of the gross-sliding test, a sinusoidal voltage signal makes the valve shutter move periodically and the cart starts its motion. At low excitation frequencies, the cart displacement does not follow a sinusoidal trend, since, at motion reversal, there is a time interval in which the piston-cart-rod system sticks. Subsequently, the system starts moving again when the pressure force overcomes the breakaway one. The second configuration behaves very similarly to the first one.

These tests made it possible to draw Stribeck curves and identify the gross sliding parameters that were employed in the implemented numerical models. These mathematical frameworks considers both static and dynamic friction models. The so called, Polito model is a static model considering stiction, viscous and Coulomb friction. Conversely, Dahl, LuGre and Leuven models are dynamical since include a state equation accounts for the deformation of the asperities of the mating surfaces.

The use of this models reveals large difficulties in identifying friction parameters that are suitable to simulate any test condition. In particular, due to the lack of a suitable experimental instrumentation it was not possible to identify the friction parameters that governs the behaviour in pre-sliding regimes.

Conversely, gross sliding test makes it possible to provide satisfactory estimations of the frictional parameters that governs the system behaviour in this regime. As a consequence, the implemented models are very accurate in the prediction in gross-sliding regime, but they present a room for improvements regarding the pre-sliding and transition ones.

BIBLIOGRAPHY

[1] V. I. Ivlev, S. Yu. Misyurin, and A. P. Nelyubin, ‘Friction Model Identification for Dynamic Modeling of Pneumatic Cylinder’, in *Brain-Inspired Cognitive Architectures for Artificial Intelligence: BICA*AI 2020*, A. V. Samsonovich, R. R. Gudwin, and A. D. S. Simões, Eds., in Advances in Intelligent Systems and Computing, vol. 1310. Cham: Springer International Publishing, 2021, pp. 127–137. doi: 10.1007/978-3-030-65596-9_16.

[2] G. Belforte, G. Mattiazzo, S. Mauro, and L. R. Tokashiki, ‘Measurement of friction force in pneumatic cylinders’, *Tribotest*, vol. 10, no. 1, pp. 33–48, Sep. 2003, doi: 10.1002/tt.3020100104.

[3] F. Al-Bender, V. Lampaert, and J. Swevers, ‘A Novel Generic Model at Asperity Level for Dry Friction Force Dynamics’, *Tribology Letters*, vol. 16, no. 1/2, pp. 81–93, Feb. 2004, doi: 10.1023/B:TRIL.0000009718.60501.74.

[4] B. N. J. Persson and E. Tosatti, Eds., *Physics of Sliding Friction*. Dordrecht: Springer Netherlands, 1996. doi: 10.1007/978-94-015-8705-1.

[5] T. Piatkowski, ‘Dahl and LuGre dynamic friction models — The analysis of selected properties’, *Mechanism and Machine Theory*, vol. 73, pp. 91–100, Mar. 2014, doi: 10.1016/j.mechmachtheory.2013.10.009.

[6] E. Pennestrì, V. Rossi, P. Salvini, and P. P. Valentini, ‘Review and comparison of dry friction force models’, *Nonlinear Dyn*, vol. 83, no. 4, pp. 1785–1801, Mar. 2016, doi: 10.1007/s11071-015-2485-3.

[7] T. Tjahjowidodo, F. Al-Bender, H. Van Brussel, and W. Symens, ‘Friction characterization and compensation in electro-mechanical systems’, *Journal of Sound and Vibration*, vol. 308, no. 3–5, pp. 632–646, Dec. 2007, doi: 10.1016/j.jsv.2007.03.075.

[8] L. Lentini, L. Mazza, G. Mossino, and T. Raparelli, ‘Modelling and Identification of a Pneumatic Positioning System: A Preliminary Study’, in *Advances in Italian Mechanism Science: Proceedings of the 4th International Conference of IFToMM Italy*, Springer, 2022, pp. 414–421.

[9] Y. F. Liu, J. Li, Z. M. Zhang, X. H. Hu, and W. J. Zhang, ‘Experimental comparison of five friction models on the same test-bed of the micro stick-slip motion system’, *Mechanical Sciences*, vol. 6, no. 1, pp. 15–28, 2015.

[10] V. Lampaert, J. Swevers, and F. Al-Bender, ‘Comparison of model and non-model based friction compensation techniques in the neighbourhood of pre-sliding friction’, in *Proceedings of the 2004 American Control Conference*, Boston, MA, USA: IEEE, 2004, pp. 1121–1126 vol.2. doi: 10.23919/ACC.2004.1386722.

[11] V. Lampaert, J. Swevers, and F. Al-bender, ‘EXPERIMENTAL COMPARISON OF DIFFERENT FRICTION MODELS FOR ACCURATE LOW-VELOCITY TRACKING’.

[12] Y.-H. Sun, T. Chen, C. Q. Wu, and C. Shafai, ‘A comprehensive experimental setup for identification of friction model parameters’, *Mechanism and Machine Theory*, vol. 100, pp. 338–357, Jun. 2016, doi: 10.1016/j.mechmachtheory.2016.02.013.

[13] M. Couillard, P. Masson, and P. Micheau, ‘Identification of Friction Parameters for Limited Relative Displacement Contacts’, *Shock and Vibration*, vol. 16, no. 5, pp. 481–493, 2009, doi: 10.1155/2009/692560.

[14] T. Raparelli, A. Manuello, and L. Mazza, ‘study of friction in an elastomeric seal for pneumatic linders’.

[15] B. M. Y. Nouri, ‘Friction identification in mechatronic systems’, *ISA Transactions*, vol. 43, no. 2, pp. 205–216, Apr. 2004, doi: 10.1016/S0019-0578(07)60031-7.

[16] F. Al-Bender, V. Lampaert, and J. Swevers, ‘Modeling of dry sliding friction dynamics: From heuristic models to physically motivated models and back’, *Chaos*, vol. 14, no. 2, pp. 446–460, Jun. 2004, doi: 10.1063/1.1741752.

[17] J. Swevers, F. Al-Bender, C. G. Ganseman, and T. Projogo, ‘An integrated friction model structure with improved presliding behavior for accurate friction compensation’, *IEEE Trans. Automat. Contr.*, vol. 45, no. 4, pp. 675–686, Apr. 2000, doi: 10.1109/9.847103.
[18] V. Lampaert, J. Swevers, and F. Al-Bender, ‘Modification of the Leuven integrated friction model structure’, *IEEE Trans. Automat. Contr.*, vol. 47, no. 4, pp. 683–687, Apr. 2002, doi: 10.1109/9.995050.
[19] F. Al-Bender, W. Symens, J. Swevers, and H. Van Brussel, ‘Theoretical analysis of the dynamic behavior of hysteresis elements in mechanical systems’, *International Journal of Non-Linear Mechanics*, vol. 39, no. 10, pp. 1721–1735, Dec. 2004, doi: 10.1016/j.ijnonlinmec.2004.04.005.
[20] G. Mossino, ‘Identificazione e Modellazione di un Sistema di Posizionamento ad Azionamento Pneumatico= Identification and Modelling of a Pneumatic Drive Positioning System’, MSc Thesis, Politecnico di Torino, 2022.